

2009

Surface damage of metallic implants due to mechanical loading and chemical reactions

Jae-joong Ryu
Iowa State University

Follow this and additional works at: <https://lib.dr.iastate.edu/etd>

 Part of the [Mechanical Engineering Commons](#)

Recommended Citation

Ryu, Jae-joong, "Surface damage of metallic implants due to mechanical loading and chemical reactions" (2009). *Graduate Theses and Dissertations*. 10480.

<https://lib.dr.iastate.edu/etd/10480>

This Dissertation is brought to you for free and open access by the Iowa State University Capstones, Theses and Dissertations at Iowa State University Digital Repository. It has been accepted for inclusion in Graduate Theses and Dissertations by an authorized administrator of Iowa State University Digital Repository. For more information, please contact digirep@iastate.edu.

Surface damage of metallic implants due to mechanical loading and chemical reactions

by

JaeJoong Ryu

A dissertation submitted to the graduate faculty
in partial fulfillment of the requirements for the degree of
DOCTOR OF PHILOSOPHY

Major: Mechanical Engineering

Program of Study Committee:
Pranav Shrotriya, Major Professor
Palaniappa A. Molian
Sriram Sundararajan
LeAnn E. Faidley
Vinay Dayal

Iowa State University

Ames, Iowa

2009

Copyright © JaeJoong Ryu, 2009. All rights reserved.

TABLE OF CONTENTS

TABLE OF CONTENTS.....	ii
LIST OF FIGURES	v
LIST OF TABLES.....	xi
ABSTRACT.....	xii
CHAPTER1. INTRODUCTION	1
Joint replacement implant: Total Hip Joint Replacement.....	2
Orthopedic alloys and their oxide layer	3
Metal corrosion in human body	4
Research approach	5
Thesis organization.....	6
CHAPTER 2. ONSET OF SURFACE DAMAGE IN MODULAR ORTHOPEDIC IMPLANT MATERIALS: INFLUENCE OF NORMAL CONTACT LOADING AND STRESS-ASSISTED DISSOLUTION.....	8
Abstract.....	8
Introduction.....	9
Materials and Experimental procedure	13
Numerical Model	18
Results and Discussion	20
Conclusion	27
Acknowledgments.....	27
CHAPTER 3. INSTABILITY IN ROUGHNESS EVOLUTION OF METALLIC IMPLANT SURFACE UNDER CONTACT LOADING AND ELECTROCHEMICAL ETCHING.....	28
Abstract.....	28
Introduction.....	29

Material and Methods	31
Experimental Results and Discussion	37
Conclusion	48
CHAPTER 4. ANALYTICAL MODEL OF MULTI-ASPERITY CONTACT AND SURFACE INSTABILITY IN CHEMICAL REACTION: INFLUENCE OF CONTACT-INDUCED RESIDUAL STRESS AND STRESS-ASSISTED DISSOLUTION	49
Abstract.....	49
Introduction.....	50
Residual stress of multi-asperity contact and Stressed surface instability in chemical reaction.....	52
Experimental measurement of surface instability by contact-induced stress and corrosion ..	58
Results.....	59
Conclusion	63
CHAPTER 5. DELAMINATION WEAR MECHANISM BY FATIGUE CRACK GROWTH DUE TO SLIDING CONTACT OF SINGLE ASPERITY: INFLUENCE OF RESIDUAL STRESS ON CRACK GROWTH RATE	64
Abstract.....	64
Introduction.....	65
Mechanics Model of Delaminating Crack	67
Results and Discussion	80
Conclusion	85
CHAPTER 6. ELECTROCHEMICAL DISSOLUTION OF BIOMEDICAL GRADE TI6AL4V: INFLUENCE OF RESIDUAL STRESS AND ENVIRONMENT	86
Abstract.....	86
Introduction.....	87
Experimental set up and procedure.....	88
Results and Discussion	93

CHAPTER 7. CONCLUSIONS	102
APPENDIX.....	107
REFERENCES	111
ACKNOWLEDGEMENT	120

LIST OF FIGURES

Figure 1- 1. Major components of total hip joint replacement; polymeric acetabular, femoral head, and femoral stem.....	3
Figure 2- 1. Surface finish of implant interfaces: (a) Interface of modular hip joint system (b) machined surface configuration of stem and (c) machined pattern of femoral head.....	10
Figure 2- 2. Optical profilometer scan of the specimen surface roughness machined to undulating finish similar to modular implant interfaces (scan size: 1.2 mm × 1.2 mm).....	14
Figure 2- 3. Schematic representation of contact loading test set up.....	15
Figure 2- 4. Asperity amplitude distribution of undulating surface presented by Fast Fourier Transform.....	17
Figure 2- 5. Amplitude changes of dominant modes due to contact pressing to 70 % of specimen yield strength.....	18
Figure 2- 6. Schematic representation of finite element model and boundary conditions	19
Figure 2- 7. Surface roughness evolution: normalized amplitude change over the loading cycles for contact loads of 60 % of yield strength.....	21
Figure 2- 8. Roughness evolution: normalized amplitude change under alternating normal contact loading to 0.7 times yield strength and etching exposure	22
Figure 2- 9. Contour plot of contact loading induced residual stress for undulating surface loaded to 70% of σ_y	23

Figure 2- 10. Average of normalized amplitude change observed on exposure to corrosive medium plotted as a function of normalized residual stress level at troughs of undulating surface.....	24
Figure 2- 11. Schematic of the proposed mechanism governing surface deformation due to combined influence of contact loading and corrosion	26
Figure 3- 1. Surface roughness of CoCrMo by milling (top) and grinding (bottom) process.....	32
Figure 3- 2. Normal contact (left) and inclined contact (right) experimental set up	33
Figure 3- 3. Surface roughness measured by optical profilometry; milled surface (top), ground surface (bottom).....	37
Figure 3- 4. Fast fourier transform spectrum of milled surface (top) and fractal surface (bottom); undulating surface presented the most dominant roughness mode as highlighted by red dashed line	39
Figure 3- 5. Roughness amplitude changes by alternating normal (top) and inclined (bottom) contact and subsequent nanoscale etching (amplitudes are normalized by initial amplitude to facilitate data interpretation).....	41
Figure 3- 6. Relative roughness amplitude changes ($\mu_1-\mu_2$) of normal (top) and inclined (bottom) contact-stressed surface in chemical reactions. The statistical significance was evaluated by comparison with roughness amplitude change of unstressed surface after etching, where μ_1 and μ_2 are average roughness amplitude change of stressed surface and unstressed surface, respectively.....	42
Figure 3- 7. Numerical prediction of stress field by normal (top) and inclined (bottom) contact of undulating surface.....	44

Figure 3- 8. Roughness evolution of stressed surface during chemical reaction illustrates quadratic dependence of contact induced residual stress.....	45
Figure 3- 9. Surface roughness evolution by alternating normal contact and nanoscale etching.....	46
Figure 3- 10. Spatial frequency where the maximum roughness evolution takes place indicates stress state developed during contact, significant influences of magnitude of contact loads and type of indenting motions were illustrated on ground surface.....	47
Figure 4- 1. Residually developed maximum principal plastic strain of undulating surface after contact loading-unloading.....	53
Figure 4- 2. two half-spaced (region 1 and region 2) elastic medium joined at interface with mirrored series of dilatation lines at distance of d from interface.	54
Figure 4- 3. In order to obtain traction free boundary condition on the perturbed surface, stress field due to equal and opposite surface tractions was superposed to stress field due to series of mirrored line dilatations.	55
Figure 4- 4. Finite element model was characterized as an elastic-perfectly plastic plane strain body. Surface roughness is parameterized by amplitude to wavelength ratio in the range of $0.003 < a/\lambda < 0.0125$ and contact loadings are characterized in the range of $0.4\sigma_y < P < 0.7\sigma_y$ where σ_y is yield strength of the contact medium.....	56
Figure 4- 5. Specimen surface roughness and normal contact experimental set up	59
Figure 4- 6. Source and (b) depth of line dilatation map predicted by matching with FEM in terms of roughness and nominal contact pressures.	60

- Figure 4- 7. (a) Roughness evolution depends on surface stress state at asperity summits and troughs, (b) quadratic correlation of chemical reaction rate (Δh) and residual stress developed by contact..... 62
- Figure 5- 1. A continuum body subjected to combined parabolic and tangential contact with pre-existing crack at subsurface, where P_o is maximum contact pressure, h and $2c$ are depth of crack location and half length of subsurface crack, respectively.... 68
- Figure 5- 2. Maximum principal stress distribution solved by Johnson's elastic contact solution under combined loading of parabolic normal and parabolic tangential contact (top) and parabolic normal and uniform tangential contact (bottom) with $\mu = 0.5$ 70
- Figure 5- 3. Geometrical presentation of through crack and edge crack with loads. 71
- Figure 5- 4. Contour of ΔK_I on parallel crack due to combined contact of parabolic normal and parabolic tangential (top), and parabolic normal and uniform tangential (bottom) loadings 73
- Figure 5- 5. Contour of ΔK_{II} on parallel crack due to combined contact of parabolic normal and parabolic tangential (top), and parabolic normal and uniform tangential (bottom) loadings 74
- Figure 5- 6. Parallel crack model with normal traction and constant friction coefficient, $\mu = 0.5$ is subjected to in-plane compression ($-\sigma_\infty$) and tension ($+\sigma_\infty$) 76
- Figure 5- 7. Contour of stress intensity factor of mode I by parabolic friction without far-field stress (top), with far-field compression (middle) and with far-field tension (bottom)..... 78

Figure 5- 8. Contour of stress intensity factor of mode II by parabolic friction without far-field stress (top), with far-field compression (middle) and with far-field tension (bottom).....	79
Figure 5- 9. Maximum ΔK_I distribution along the depth of the contacting medium with different tangential tractions.	82
Figure 5- 10. Maximum ΔK_{II} distribution along the depth of the contacting medium with different tangential tractions.	82
Figure 5- 11. Maximum ΔK_I (top) and ΔK_{II} (bottom) distribution along the depth of the contacting medium indicates higher fatigue crack growth rate and wear depth.....	83
Figure 5- 12. Linear trend of maximum ΔK_I with in-plane stresses implies residual stress dependence of delamination wear.....	84
Figure 5- 13. Linear dependence of wear depth during cyclic sliding contact of single asperity with pre-stress loaded on the contacting CoCrMo sample surface where h is measured wear depth and a_c is half contact area obtained by Hertzian contact model.....	84
Figure 6- 1. C-clamp design with capacitance gage, utilizing varying size of rollers different bending force, which can be measured by deflection of free end of clamp arm, can be loaded on the rectangular specimen.	89
Figure 6- 2. AFM-based fretting contact experimental on stressed rectangular specimen by 4-point bending set up using c-clamp.	90
Figure 6- 3. Wear volume of Ti6Al4V with varying pre-stress state due to fretting contact of AFM tip in ambient condition (RH = 35±3 %).	93

Figure 6- 4. Wear volume of CoCrMo with varying pre-stress state due to fretting contact of AFM tip in ambient condition (RH = 44±5 %).	94
Figure 6- 5. Wear volume of Ti6Al4V with varying pre-stress states due to fretting contact of AFM probe in passivating condition of pH 7.4.	95
Figure 6- 6. Wear volume of CoCrMo with varying pre-stress states due to fretting contact of AFM probe in passivating condition of pH 7.4	95
Figure 6- 7. Wear volume of Ti6Al4V with varying pre-stress states due to fretting contact of AFM probe in corroding condition of PBS, pH 4.11.	96
Figure 6- 8. Wear volume of Ti6Al4V with varying pre-stress states due to fretting contact of AFM probe in corroding condition of PBS, pH 1.98.	97
Figure 6- 9. Wear volume of CoCrMo with varying pre-stress states due to fretting contact of AFM probe in corroding condition of PBS, pH 4.11.	98
Figure 6- 10. Wear volume of Ti6Al4V with varying pre-stress states due to fretting contact of AFM probe in corroding condition of CaCl ₂ , pH 1.95.	99
Figure 6- 11. Wear volume of CoCrMo with varying pre-stress states due to fretting contact of AFM probe in corroding condition of CaCl ₂ , pH 4.11.	99

LIST OF TABLES

Table 2- 1. Loading levels applied on the implant specimens.....	15
Table 2- 2. Mechanical properties of CoCrMo used in the finite element model	19
Table 3- 1. Number of contact and etching experiment.....	36
Table 3- 2. Surface roughness characteristics on different surface manufacturing process ...	38
Table 3- 3. properties and problem size employed in FEA model	43
Table 4- 1. Description of Finite element model	57
Table 6- 1. Mechanical properties of specimen and AFM probe	92

ABSTRACT

The present study investigates interfacial damage mechanism of modular implants due to synergetic action of mechanical contact loading and corrosion. Modular implants are manufactured such that surfaces have a characteristic degree of roughness determined by tool tip size and motion of tool path or feeding speed. The central hypothesis for this work is that during contact loading of metallic implants, mechanisms of damage and dissolution are determined by contact loads, plastic deformation, residual stresses and environmental conditions at the nanoscale surface asperities; while during subsequent rest periods, mechanism of metallic dissolution is determined by the environmental conditions and residual stress field induced due to long range elastic interactions of the plastically deformed asperities. First part of the thesis is focused on investigating the mechanisms underlying surface roughness evolution due to stress-assisted dissolution during the rest period. The latter part is focused on investigating material removal mechanisms during single asperity contact of implant surfaces.

Experimental study was performed to elucidate the roughness evolution mechanism by combined effect of multi-asperity contact and environmental corrosion. Cobalt-chromium-molybdenum specimen was subjected to either contact loading alone or alternating contact loading and exposure to reactive environment. Roughness of the specimen surface was monitored by optical profilometry and Fast Fourier Transform (FFT) calculation was used to characterize the evolving behavior of roughness modes. Finite element analysis (FEA) was employed to identify influences of surface morphological configurations and contact pressures on the residual stress development. Analytical model of

multi-asperity contact has been developed for prediction of residual stress field for different roughness configurations during varying magnitude of contact loads based on elastic inclusion theory. Experimental results indicate that surface roughness undergoes continuous evolution during alternating contact loading and exposure to etchant. Surface roughness evolution is governed by the residual stress induced due to contact loading. Two different stress-assisted dissolution driven instabilities in roughness evolution have been identified.

In order to investigate stressed surface damage by electrochemical reaction during active contact loading, in the first stage, surface failure due to sliding contact was investigated as a function of different residual stress states from compressive to tensile. Residual stress is usually developed during manufacturing process or former mechanical interactions playing an important role on service life of the surface. The wear mechanism of fatigue contact in the presence of residual stresses was explored by analytical model of fatigue crack growth by utilizing modified delamination wear theory with surface layer spalling model. Fatigue stress intensity factors (ΔK_I) loaded by contact stress and combined residual stress implied that buckling of subsurface crack with compressive residual stress opens crack-tip and consequently increase wear rate during sliding contact. As for the experimental verification of the modified delamination model, cyclic sliding contact experiment on metallic implant materials in ambient was conducted by utilizing atomic force microscope (AFM) and four-point-bending set up by which well characterized pre-stress was established on rectangular specimen. In addition, complex mechanism of corrosion on the damaged surface illustrated strong stress-dependent effects on wear rate in re-passivating environment and dissolution rates in reactive environment.

CHAPTER1. INTRODUCTION

Metallic materials are widely used for biomedical implant applications. Orthopedic implants require the high load-supporting capacity, low wear and friction, and high resistance to corrosion. Therefore, metallic materials, widely used for the biomedical implant purpose are 1) stainless steel alloy (316L, 316LV), 2) cobalt-chromium alloy (ASTM F75, F90, F562), and 3) titanium alloy (ASTM F67, 136) owing to their high ductility and desirable quality of wear and corrosion resistance. In all the alloys described above a stable oxide layer protects underlying material from continuous corrosion damage in reactive environment. However, when the implant system is subjected human motions and loads, the modular interface undergoes mechanical loading leading to local surface damage. During the interaction, there may be combined process of oxide layer fracture-reformation with material dissolution due to electrochemical reaction. When the continuous human behavior results in repetitive contact damage, the synergistic actions of mechanical fracture and chemical reactions accelerate interfacial degradation. Fretting and crevice corrosion has been used to explained the implant surface damage due to repeating process of oxide layer fracture and reformation [1-9]. The repetitive oxidation leads to increase in local hydrogen concentration (drops pH level) by consuming oxygen in physiological body fluid and thus increases the electrochemical reactivity ultimately resulting in oxide layer instability and continuous corrosive attack. The soluble and particulate debris formed through this process may migrate locally and systematically and likely induce adverse reaction with in our body [5, 7, 10]. Consequently, it is very important to understand the basic physical operation of joint replacement system and their wear and corrosion response in our body.

Joint replacement implant: Total Hip Joint Replacement

In order to mimic joint motion, hip replacement system has been designed in the form of pivot hinge or rotational ball-socket assembly. Also, for the wide customization assembled modular design has been preferred. For example, total hip joint replacement (THR) comprises 4 major components; femoral stem, femoral head, polymeric socket (low-friction inserts) and acetabular cup (see Figure 1-1).

The early design of total hip joint device with stainless steel was not successful since the poor corrosion resistance *in vivo* of stainless steel lead to adverse effect with body cells. Efforts to enhance the corrosion resistance led to new materials such as cobalt-chromium and achieved greater success. However their high frictional forces at bearing surface resulted in wear and premature loosening. Polytetrafluororthylene (Teflon) was inserted between acetabular and femoral components to reduce the friction forces but was not successful due to the low wear resistance of the insert. High-density polyethylene was employed to improve wear resistance which became basis for modern design of total hip joint replacement. Innovative technologies have been employed to improve reliability and useful life of the joint replacement by obtaining stable state of joining surface from geometrical modifications, porous coating, surface texturing and so forth [11-15]. Modular implant is constructed by interlocking of femoral head and femoral stem. At the tapered connection such as head-stem interface, the interlocked surface created by machining undergoes rough surface contact and experiences a cyclic process of oxide film breakage and reformation by combined effects of contact and corrosion. Accordingly, it is necessary to identify the nature of oxide layer and surface properties in biomedical purposes.



Figure 1- 1. Major components of total hip joint replacement; polymeric acetabular, femoral head, and femoral stem

Orthopedic alloys and their oxide layer

The dominant metal alloys for artificial joint are stainless steel, cobalt-based alloy and titanium-based alloy. Their oxide layer, which separates the underlying metal from the reactive environment, is the primary reason for their corrosion resistance. The alloys chosen for implant are not perfectly inert in chemical reaction, but the native oxide film blocks the metals from oxygen and moisture. Stainless steel alloys were the first metallic material used for biomedical implant purpose. However their poor resistivity to wear and corrosion limited their service life while the high ductility is still attractive for the dynamic load-bearing use. Other chemical components added to stainless steel enhance the corrosion resistance; molybdenum is added to improve corrosion resistance of grain boundary and chromium forms oxide layer which protects the surface from electrochemical reactions in corrosive environment. Owing to the high quality of fatigue resistance cobalt-based alloys have been selected for joint replacements. The most prevalent cobalt-chromium alloys are cobalt-

chromium-molybdenum (CoCrMo), cobalt-nickel-chromium-molybdenum (CoNiCrMo) and cobalt-chromium-molybdenum-tungsten (CoCrMoW). Chromium and molybdenum help to gain the stability of the surface against corrosion. Nickel containing alloys display increase in friction and wear resistance but are not widely used due to cytotoxicity and allergic reactions to released nickel. Titanium alloys have low density, good strength, and can be easily fabricated. The most attractive characteristic of Ti-alloy is high corrosion resistance since titanium readily forms titanium dioxide (TiO_2) layer which forms a barrier to electrochemical reactions. Greater stability of oxide layer on titanium alloys leads to their excellent biological compatibility. Due to high ductility of commercially pure titanium (CPTi) it has been used for porous coatings while Ti6Al4V has been utilize in general joint replacement components.

Metal corrosion in human body

Metal corrosion is degradation process of metallic materials by reaction with environment. Most of metallic materials are susceptible to corrosion attack if a tenacious surface oxide layer does not exist. However, when the surface layer is permeable to oxygen and moisture, the corrosion process will continue and lead to eventual failure. Among the variety of corrosion mechanism, metal corrosion is driven by electrochemical reactions. During exposure to aqueous environment, atoms of metal surface experience anodic process, namely, electrons are released leading to oxidation and formation of metallic ions. The localized electrical potential accelerates the oxidation process until the electrochemical potential is balanced.

Physiological environment is an oxygen rich saline solution with about 0.9% of salt content in approximately neutral pH level of 7.4 [16]. The body fluid is electrochemically active due to dissolved oxygen and reactive molecules in the forms of sodium and chloride ions, and the conductive water as electrolyte. In this corrosive environment, contact loading of rough surface likely induces small scale oxide film fracture leading to local variance of electrochemical potential. Preferential anodic reactions produce localized surface defects and initiate microscale surface cracks. The repetitive loading on the implant material by human behavior may propagate the surface crack and the synergetic combination between corrosion and surface layer fracture accelerate the interacting surface damage. The repetitive oxidation leads to increase in local hydrogen concentration (drops pH level) by consuming oxygen in physiological body fluid and thus increase the electrochemical reactivity. This event produces corrosion products near the implant site and leads to biocompatibility problems.

Research approach

Present study is to comprehend damage mechanism of implant surface in biological environmental. In order to identify influence of surface roughness and contact loads on surface damage, experimental study of fatigue contact of cobalt-based alloy (cast CoCrMo) and subsequent accelerated corrosion have been conducted. Experimental results indicate that surface roughness continuously evolve during alternating contact loading and corrosion. Roughness amplitude decreases by plastic deformation of contacting surface asperities while roughness amplitude increases by selective corrosion attack depending on local stresses developed due to plastic deformation of the asperities. Finite element analysis (FEA) was

utilized to characterize residual stress field as a function of contact pressures and roughness configurations. Analytical model of multi-asperity contact was developed by elastic inclusion theory. Since it was necessary to identify the strength and location of elastic inclusions, FEA models were developed in varying morphological configurations and nominal contact pressures. Based on the residual stress field obtained by multi-asperity contact solution, stress-driving roughness instability model was investigated by kinetics of surface roughness instability.

Influences of residual stress on fatigue contact damage mechanism were evaluated by inspecting subsurface crack growth rate. Delamination theory of single asperity contact was modified by superposing in-plane compression and tension to understand role of residual stress in fretting contact damage. Influence of residual stress on wear rate was investigated by determining the crack driving force for subsurface cracks and their locations. AFM based single asperity contact experiment was performed to observe residual stress dependence of fretting damage. Four-point-bending set up was used to apply pre-stress field in tension and compression on the rectangular titanium specimen (Ti6Al4V and CoCrMo) and surface damage rates were measured in ambient and aqueous environment. The strong residual stress dependence of implant alloy fretting wear was found in aqueous environment.

Thesis organization

Surface roughness configuration and contact pressure dependence on surface morphology instability was investigated to identify chemo-mechanical damage mechanism by alternating contact experiment and subsequent accelerated corrosion test. Surface roughness changes have been characterized by optical profilometry and Fast Fourier

Transform calculations. Roughness evolution process due to stress-assisted dissolution is summarized in Chapter 2 and Chapter 3.

In Chapter 4, residual stress developed due to multi-asperity contact and kinetics of the stressed surface instability are modeled based on proposed mechanism of surface instability from Chapter 2 and Chapter 3. This analysis provides a simple solution of residual stress developed on contact loading of undulating surface. A new method for determining interfacial surface energy associated with nanoscale etching of cobalt-chromium surface is presented.

In the next part of thesis, surface damage during single asperity contact is investigated. Influence of residual stress on fatigue contact damage was characterized by evaluating cyclic stress intensity factor of subsurface cracks. Delamination wear theory combined with surface layer spalling model is used to explain the significant role of residual stress during cyclic sliding contact in Chapter 5.

Chapter 6 presents Atomic Force Microscope (AFM) based experimental study of fretting corrosion. Wear rate by scratching with silicon-nitride AFM on metallic surfaces was measured in ambient and aqueous environment to identify combined effect of mechanical and chemical reaction on fretting corrosion process.

In Chapter 7, important findings are summarized along with the recommendations for future work.

CHAPTER 2. ONSET OF SURFACE DAMAGE IN MODULAR ORTHOPEDIC IMPLANT MATERIALS: INFLUENCE OF NORMAL CONTACT LOADING AND STRESS-ASSISTED DISSOLUTION

Abstract

Surface damage at interfaces of modular implants results from repeated fretting contacts between metallic surfaces in a corrosive environment. As a first step in understanding this complex process, multi-asperity contact experiments were conducted to characterize roughness evolution due to action of contact loads and exposure to a reactive environment. Cobalt-chromium specimens with surface roughness similar to modular implant were first subjected to only contact loading and subsequently, to alternating contact loads and exposure to reactive environment. During repeated normal contact loading, amplitude of surface roughness reached a steady value after decreasing during the first few cycles. However during the second phase surface roughness amplitude continuously evolved – decreasing during contact loading and increasing on exposure to corrosive environment. The increase in roughness amplitude during surface reaction depended on the magnitude of applied contact loads. A damage mechanism that incorporates contact-induced residual stress development and stress-assisted dissolution is proposed to elucidate the measured surface roughness evolution.

Keywords: Fretting corrosion; Modular implants; surface roughness evolution; stress-assisted dissolution; multi-asperity contact

Introduction

Surface damage of orthopedic implants due to *in vivo* fretting corrosion is of great concern as it may induce a cascade of inflammatory events that may ultimately result in bone loss by osteolysis and subsequent implant failure. Head-stem interface of a typical modular total hip replacement is shown in Figure 2-1. In human body the physiological fluid penetrates implant modular interface leading to synergistic interactions of mechanical loading and electrochemical oxidation, i.e. fretting and corrosion [17, 18]. Due to human actions like walking, jogging, and running biological implants are subjected to repetitive loadings in a corrosive environment resulting in onset of surface damage [8, 17, 18]. Resulting soluble and particulate debris can migrate locally or systemically and may induce biocompatibility problems such as inflammations and necrosis that may ultimately result in bone loss by osteolysis and subsequent implant failure [4, 6, 18-22].

Fretting corrosion response of modular implants has been generally quantified through electrochemical measurements or measurement of weight loss during fretting testing [1-3, 8, 23-26]. Results of the fretting corrosion studies indicate that there is a synergistic interaction of mechanical loading and electrochemical oxidation i.e. material degradation is accelerated by the combined effects of fretting and corrosion. Gilbert and Jacobs [5, 9] have concluded that increased rate of corrosion is due to continual fracture and reformation of oxide layers (repassivation) over the metallic surfaces [9]. This hypothesis explains the reported increase in electrochemical activity but detailed mechanisms on how the contact loads, residual stresses, roughness parameters influence the fretting corrosion have not been well described and are still not clearly understood.

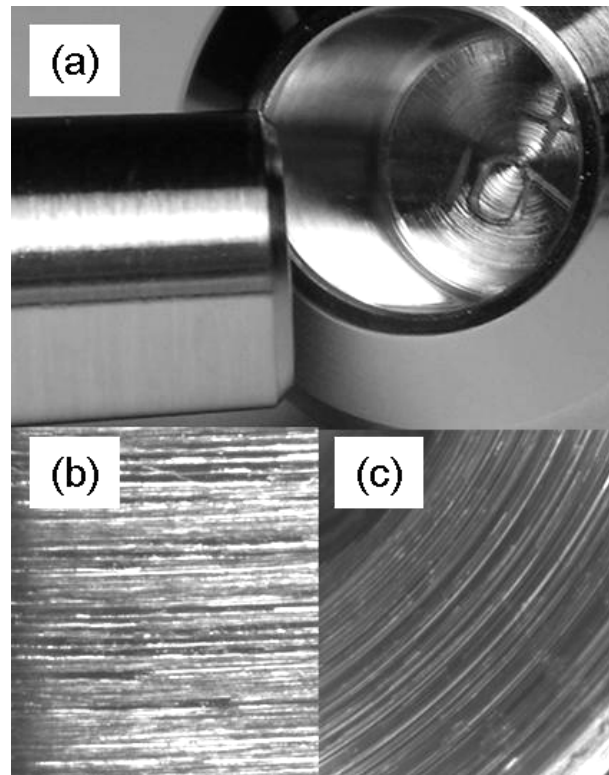


Figure 2- 1. Surface finish of implant interfaces: (a) Interface of modular hip joint system (b) machined surface configuration of stem and (c) machined pattern of femoral head

In a modular implant, head and stem surfaces that form the tapered junction are machined with a regular roughness pattern in order to promote interlocking [8, 17]. When the surfaces are brought in contact, only the protruding surface asperities are in contact. The size and distribution of the contact spots depend on the surface roughness and the applied load. Even when the overall contact loads are not large enough to cause macroscopic deformation, plastic deformation can occur in small scales under the contacting asperities so that the surface roughness changes after the removal of load. The plastic deformation under the asperity contact may lead to development of surface residual stress field and in turn, stress-concentrations near the surface roughness grooves. The corrosive physiological

environment aggressively attacks the area of residual stress concentrations leading to the deepening of grooves exacerbating the surface deformation. The combined effect of plastic surface deformation and stress-assisted corrosion ultimately may result in surface damage by nucleation of small cracks and breaking away of particulate debris. As a first step in understanding this complex process, a combined experimental and numerical approach is utilized to characterize the surface roughness evolution due to combined action of normal contact loading and corrosive environment.

Elastic and elasto-plastic surface deformation due to contact of rough surfaces has been investigated by many researchers [27-40]. In his pioneering work, Archard [27], found that in multiple-asperity-contact of elastic rough surfaces Amontons's law is valid and established that surface topography is an important factor in determining mechanics of rough surface contact. Greenwood and Williamson [28] modeled the rough surface as a Gaussian distribution of identical half sphere asperities and demonstrated that macroscale quantities such as total contact area, the number of asperity contact, contact load, and contact conductance have linear relationships. However they assumed that the neighboring asperities are isolated and do not interact with each other. In order to model the surface response under elasto-plastic deformation, Abbott and Firestone [37] and other authors [38-40] utilized purely plastic or elasto-plastic deformation of truncated single spherical asperity to model rough surface contact while Chang et al. [33] analyzed plastic contact between two rough surfaces based on asperity volume conservation condition (CEB model). As other spherical asperity contact models, they studied isolated single asperity contact model and didn't account for the influence of interactions between two neighboring asperities on the plastic flow [38-40].

Whitehouse and Archard [29] used statistical surface characterization based on digital analysis of roughness profiles for the study of rough surface contact. They showed that the random surface can be modeled with a gaussian height distribution and an exponential autocorrelation function. Rough surface have also been modeled as fractal surfaces using analytical expression based on Weierstrass function. Weierstrass function characterizes self-affine fractal surface using a series of superposed sinusoids. Yan and Komvopoulos [34] used two-variable Weierstrass function for anisotropic surfaces to characterize three-dimensional fractal surface contact in both elastic and elastic-perfectly plastic regime. They identified the impact of surface topography and material properties on the contact behavior. Ciavarella et al. [35] presented analytical model for elastic contact of rough surfaces approximated by Weierstrass function. They investigated partial contact of a sinusoidal surface at different fractal dimensions and determined fractal characteristics of contact area.

Contact loading of rough surface may result in not only elastic but also plastic deformation of the asperities, and the asperities may interact with neighboring asperities. Gao et al. [41] developed an elastic-perfectly plastic contact model for fractal surface profile based on Weierstrass function, considering the interaction between neighboring asperities. Their results indicated that surface deformation is highly dependent on surface geometry and mechanical properties of material. They extended Ciavarella's [35] self-affine fractal rough surface contact to elastic-plastic regime. They calculated calculate critical conditions that will initiate plastic flow in the asperities, and determined the extent of this plastic flow as a function of the applied loading, the material properties of the deforming solid, and the surface roughness. In conclusion, the relationship between contact loading and resulting

contact stress distribution has been investigated thoroughly, but effects of the surface topography on contact-induced residual stress development are not well characterized.

The paper presents experimental descriptions of roughness evolution for a cobalt-chromium surface subjected to two different loading sequences: first sequence of only repeated contact loadings and second sequence of alternating contact loading and exposure to a reactive medium. Fourier spectrum of surface roughness was monitored after each stage of contact and surface chemical reaction in order to identify the roughness modes that dominate surface deformation and characterize the roughness evolution. Finite element analysis was used to predict residual stress distribution due to the dominant surface roughness modes under contact pressing. Finally, a mechanism that incorporates residual stress development during contact loads and preferential attack of corrosive medium on highly stressed locations of surface is proposed to interpret the measured roughness evolution.

Materials and Experimental procedure

Specimen Configuration and loading set-up

Cobalt-chromium-molybdenum, (CoCrMo) designated as ASTM F-75 and F-76 for medical applications is a common cobalt-based alloys used for load supporting orthopedic implants. In the present work, roughness evolution at the taper junction interface between head and stem of modular CoCrMo components is simulated using normal contact loading and exposure to a reactive medium. At the taper junction interface, surface of modular components are machined to an undulating profile to promote interlocking [8] A typical modular junction interface has amplitude to wavelength ratio (a/λ) from 0.003 to 0.005 as shown in Figure 2-1 (b)-(c). Flat disk shaped CoCrMo specimen measuring 25 mm diameter

and 2 mm thickness manufactured by BioMedtrix (Boontown, NJ) were utilized to investigate the surface roughness evolution. Two sides of the sample had different surface morphologies: one side is mirror-polished while the other surface is machined to mimic the undulating finish of modular interface with amplitude to wavelength ratio (a/λ) of 0.003 as shown in Figure 2-2.

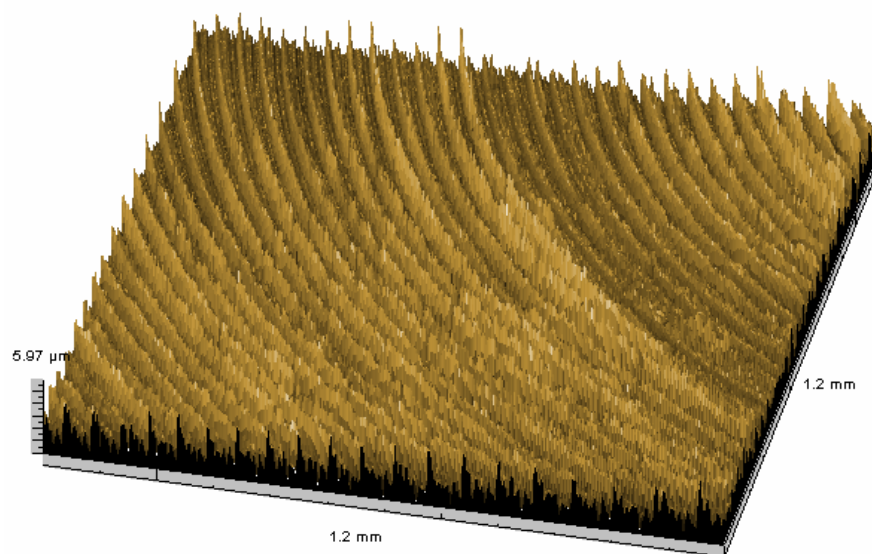


Figure 2- 2. Optical profilometer scan of the specimen surface roughness machined to undulating finish similar to modular implant interfaces (scan size: 1.2 mm × 1.2 mm)

Contact loading

Specimen surface with undulating finish are loaded by normal contact loads with a flat CoCrMo indenter as shown in Figure 2-3. Magnitude of applied contact loads is chosen so that bulk of the specimen deforms in elastic regime. Average compressive stress and corresponding contact loads applied to the specimen are listed in Table 2-1. The mirror polished side of the samples is placed on soft polyurethane substrate during contact pressing to ensure: alignment of sample and localization of the plastic deformation on the loaded side of the specimen.

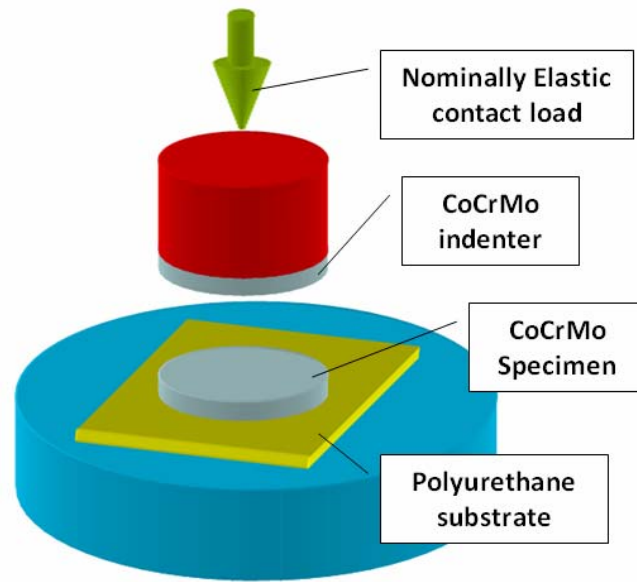


Figure 2- 3. Schematic representation of contact loading test set up

During the first stage, only repeated contact loads were applied to the specimens and in the later stage, the specimens were subjected to alternating contact loading and exposure to a reactive medium. Roughness of the loaded surface was scanned by optical profilometer after each loading and exposure to corrosive environment in order to measure the roughness evolution.

Table 2- 1. Loading levels applied on the implant specimens

	Average Contact Stress (MPa)	Load (kN)
0.4S _y	180	91
0.5S _y	225	114
0.6S _y	270	137
0.7S _y	315	160

Exposure to reactive medium

Contact loaded samples are exposed to a reactive environment to inspect the influence of contact induced residual stresses on surface dissolution of CoCrMo implant materials. Timescales involved in corrosion of implants in physiological solutions are on the order of days and months and pose significant challenges for laboratory experiments. In order to overcome this limitation, an aggressive etching medium (20 mL hydrogen chloride (HCl), 10 mL nitric acid (HNO₃), and 3 g ferric chloride (FeCl₃)) [42] is utilized to investigate influence of stress-assisted dissolution on roughness evolution of implant surfaces. The contact loaded specimen surfaces are exposed to the etching medium for two and a half minutes and roughness of the specimen surface was measured using optical profilometry before and after the etching to determine the roughness evolution. Etching tests were also conducted on unloaded specimens in order to unambiguously identify the influence of contact load induced residual stress field on surface roughness evolution.

Surface Roughness Evolution

Surface roughness of the specimens was measured with an optical profilometer, LaserScan, manufactured by Solarius Development Inc. (Sunnyvale, CA). Machined surface of the specimen were scanned from the center in radial directions along three different angles from the reference position; 0, 60, and 120 degrees in order to evaluate the overall roughness changes on the surface. For each roughness measurement, horizontal scan length and scan intervals were maintained to be 2.0 mm and 0.5 μm , respectively with vertical resolution of 100 nm. Fast Fourier Transform (FFT) of the measured roughness data was utilized to identify the roughness modes that dominate surface deformation during contact loading and exposure to corrosive medium. Amplitudes of different surface modes for the machined

surface are presented in Figure 2-4. Amplitude of each roughness mode is approximated by dividing the power spectrum by total number of data points in the roughness scan. Since the specimen surfaces are machined to an undulating profile, only a few roughness modes dominate the spectrum. Amplitude distribution of measured surface profile before and after loading is compared to measure the change in amplitude of dominant roughness modes. After contact loadings, overall shape of amplitude distribution is comparable to those before contact but the amplitude of the dominant wavelengths are reduced at corresponding frequencies as shown in Figure 2-5. Amongst all the dominant modes, roughness mode with smallest wavenumber (corresponding to $\lambda = 36 \mu\text{m}$) displays the highest change in amplitude for each contact loading and corrosion experiment. For the sake of brevity and to simplify the presentation of experimental results, only the amplitude changes of this roughness mode are discussed for the rest of this manuscript.

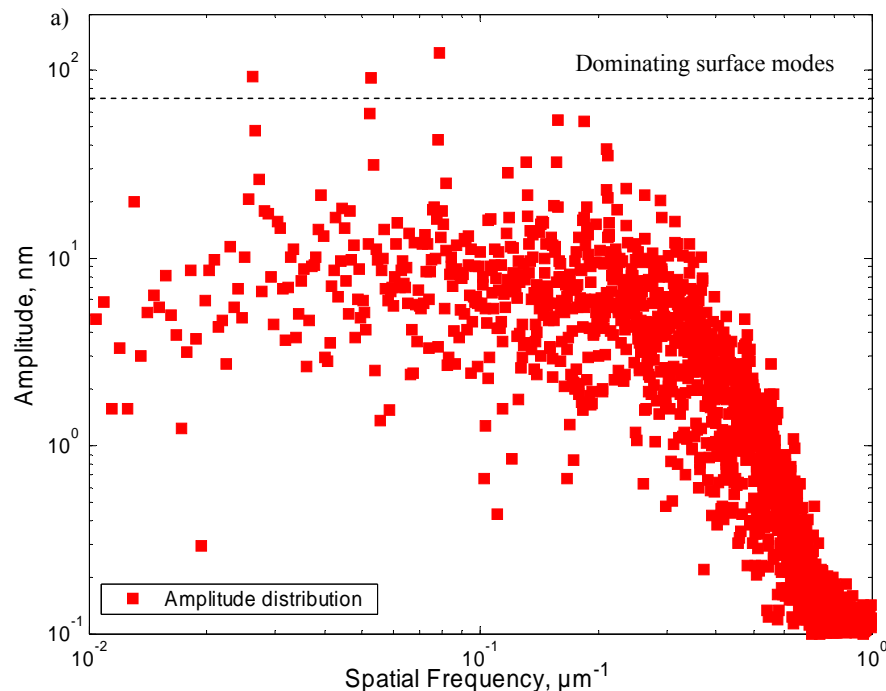


Figure 2- 4. Asperity amplitude distribution of undulating surface presented by Fast Fourier Transform

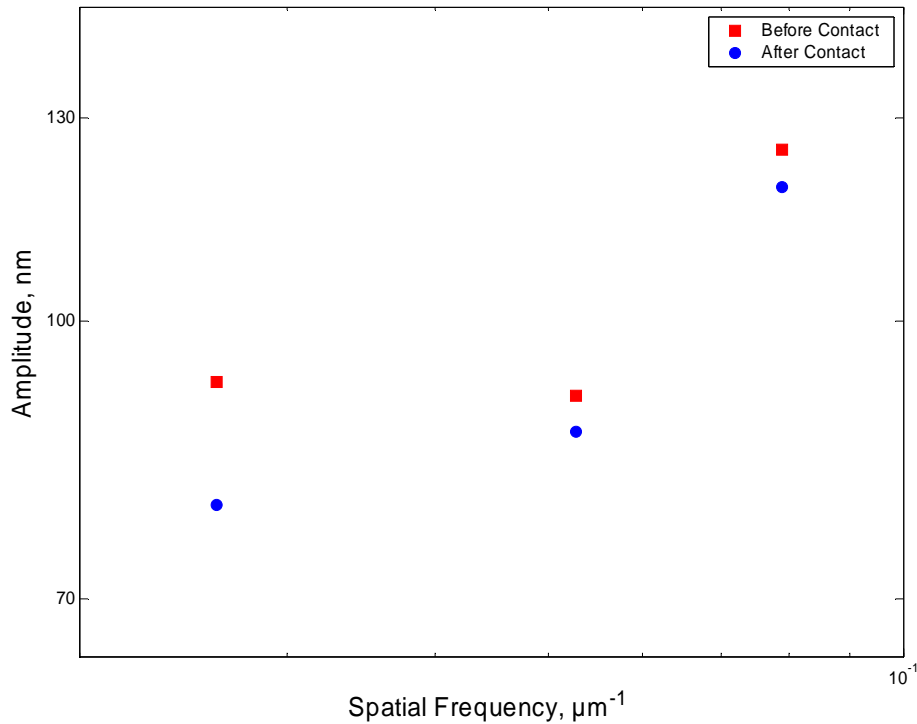


Figure 2- 5. Amplitude changes of dominant modes due to contact pressing to 70 % of specimen yield strength

Numerical Model

Finite element analysis is utilized to investigate the residual stress field developed by contact pressing of specimen surface to different loading levels. As shown in Figure 2-5, only a few roughness modes dominate the evolution of the undulating surface profile under contact loading and etching experiment. Therefore, sinusoidal surface with amplitude to wavelength ratio ($a/\lambda = 0.003$) similar to dominant roughness mode was used to simulate the residual stress development. A schematic representation of the finite element model and appropriate boundary conditions is presented in Figure 2-6.

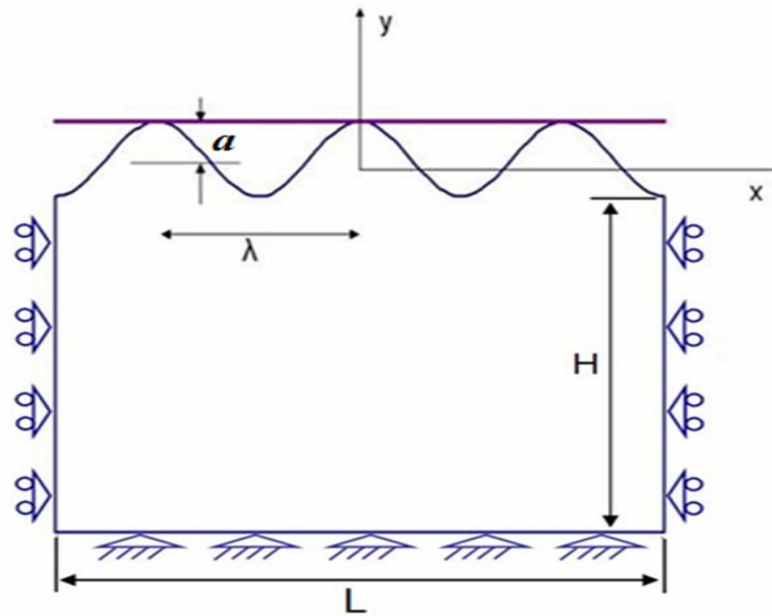


Figure 2- 6. Schematic representation of finite element model and boundary conditions

Cast cobalt-chromium alloy (CoCrMo) display significant hardening during plastic deformation [43, 44]. Therefore, local mechanical response at different locations of specimen surface is expected to vary as a function of machining as well as contact loading induced work-hardening. Primary focus of numerical calculation is to compare the residual stress states induced due to different magnitudes of contact loading. Therefore, material (CoCrMo) is assumed to be isotropic, elastic-perfectly plastic to approximate an upper bound on contact induced residual stress state. Mechanical properties utilized in the finite element model are listed in Table 2-2.

Table 2- 2. Mechanical properties of CoCrMo used in the finite element model

Property	CoCrMo (F-75)
Young's Modulus	230 GPa
Yield strength 0.2% offset	450 MPa
Poisson's ratio	0.33

Numerical model is meshed using six noded plane strain triangular elements and mesh refinement was performed to achieve numerical convergence. Finite element package, ABAQUS, is used to model the contact loading of the sinusoidal profile with a rigid flat surface. The indentation is simulated in three steps: in the first step the rigid flat penetrates onto the sinusoidal surface, and in the second and third steps the indenter is withdrawn and completely separated. A series of indentation simulation were conducted to approximate the residual stress field developed after each loading condition in order to identify the influence of residual stress field on measured surface roughness evolution.

Results and Discussion

Normalized amplitudes of the smallest wavenumber (corresponding to $\lambda = 36 \mu\text{m}$) for specimens subjected to repeated contact loading to average stress level of 60 % of the yield stress is plotted in Figure 2-7 as a function of loading cycles. Similar roughness evolution was observed for all the load levels (40 % to 70 % of yield stress). As shown in Figure 2-7, surface deformation achieves “shakedown” after the first loading i.e. amplitude reduces during the first cycle and then achieves nearly a steady value. Flattening of asperity peaks during the first cycle results in increase of contact area for each asperity and also increases the number of asperities coming in contact with the indenter during subsequent loading cycles. In addition, CoCrMo undergoes significant work hardening during plastic deformation [43, 44]. Consequently, asperities are plastically deformed only during the first loading cycle and in subsequent cycles surface deformation is elastic with little or no incremental plastic deformation [45].

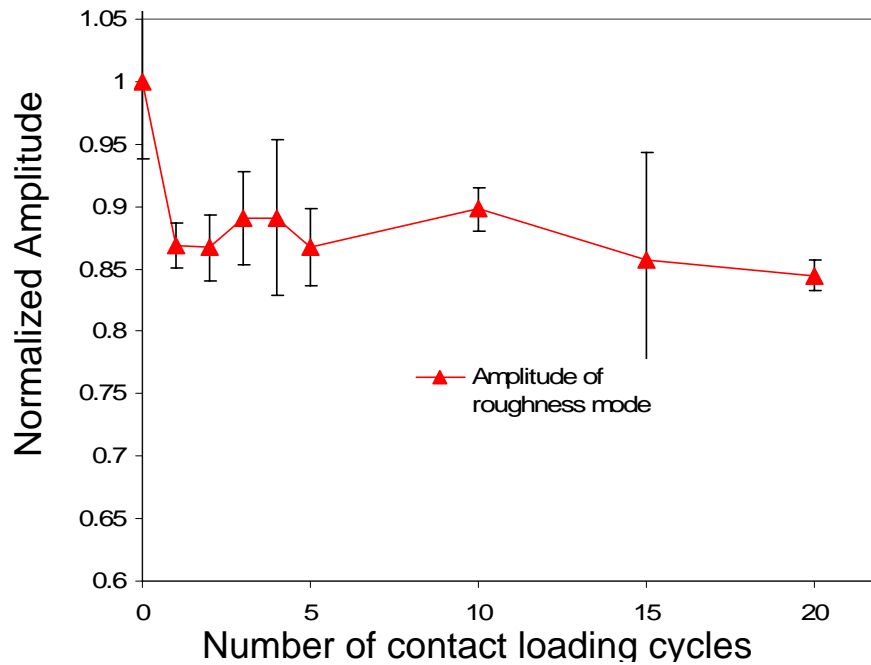


Figure 2- 7. Surface roughness evolution: normalized amplitude change over the loading cycles for contact loads of 60 % of yield strength

Surface deformation of specimens subjected to alternating contact loading and etching is plotted in Figure 2-8 for a representative loading cycle. During alternating contact loading and etching, amplitude of the smallest wavenumber (corresponding to $\lambda = 36 \mu\text{m}$) decreased during contact loading and increased on exposure to reactive environment. Magnitude of the amplitude change increases as the level of contact loading changes from 40 % to 70 % of the yield stress. Observed amplitude changes indicate the asperity peaks flatten during contact loading while exposure to corrosive medium roughens the surface. Comparable magnitudes of amplitude change are observed for each repetition of the loading cycle indicating that surface roughness continuously evolves under the combined action of mechanical loading and etching induced dissolution.

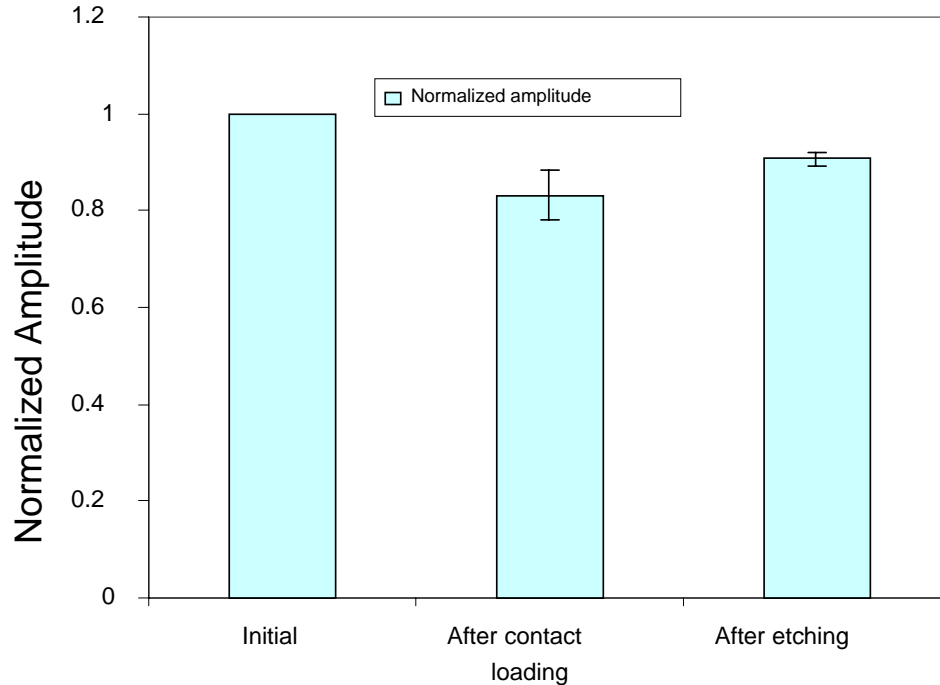


Figure 2- 8. Roughness evolution: normalized amplitude change under alternating normal contact loading to 0.7 times yield strength and etching exposure

Unloaded specimens were also exposed to the etching medium in order to clearly identify the influence of contact loading on surface corrosion. In the case of unloaded specimens, amplitude of smallest wavenumber decreased by approximately 1% during the etching tests. Spatial distribution of etching attack is different on the surfaces of unloaded and loaded specimens. Local material dissolution rate during a surface chemical reaction is accelerated due to stress and curvature because the corresponding strain and surface energies augment the free energy change associated with chemical reaction [46]. On the unstressed surface, material dissolution rate is expected to be highest at locations with positive curvature such as asperity peaks. As a result, the surface becomes flatter and amplitude of the dominant wavelength reduces during etching tests. In contrast, contact loading induced residual stress modifies the material dissolution such that surface of loaded specimen

becomes rougher and amplitude of dominant wavelength increases on exposure to corrosive medium.

Finite element calculations were performed to determine the residual stress developed due to contact pressing of specimen surface. During contact pressing, only the asperity peaks are plastically deformed and on subsequent unloading, residual stress field is developed due to the non-uniform surface deformation. Representative contour plot of residual stress developed due to contact pressing of an undulating surface (with amplitude to wavelength ratio of 0.003 and wavelength of 36 μm) to average pressure of approximately 70% of yield strength is presented in Figure 2-8. Plastic deformation of peaks leads to development of highest residual stress level at sub-surface location below the asperities [41].

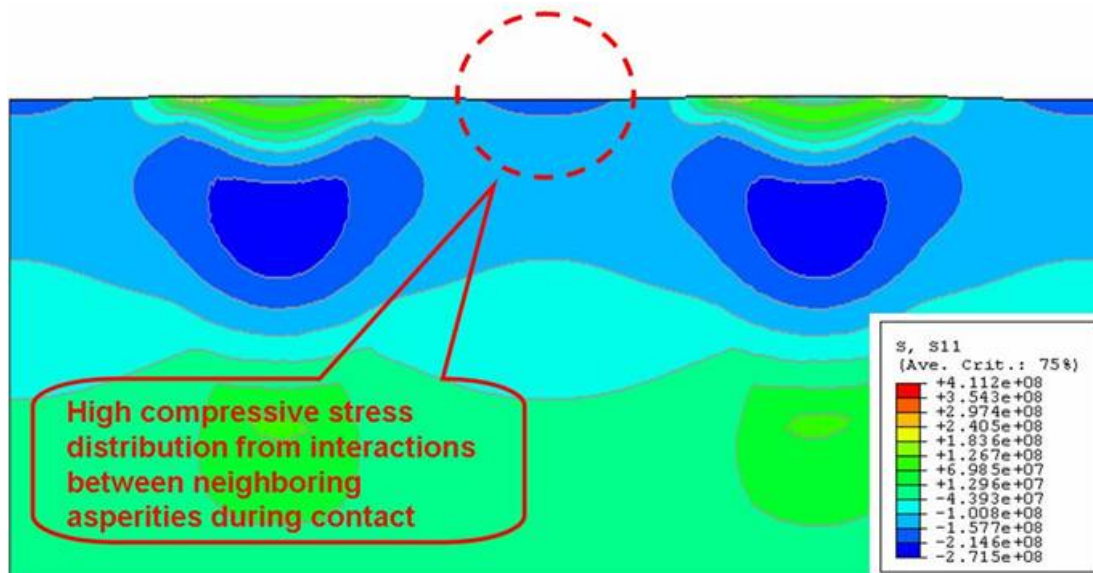


Figure 2- 9. Contour plot of contact loading induced residual stress for undulating surface loaded to 70% of σ_y

At the specimen surface, asperity peaks are relatively stress free but elastic interactions between two plastically deformed asperities leads to development of significant residual stress level at the troughs between them. Consequently, the surface residual stress

distribution is periodic with same periodicity as the surface undulations. Observed surface roughening or increase in amplitude during corrosion tests may be due to preferential removal of stressed material at the troughs of undulating surface. Average of the amplitude changes on exposure to corrosive environment measured over ten cycles are plotted as a function of normalized stress levels at the troughs for each load level in Figure 2-9, to elicit the relationship between contact-induced residual stress and corrosion. Magnitude of amplitude change strongly depends on the residual stress level developed due to contact pressing: from reduction in amplitude for unloaded specimen to about 10% increase for specimens contact pressed to the highest load.

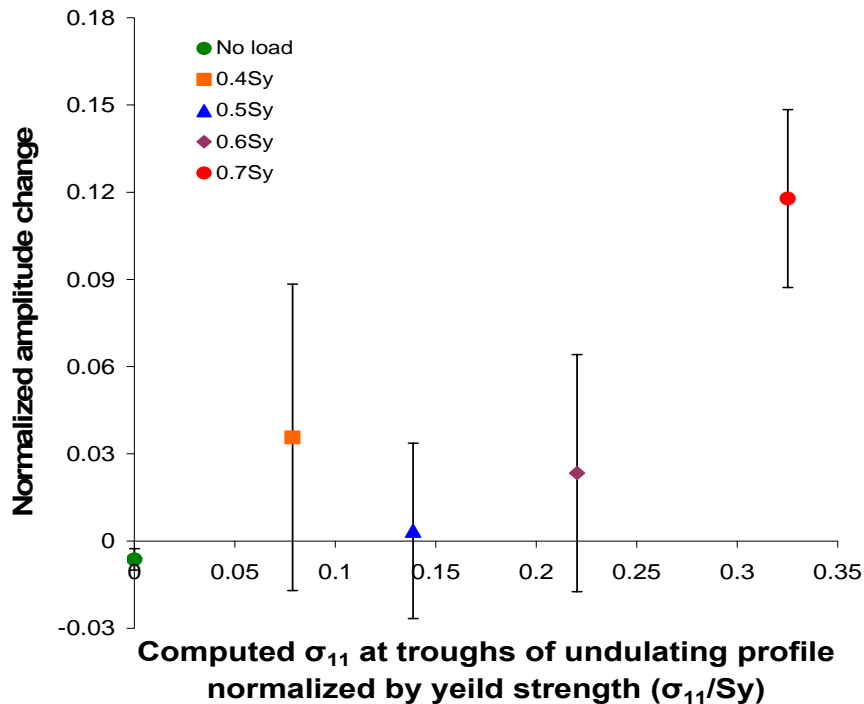


Figure 2- 10. Average of normalized amplitude change observed on exposure to corrosive medium plotted as a function of normalized residual stress level at troughs of undulating surface

The experimental and numerical results suggest that damage of implant surface under the combined action of normal contact loading and corrosive environment proceeds

according to mechanism outlined in Figure 2-9. When the implant surface comes in contact with another surface, only the protruding surface asperities are in contact. The size and distribution of the contact spots depend on the surface roughness and the applied load. Even when the overall contact loads are not large enough to cause macroscopic deformation, plastic deformation can occur in small scales under the contacting asperities so that the surface roughness changes or flattens after the removal of load. The plastic deformation under the asperity contact also leads to development of surface residual stress field. In a non-corrosive environment, repeated contacts of the surface will not lead to further damage as average contact stress is below bulk yield stress and surface deformation reaches “shakedown” after the first few loadings. However in a corrosive environment, material dissolution is accelerated at stressed location exacerbating the surface deformation. For the undulating surfaces of typical implants investigated in this paper, residual stress field distribution is such that the corrosive attack removes material from the trough increasing the amplitude or roughening the surface. As a result, the surface roughness evolves through a sequence of flattening and development of residual stress field during contact loading and subsequent roughening due to stress-assisted dissolution in a corrosive environment.

Chemical etchant used in this study is used to micro-polish Co alloy surfaces [42]. Intent of the etching experiment is to demonstrate the influence of contact induced residual stress field on local rates of chemical reaction. It may be expected that rates of surface reactions associated with *in-vivo* corrosion will also be modified in the same manner. During surface damage initiation in modular, material dissolution over the surface precedes localized pitting attack. Dissolution of implant material results in lowering of pH of surrounding medium beyond the stability of native oxide layer and leads to localized pitting attacks.

Repeated contact loading in a corrosive environment leads to surface roughness evolution and continuous dissolution of implant material through a sequence of contact induced residual stress development and stress-assisted dissolution. Surface roughness evolution may lead to damage nucleation as continuous dissolution causes differential aeration of surrounding physiological fluid [4]. The differential aeration leads to creation of a hostile HCl environment and may cause aggressive local attacks on the implant surface that ultimately results in nucleation of small cracks and breaking away of particulate debris [4]. Characterization of the transition from surface roughness evolution to crack nucleation or localized pitting corrosion is required to understand the damage mechanism but it is beyond the scope of this work. Presented experimental and numerical results provide validation for the proposed hypothesis on surface deformation during initial stages of alternating normal loads in a corrosive environment.

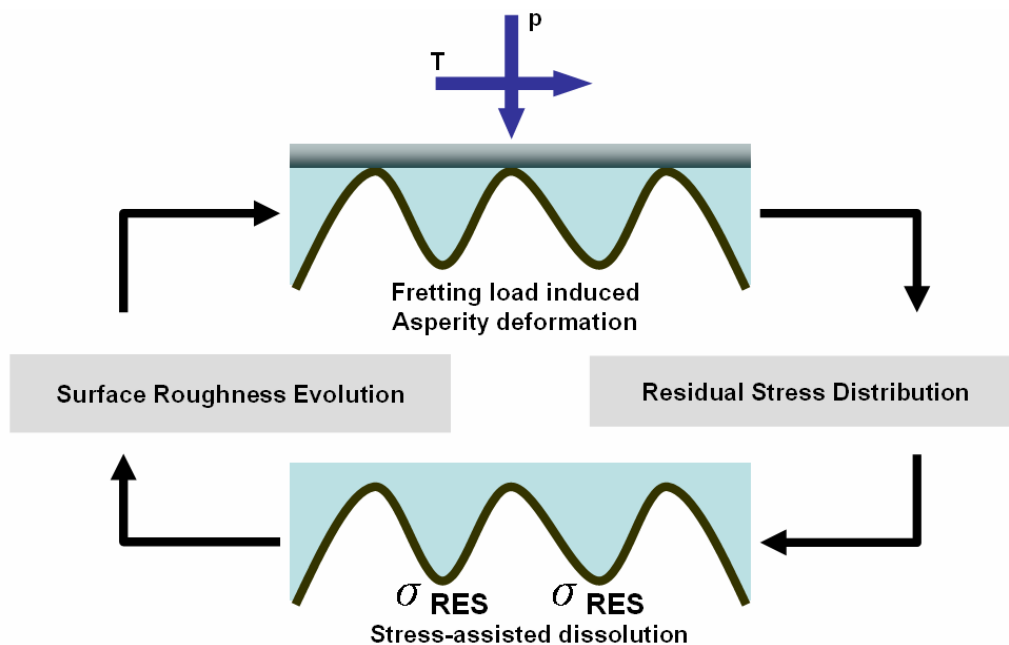


Figure 2- 11. Schematic of the proposed mechanism governing surface deformation due to combined influence of contact loading and corrosion

Conclusion

Multiple asperity contact experiments were conducted to characterize roughness evolution due to action of contact loads and exposure to corrosive environment. Cobalt-chromium specimens with undulating surface finish similar to modular implant interfaces were first subjected to only contact loading and subsequently, to alternating contact loads and etching medium. Amplitude of the dominant wavelength in surface roughness spectrum was monitored to characterize the surface roughness evolution. During repeated contact loading, amplitude reached a steady value after decreasing during the first few cycles. However during the second phase surface roughness amplitude continuously evolved – decreasing during contact loading and increasing on exposure to corrosive environment. The increase in roughness amplitude during etching depended on the magnitude of applied contact loads. Finite element analysis of the contact loading and unloading process indicated development of a significant residual stress at the trough of surface undulations due to elastic interactions of plastically deformed peaks. Based on experimental and numerical results, a damage mechanism that incorporates contact-induced residual stress development and stress-assisted dissolution is proposed to elucidate the measured surface roughness evolution.

Acknowledgments

The authors gratefully acknowledge the financial support for this research provided by Iowa State University under the Special Research Initiation Grant (SPRIG) award.

CHAPTER 3. INSTABILITY IN ROUGHNESS EVOLUTION OF METALLIC IMPLANT SURFACE UNDER CONTACT LOADING AND ELECTROCHEMICAL ETCHING

Abstract

Interface damage of modular implant such as total hip joint replacement results from repeated fretting contacts at interlocking surfaces in a physiological environment. In order to understand the influence of surface roughness characteristics on the damage mechanism, the multi-asperity contact experiments were conducted to characterize roughness evolution due to action of contact loads. Cobalt-chromium (CoCrMo) specimens with two different roughness configurations created by milling and grinding process were subjected to normal and inclined contact loading. During repeated contact loading, amplitude of surface roughness reached a steady value after decreasing during the first few cycles. During the second phase, the stressed CoCrMo surface was subjected to alternating contact loads and exposure to etchant. Surface roughness amplitude continuously evolved – decreasing during contact loading and increasing on exposure to corrosive environment. Two different instabilities could be identified in the surface roughness evolution during etching of contact loaded surfaces: increase in the amplitude of dominant wavenumber and increase in amplitude of a group of roughness modes. A damage mechanism that incorporates contact-induced residual stress development and stress-assisted dissolution is proposed to elucidate the measured instabilities in surface roughness evolution.

Introduction

Metallic materials are chosen for orthopedic implants because of their high load-bearing capacity, low cost and low wear rates. However, repeated contact loading at tapered or clamped metallic implant interfaces results in formation of soluble and particulate debris due to the simultaneous action of mechanical loading and electrochemical reactions in the corrosive physiological environment [2, 9, 17]. Previous work on understanding metallic implant surface damage due to mechanical load assisted dissolution has run the gamut from examination of retrieved implants [4, 5, 20, 47] to in-vitro implant scale experiments (see for instance [8] and references in review articles [5, 9, 17, 47]). Results of these studies indicate that there is a synergistic interaction of mechanical loading and electrochemical oxidation i.e. material degradation is accelerated by the combined effects of contact loading and corrosion. Gilbert and Jacobs have postulated that increased rate of corrosion is due to continual fracture and reformation of oxide layers (repassivation) over the metallic surfaces [4, 5]. According to this hypothesis, mechanical abrasion of oxide layer is necessary to initiate increased electrochemical activity on the surface but the role of contact loading induced residual stress distributions on the chemical reactions and roughness evolution has not been taken into account.

Previous experimental studies have shown that stress fields on a surface can influence chemical reactions and surface roughness evolution associated with corrosion, etching and material aggregation. Bundy et al. [24] have reported that application of static as well as dynamic stress leads to increased ion release from metallic implant surfaces under free corrosion conditions. Kim et al. [46] postulated that strain energy associated with applied

stress field reduces the energetic barrier associated with chemical reactions and conducted experiments that demonstrated increased rate of material removal for certain surface roughness wavelengths leading to development of characteristic patterns in roughness spectrum during nanoscale chemical etching of stressed surfaces. Barvosa-Carter et al. [48] have proposed that applied stress modifies the kinetics of surface chemical reactions and conducted experiments that show development of growth instabilities during material addition on a stressed surface.

When two rough surfaces such as implant faces forming taper-junction interface, are pressed against each other, the size and distribution of the contact spots depend on the surface roughness and the applied load. Even when the overall contact loads are not large enough to cause macroscopic deformation or fracture of oxide layers, plastic yielding can occur in small scales under the contacting asperities so that the surface roughness changes after the removal of load. Long range elastic interaction of the plastically deformed asperities may lead to development of surface residual stress field and in turn, stress-concentrations near the surface roughness grooves. In modular implants, surfaces that form the tapered junction are machined with a regular roughness pattern in order to promote interlocking [8, 17]. In an initial study on cobalt-chromium (ASTM F-76) specimens with surface finish similar to taper junction interface [49], it was found that under repeated contact loading amplitude of the dominant surface roughness mode reaches a steady value or “shake-down” after decreasing during the first few cycles. However, alternating contact loading and nanoscale chemical etching, lead to instabilities in evolution of the amplitude of dominant roughness mode – decrease during contact loading and increase on exposure to etchant. The increase in roughness amplitude during etching depended on the magnitude of applied

contact loads. Results of the study clearly demonstrated the influence of contact loading induced residual stresses on roughness evolution under nanoscale chemical etching however, several interesting questions about surface deformation were unanswered by this work: 1) How does the surface roughness evolve under combination of normal as well tangential contact loads? 3) How does the overall roughness spectrum evolve under nanoscale etching of contact loaded surfaces? 2) Will the unstable surface roughness evolution under alternating contact loading and exposure to etchant only occur on surfaces with undulating surface finishes? 4) What mechanisms and residual stress distribution underlie these processes? The purpose of this study is to help answer these questions.

Material and Methods

Specimen Configuration

Experimental investigations were carried out on cobalt-chromium-molybdenum, (CoCrMo) designated as ASTM F-75, common cobalt based alloy for the load supporting orthopedic application. Previous investigation of the alloy microstructure indicated that the average grain size is on the order of hundred microns [50]. Two different sets of flat disk shaped CoCrMo specimen (25 mm diameter and 2 mm thickness) were manufactured by BioMedtrix (Boontown, NJ) such that two sides of the specimens had different surface morphologies: one side was mirror-polished while the other surface was either machined or ground to the desired level of roughness. Rough surface of the first set of specimens was produced by machining to an undulating profile with amplitude to wavelength ratio (a/λ) between 0.003 to 0.005 in order to mimic surface finish of interfaces at taper-locked junctions [8]. While the rough surface of the other specimen set was produced by wet

grinding with a coarse grit size (240 or average particle size $53\ \mu\text{m}$) to an average roughness of $0.2\ \mu\text{m}$ (see Figure 3-1).

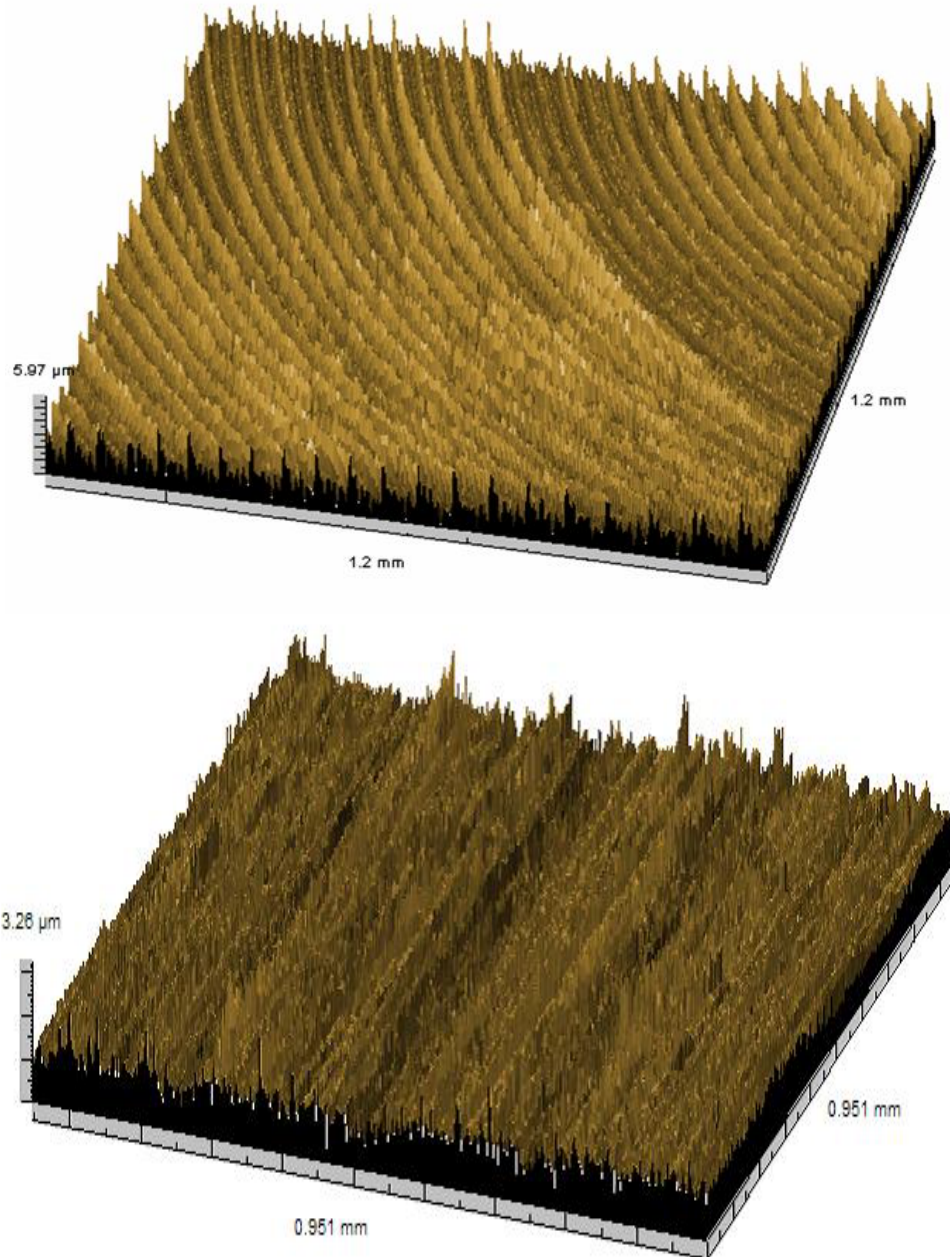


Figure 3- 1. Surface roughness of CoCrMo by milling (top) and grinding (bottom) process

Prior to experimental work, all the specimens were exposed for six minutes to a micro-polishing etchant (20 mL hydrogen chloride (HCl), 10 mL nitric acid (HNO₃), and 3 g ferric chloride (FeCl₃)) [42] and ultrasonically cleaned in distilled water.

Contact Loading

Specimen with ground and machined surface finish were contact loaded with flat CoCrMo indenter under two different contact loading configurations as shown in Figure 3-2.

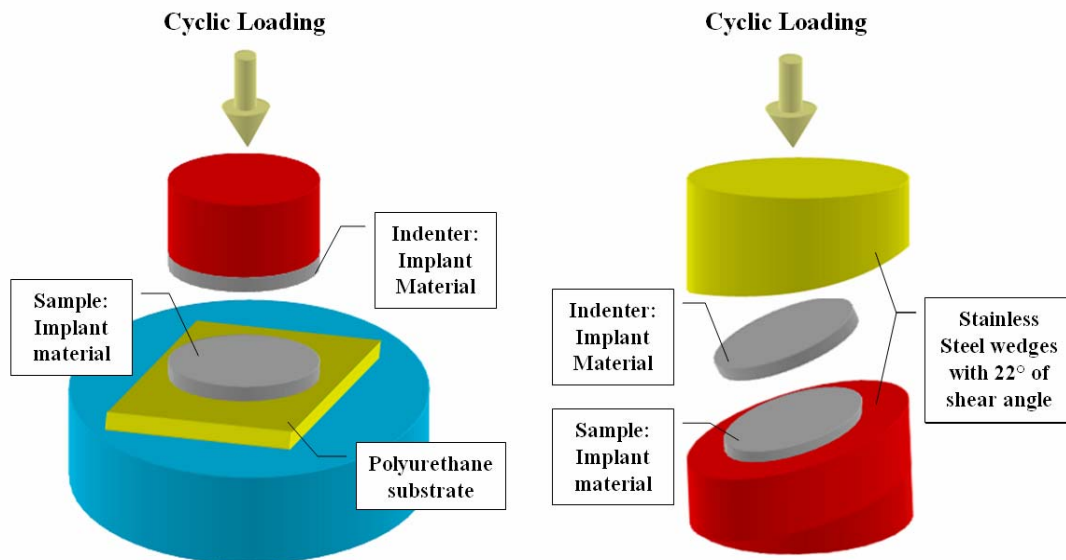


Figure 3- 2. Normal contact (left) and inclined contact (right) experimental set up

The contact pressures (p) are confined in nominally elastic regime, i.e. $0.4\sigma_y < P < 0.7\sigma_y$, where σ_y is yield strength of CoCrMo specimen. In the first configuration (shown in Figure 3-2, left), specimen were subjected to only a normal contact load while in the second configuration (shown in Figure 3-2, right), specimen surface were subjected to both normal as well as tangential loads. The mirror polished side of the specimens was placed on soft polyurethane substrate during contact pressing to ensure: alignment of sample and localization of the plastic deformation on the loaded side of the specimen. Roughness of the

loaded surface was scanned by optical profilometer before and after each loading in order to measure the roughness evolution.

Nanoscale chemical etching

Contact loaded specimen surfaces were exposed to a chemical etchant (20 mL hydrogen chloride (HCl), 10 mL nitric acid (HNO₃), and 3 g ferric chloride (FeCl₃)) for three minutes and subsequently, the etched surfaces were ultrasonically cleaned in distilled water for three minutes. Roughness of the specimen surface was measured using optical profilometry before and after the etching to determine the roughness evolution. The chemical etchant used to micro-polish cobalt chromium alloy surfaces is utilized in the experiments in order to minimize pitting and local corrosion attacks on specimen surface. [42].

Surface roughness analysis

Surface roughness of the specimens was characterized with an optical profilometer, (LaserScan, Solarius Development Inc. (Sunnyvale, CA)). Specimens with undulating surface profile were scanned from the center along a number of radial directions to evaluate the roughness changes of the surface before and after each contact and etching test. The scan size and scan intervals were maintained to be 2.0 mm and 0.5 μm , respectively. Specimens with rough surface profile were characterized by scanning along the direction perpendicular to grinding tool path. For ground surface roughness measurement, scan size and scan intervals were maintained to be 20.0 mm and 0.5 μm , respectively. In both cases, scan length was chosen such that roughness spectrum obtained from Fourier transform of acquired data is independent of scan length. Ground surfaces exhibited a wider distribution of surface heights

in comparison to undulating surfaces therefore a longer scan length was required for the former to determine the roughness spectrum.

Experimental procedure and data analysis

Four different sequences of contact loading and chemical etching used to test the two sets of specimens were: a) repeated normal contact loading; b) repeated normal and tangential contact loading; c) cycles of alternating normal contact loading and chemical etching; and d) cycles of alternating normal and tangential contact loading and chemical etching. Magnitude of applied contact loads was chosen so that bulk of the specimen deforms in elastic regime and only the asperities on the contact loaded surface undergo plastic deformation. As a control group, chemical etching experiments were also conducted on unloaded specimens in order to unambiguously identify the influence of contact load induced residual stress field on surface roughness evolution during etching. Number of specimens subjected to each sequence of loading, magnitude of applied contact loads and corresponding average normal and inclined stresses acting on the specimen surface are summarized in Table 3-1. After each contact loading and chemical etching, surface roughness was measured using optical profilometer. Roughness spectrums of the surface profile before and after the contact loading or chemical etching were determined using Fast Fourier Transform (FFT) functions of MATLAB version 6.5 (Mathworks, Natick, MA) in order to evaluate two quantities that characterize surface deformation [46, 48, 49]: change in amplitude of the dominant roughness mode for undulating surfaces and wavelength of the roughness mode undergoing largest change in amplitude.

Table 3- 1. Number of contact and etching experiment

Specimen	Type & Magnitude of loading	Pure contact	Etching	
Milled	Normal contact	0.4 σ_y	6 \square	12 \blacktriangle
		0.5 σ_y	6 \square	12 \blacktriangle
		0.6 σ_y	6 \square	12 \blacktriangle
		0.7 σ_y	6 \square	12 \blacktriangle
	Inclined contact	0.6 σ_y	4 \square	4 \diamond
		0.7 σ_y	4 \square	4 \diamond
Control group *	-	-	3	
Ground	Normal Contact	0.6 σ_y	5 \S	4 \diamond
		0.7 σ_y	5 \S	4 \diamond
	Inclined contact	0.6 σ_y	5 \S	4 \diamond
		0.7 σ_y	5 \S	4 \diamond
	Control group *	-	-	3

* Unstressed samples were etched as references to contrast the influences of contact stress on surface roughness evolution during accelerated corrosion process.

\square 6 pure contact tests (2 specimens each x 3 locations) of milled surface were conducted and 4 pure contact tests (2 specimen x 2 locations) of milled surface under tangential contact were performed respectively.

\S 5 pure contact tests (1 specimen each x 5 scans) were conducted for ground surface under normal and tangential contact conditions

\blacktriangle 12 etching tests (4 specimens x 3 locations) of milled surface stressed by normal and tangential contact were performed in the subsequent etching tests after indentations

\diamond 4 etching tests (4 specimens) were conducted after incremental indentations.

In order for the better contrast of the contact pressure dependence of roughness amplitude changes in chemical reaction, it is necessary to present statistical inference of roughness evolution of stressed surfaces compared to unstressed surface roughness changes during etching. It describes the significant relevance of roughness amplitude changes in terms of different normal contact loads, and thus the correlations between developed residual stress and roughness evolution by chemical reaction may be presumed qualitatively. Based on the estimated mean and variance of roughness amplitude, mean value (μ) of each stressed surface are compared to mean value (μ) of control group by presenting confidence interval of

differences in sample means. Smith's inference method is frequently introduced, but it is only appropriate for large sample applications [51]. The modified inference method for small sample size by Satterthwaite [52] was employed to present statistical significance since the size of sample is relatively small as shown in Table 3-2. The inference approach firstly requires approximated degrees of freedom and t -statistic level has been chosen in 95% of certainty deviation scale. It provided an approximate confidence interval which presented significance of contact pressures on degree of roughness evolution in chemical reaction.

Experimental Results and Discussion

Representative profilometry scan of the specimens with the different surface morphologies: an undulating profile produced by milling and quasi-fractal profile produced by grinding; are presented in Figure 3-3. Roughness parameters corresponding to initial surface finish for the two set of specimens is presented in Table 3-3.

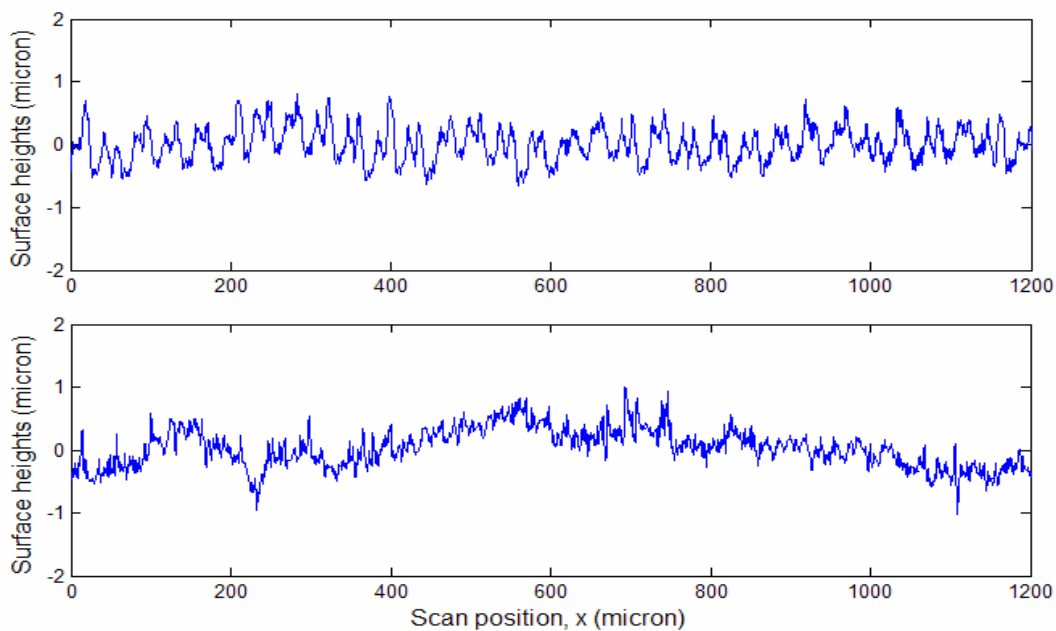


Figure 3-3. Surface roughness measured by optical profilometry; milled surface (top), ground surface (bottom)

The surface roughness condition is an important issue to be considered in the roughness evolution mechanism by contact induced stress and chemical reaction. When the center-line average and root-mean square values were compared, the milled surface displays the higher roughness amplitudes than the ground surface due to the size of cutting tool. The milling process produced undulating pattern which leads to the higher positive skewness, while the grinding process with smaller particles produced randomized surface morphology which imply the smaller radius of curvature at asperity summits at the higher spatial frequencies turning out the greater kurtosis.

Table 3- 2. Surface roughness characteristics on different surface manufacturing process (R_a , R_q , R_{sk} and R_{ku} are center-line average, root-mean-square, skewness, and kurtosis respectively)

	Ground surface	Milled surface
R_a (μm)	0.2035	0.4205
R_q (μm)	0.2647	0.5335
R_{sk}	0.2548	0.4408
R_{ku}	4.5785	3.6275

Roughness spectrum of the initial surface finish obtained by FFT calculations has been plotted in Figure 3-4. Undulating surface presented repeating roughness mode obtaining the most dominant amplitude and wavenumber while ground surface produced by grinding does not provide repeating mode and its power spectrum is similar to power spectrum of fractal noise with fractal dimension of 1.82.

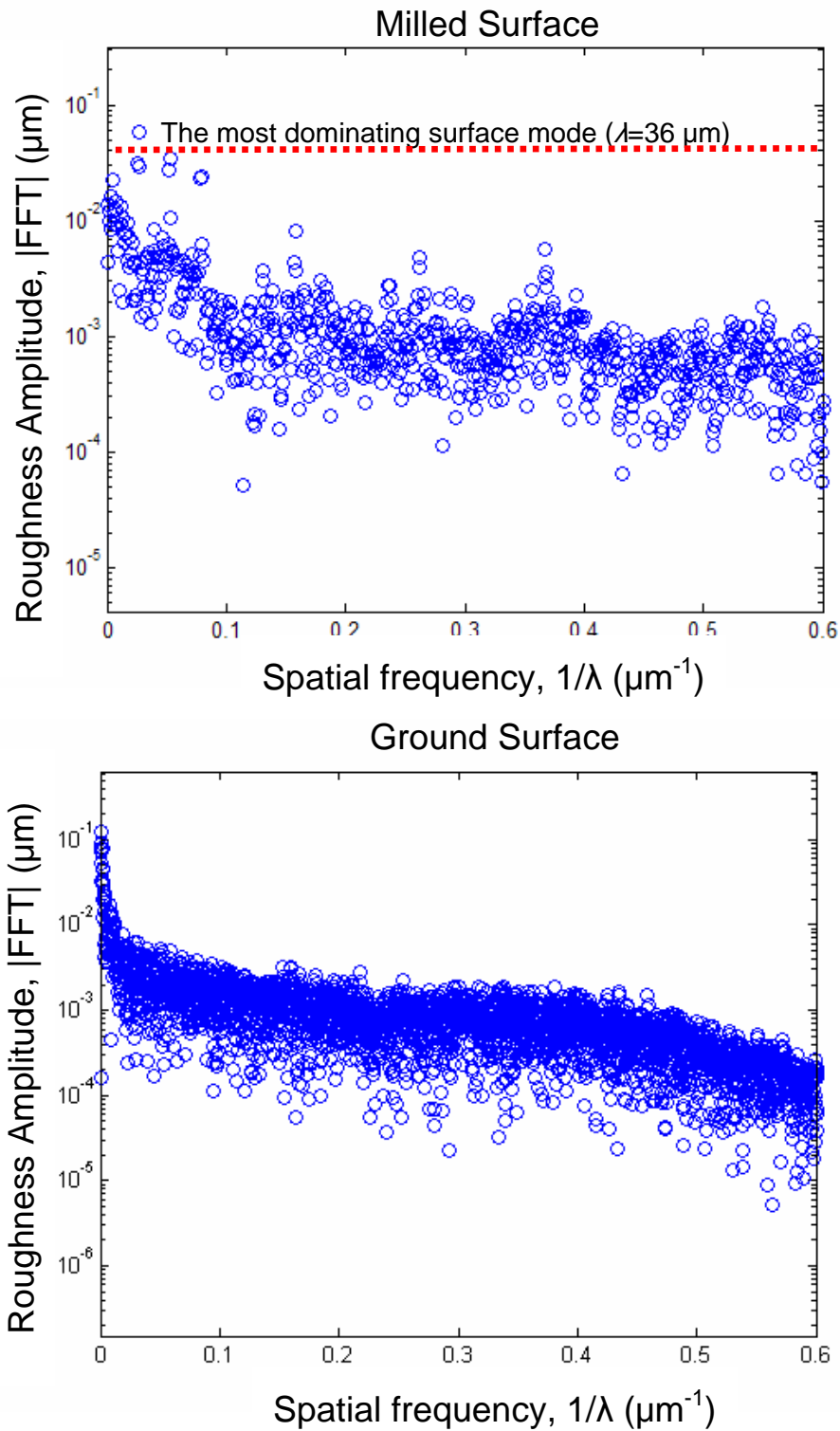


Figure 3- 4. Fast fourier transform spectrum of milled surface (top) and fractal surface (bottom); undulating surface presented the most dominant roughness mode as highlighted by red dashed line

Surface amplitude corresponding to dominant roughness mode is monitored in order to characterize the behavior of undulating surface during contact loading and nanoscale etching. Roughness amplitude changes during normal and inclined contact loading of $0.7\sigma_y$ and after subsequent etching are plotted in Figure 3-5. The amplitude of the undulating surface reduces during contact loading i.e. the surface undergoes plastic deformation establishing residual stress and work-hardening. During chemical reactions the decreased surface roughness amplitude grows. Consequently, the chemical dissolution depending on contact-induced stress state results in roughness evolution (see Figure 3-5).

In order to identify correlation between roughness evolution of undulating surface after nanoscale etching and contact loads, roughness amplitude are presented as a function of applied contact load in Figure 3-6. Magnitude of amplitude change for unloaded specimen was observed to clarify the influence of contact loading on roughness evolution in chemical reaction. In the etching experiment of the unloaded specimen, amplitude of smallest wavenumber decreased by approximately 1% during the corrosion tests.

Statistical significance of contact loads on roughness amplitude change after sequential contact loading and chemical etching processes was depicted by the relative average amplitude changes ($\mu_1 - \mu_2$) between stressed surface (μ_1) and unstressed surface (μ_2) of undulating surface. As a result, normal contact loading showed more strong relevance with roughness evolution than inclined contact while in the inclined contact loading experiment stress-induced roughness change in chemical etching does not provide significant relevance with contact pressures. In order to identify the residual stress development during normal and inclined contact loadings on the undulating surface, finite element analysis is utilized.

The undulating surface has been characterized as sinusoidal waveform based on optical profilometry measurement of Milled CoCrMo surface.

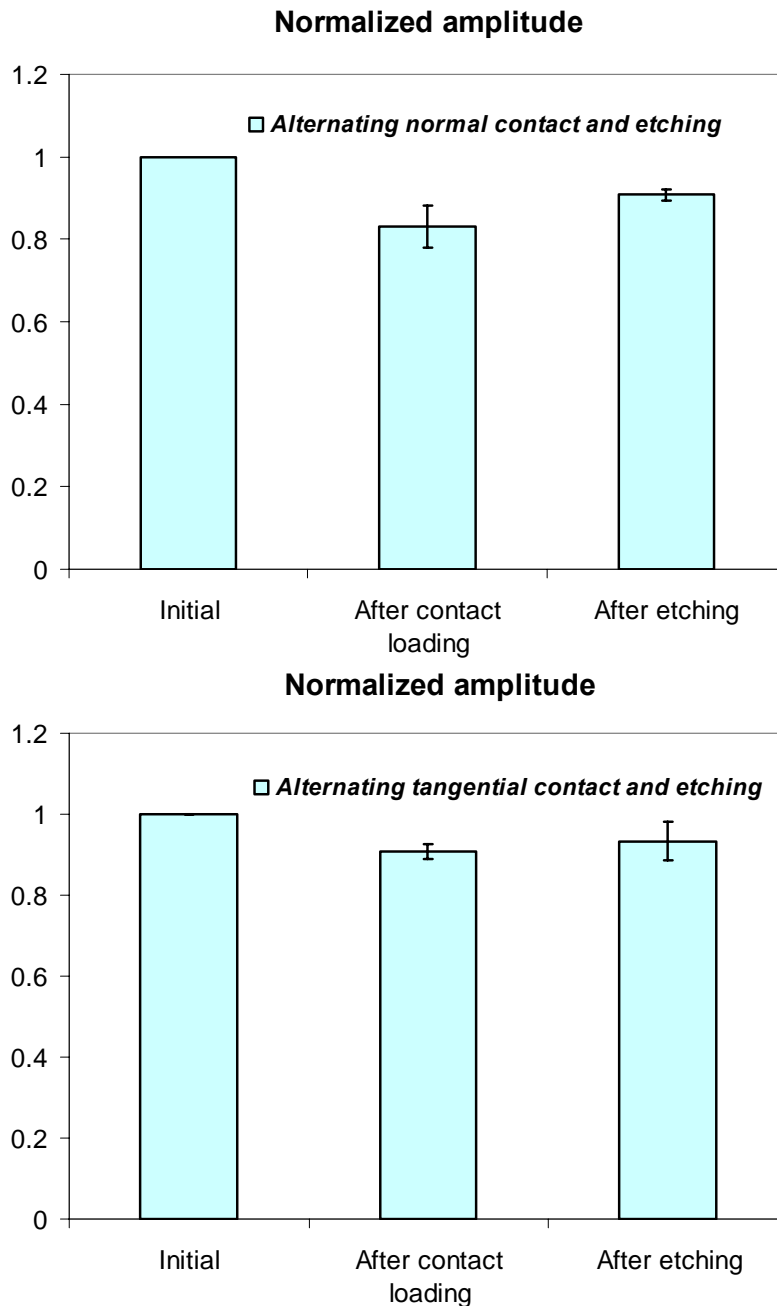


Figure 3- 5. Roughness amplitude changes by alternating normal (top) and inclined (bottom) contact and subsequent nanoscale etching (amplitudes are normalized by initial amplitude to facilitate data interpretation)

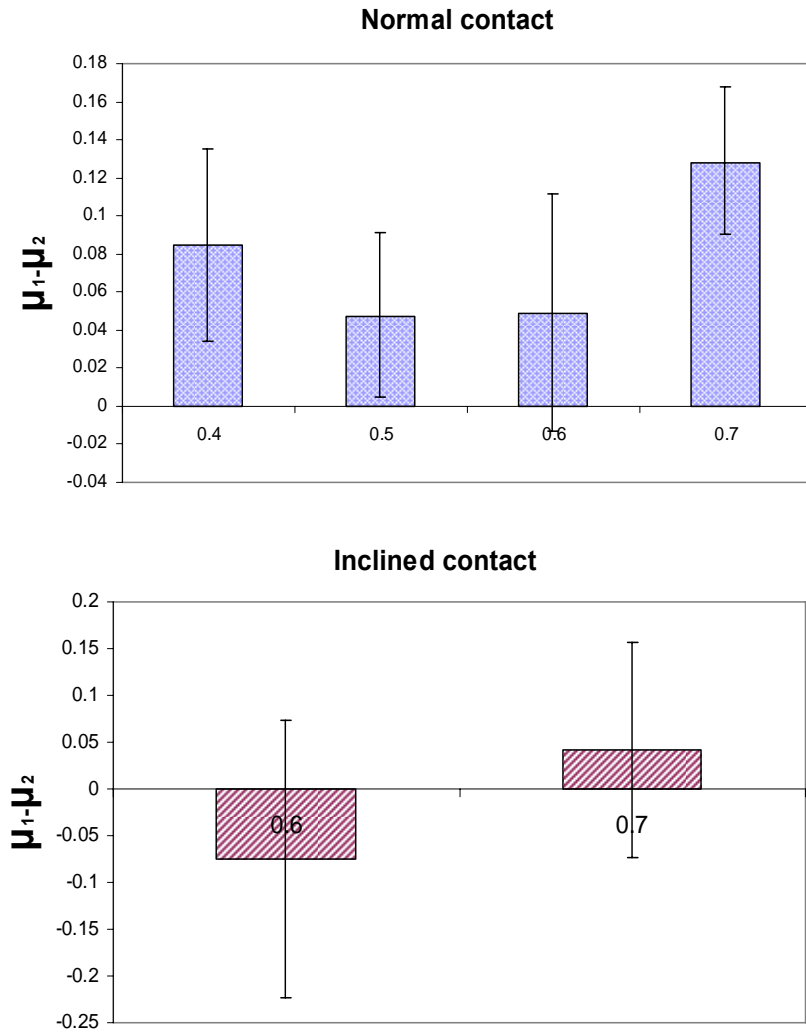


Figure 3- 6. Relative roughness amplitude changes ($\mu_1 - \mu_2$) of normal (top) and inclined (bottom) contact-stressed surface in chemical reactions. The statistical significance was evaluated by comparison with roughness amplitude change of unstressed surface after etching, where μ_1 and μ_2 are average roughness amplitude change of stressed surface and unstressed surface, respectively.

As similar to contact experiment the normal and inclined contact models were confined in elastic contact, approximately 40, 50, 60 and 70% of yield strength. Sinusoidal surface of two dimensional (plane strain) isotropic medium was created with periodic boundary conditions. Mechanical properties of cobalt-chromium alloy (cast ASTM F-75) were employed. Since cast cobalt-chromium alloy (CoCrMo) displays significant hardening

during plastic deformation, local mechanical response at different locations of specimen surface is expected to vary as a function of machining as well as contact loading induced work-hardening. However primary focus of the numerical calculation is to show the residual stress states induced due to different contact conditions. Therefore, the contact surface is assumed to be elastic perfectly-plastic under different modes of contact pressure. Numerical model is meshed using six noded triangular elements and mesh refinement was performed to achieve numerical convergence. Problem size and material properties are summarized in Table 3-3.

Table 3- 3. properties and problem size employed in FEA model

Mechanical properties		Problem size	
Young's Modulus	230 GPa	Number of elements	32734
Yield strength 0.2% offset	450 MPa	Number of nodes	101800
Poisson's ratio	0.33	Total number of variables in the model	200799

Finite element package, ABAQUS, is used to model the contact loading of the sinusoidal profile with a rigid flat surface. A series of indentation simulation with different contact loads as illustrated above was conducted to approximate the residual stress field developed due to normal and inclined contact loading. As the numerical results displayed, rough surface contact induces nonuniform surface stress depending on applied contact pressures as presented in Figure 7. Since the elastic strain caused by plastically deformed zone during unloading interacts with strain field nucleated by neighboring plastic deformation, high compressive residual stress was found at the troughs. However, stresses on the free surface near the asperity peaks may be relaxed by plastic deformation of surface during unloading process leading to lower stress states. Consequently, nonuniform residual

stress field will be generated along the undulating surface by both of the normal and tangential indentations. In addition, the frictional traction by inclined contact produces the shear motion and the stress field was modified along the tangential direction as shown in Figure 3-7.

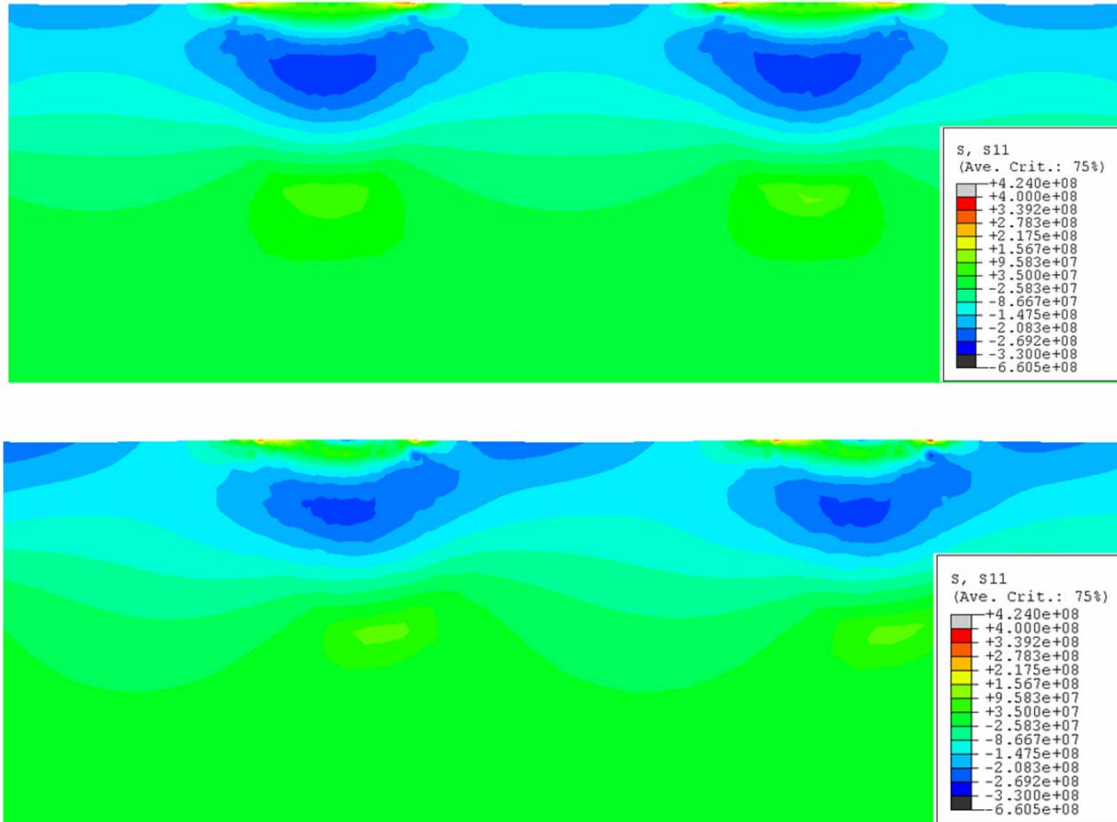


Figure 3- 7. Numerical prediction of stress field by normal (top) and inclined (bottom) contact of undulating surface.

The stressed surface exposed to corrosive environment undergoes preferential chemical reaction. Kinetics of solid surface interacting with liquid illustrates that reaction rate of solid surface is driven by chemical potential, strain energy and interfacial energy. In thermal equilibrium chemical potential can be negligible while the strain energy is significant by contact loading. The quadratic dependence between stress and roughness amplitude

changes is illustrated in Figure 3-8 by plotted amplitude changes during etching with contact-induced residual stress predicted by FEM.

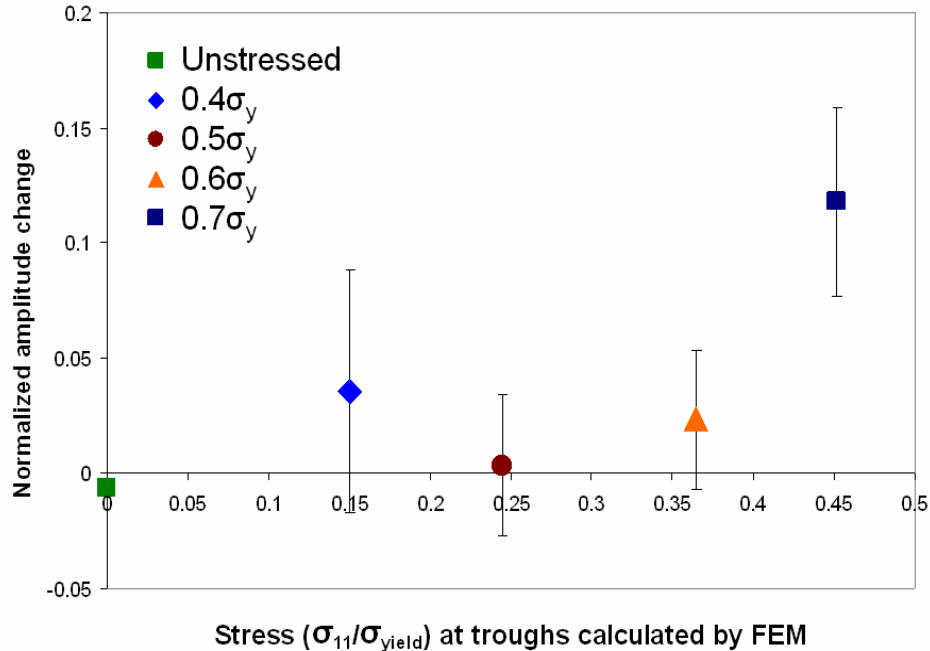


Figure 3- 8. Roughness evolution of stressed surface during chemical reaction illustrates quadratic dependence of contact induced residual stress.

Overall spectrum was observed for the ground surface roughness evolution in alternating contact loading and subsequent chemical etching experiment since the fractal spectrum doesn't present dominant roughness mode. The Fourier spectrum study dictates that more number of asperities of ground surface may be subjected to contact loading and undergo of plastic deformations resulting in less variations of residual stress. During the alternating indentation and chemical etching, the wide range of roughness modes undergoes flattening and increase in amplitude, respectively. The roughness modes were suppressed by normal and inclined contact loads while the plastically deformed roughness components grow during nanoscale etching as illustrated in Figure 3-9.

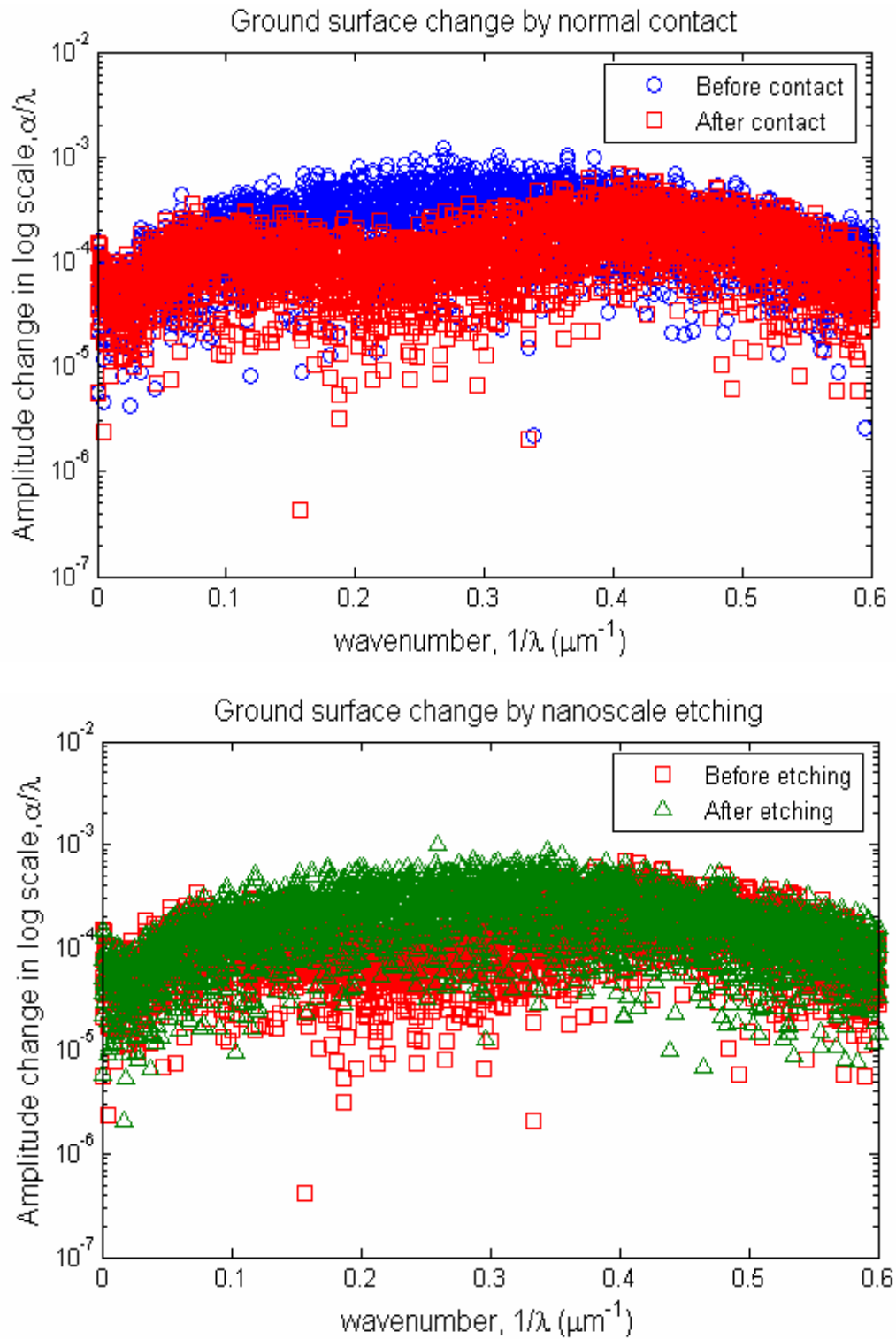


Figure 3- 9. Surface roughness evolution by alternating normal contact and nanoscale etching

As Kim et al [46] suggested surface roughness-evolution spectroscopy enables to approximate surface stress by observing critical wavelength where the roughness evolution takes place. The roughness modes of maximum evolution during chemical reaction indicate degree of surface stress developed by different types and magnitudes of contact pressures. Therefore spatial frequencies ($1/\lambda$) of roughness changes are statistically investigated on the different surface roughness configuration as well as different contact loading conditions in Figure 3-10.

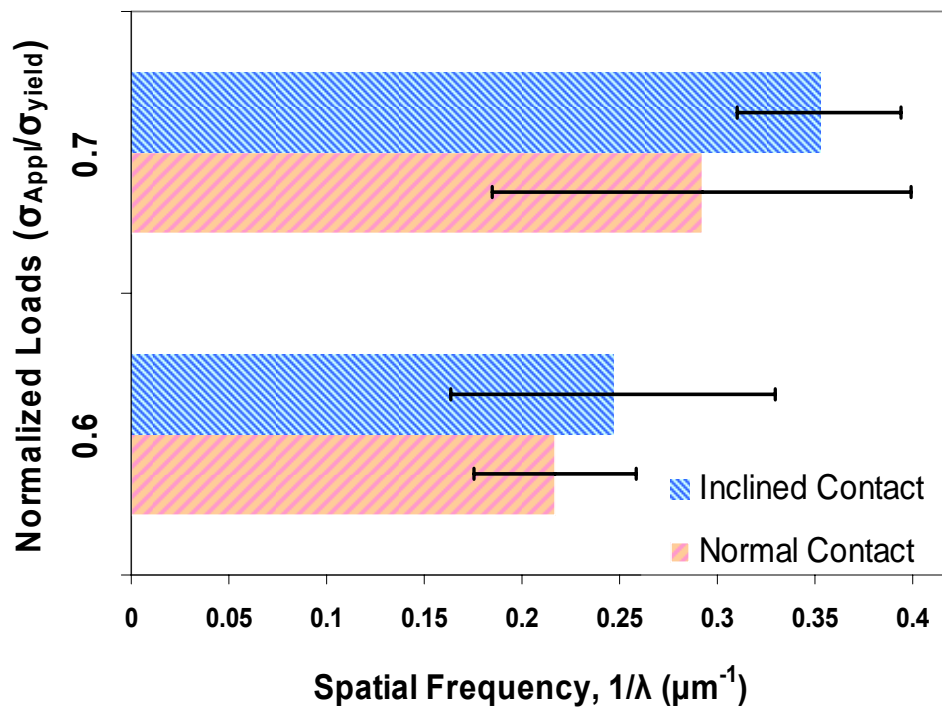


Figure 3- 10. Spatial frequency where the maximum roughness evolution takes place indicates stress state developed during contact, significant influences of magnitude of contact loads and type of indenting motions were illustrated on ground surface

Significant influence of indentation (normal vs. inclined) and magnitude of contact loads ($0.6\sigma_y$ vs. $0.7\sigma_y$) are demonstrated in Figure 3-10. Since the critical wavenumber of roughness change is proportional to square of stress state as presented by former studies [46,

53] it implies that the higher contact load and inclined contact result in the higher residual stress.

Conclusion

Multi-asperity contact experiments were performed to identify influences of surface roughness configurations and types of contact loads on roughness evolution during chemical reactions. Cobalt-chromium-molybdenum specimens manufactured to undulating surface and fractal surface morphologies were subjected to normal and inclined contact and exposed to nanoscale etching solution. For the undulating surface it was found that the most dominant surface mode decreased during both of the normal and inclined contact experiment while the suppressed roughness mode increased during exposure to etchant. FEA study indicates localized high stress region at surface troughs by residual strain after unloading stimulated by plastic deformation during contact loading. Consequently, stress-dependent dissolution rate leads to roughening of the undulating surface in the course of contact loading and exposure to corrosion. FFT spectrum observation of fractal surface contact demonstrated that group of surface roughness modes undergo decrease in amplitude due to plastic deformation during contact loading and increase in amplitude during subsequent nanoscale etching. Stress-dependence of roughness evolution of fractal surface indicates strong relevance with contact pressures and indenting motion (normal versus inclined contact).

CHAPTER 4. ANALYTICAL MODEL OF MULTI-ASPERITY CONTACT AND SURFACE INSTABILITY IN CHEMICAL REACTION: INFLUENCE OF CONTACT-INDUCED RESIDUAL STRESS AND STRESS-ASSISTED DISSOLUTION

Abstract

Roughness evolution of mechanical interface results from contact induces nonuniform stress and the stress-dependent selective corrosion attack. In many cases, surface manufacturing process produces certain degree of roughness and when the rough surface is brought into contact, the developed stress will be nonuniform depending on surface roughness conditions and contact pressures. In addition, when the stressed material is exposed to chemically active environment the stress-induced dissolution mechanism leads to surface roughness modifications. Residual stress field is approximated by an array of dilatational line embedded near an undulating surface. The depth and strength of the dilatational lines are determined by finite element computations of contact loading. Predicted stress field is utilized to predict the stress-assisted dissolution rates. Comparison of predicted and measured rate is used to determine the interfacial energy and mobility associated with nanoscale etching.

Introduction

Surface roughness is of importance in modular implant's fretting corrosion responses. At the modular interface rough surface contact nucleates local plastic deformation of contacting asperities and development of residual stress field on unloading. If the stressed surface is exposed to corrosive environment the stress-dependent dissolution leads to roughness evolution. During corrosion the kinetics of surface roughness evolution is driven by residual stress state developed by contact. Since the residual stress by contact depends on roughness condition of the contacting interfaces and contact pressure, and the surface roughness evolution in underlying corrosion environment also will be a function of surface roughness and contact loads.

Many artificial implant devices such as total hip joint replacement undergo surface degradation by stress-assisted corrosion [17]. In general implant hip joint system is composed with modular components i.e. acetabular cup, femoral head and femoral stem. Friction and wear problems at bearing surface between acetabular cup and femoral head have been improved by various technologies of compatible matching of materials, metallurgical surface property enhancement, and/or implementation of surface layer [4, 8]. However, modular interface between femoral head and femoral stem obtained by male-female fixation undergoes fretting contact by human motions and corrosion by physiological body fluid [1-3, 5, 6, 17, 18]. In order to maintain self-locking state of modular components male and female surfaces are manufactured by tapering process. The surface finish processes leads to an undulating surface with certain degrees of roughness with amplitude and wavenumber controlled by tool tip size and cutting speed. During the service life of the hip joint human

behavior brings the head-stem interface into repetitive rough surface contact leading to nonuniform residual stress field. As illustrated in the previous experimental work on roughness evolution observation under combination of contact and etching, when the stressed surface is exposed to corrosive environment, roughness will be evolved by stress-dependent selective material dissolutions [49].

Roughness evolution during surface chemical reactions is due to three contributions of chemical potential, elastic energy, and interfacial energy[46, 48, 53-57]. Chemical potential can be assumed to be constant over time and uniform over the surface and thus it is not responsible for the surface roughness changes. The interfacial potential is governed by interfacial energy density and local surface curvature. Surface energy can be approximated to be constant in thermally equilibrium condition while the varying surface curvature over the solid surface alters the local evolving action of the interface. In the case of nominally flat solid surface subjected to far-field stress, since the influence of surface stress is uniform and insignificant, elastic energy is usually considered minor during the surface roughness evolution process. However, the residually developed surface stress due to rough surface contact will result in spatial variations and will be an important factor on roughness evolution.

In order to proceed with the roughness evolution analysis it is required to estimate residual stress developed due to contact. Plastic deformation during contact loading-unloading process results in elastic stress field after complete unloading due to misfit between plastically deformed material and recovering elastically deformed material. Since the complexity of elastic-plastic contact of multi-asperity does not allow simple analytical solution, finite element model has been utilized in many cases to predict resultant stress state. In the present study similarities between elastic stress field due to line dilatation and two-

dimensional plastic contact-induced stress field is utilized to construct a residual stress field due to multi-asperity contact. However, since the size and location of plastic deformation area are required to implement line dilatation solution, finite element models were developed to calculate these parameters for varying roughness conditions and contact pressures.

This hybrid solution of surface stress would contribute to achieve simple solution of rough surface contact problem without performing FEA of different contact problems. In addition, this residual stress approximation of multi-asperity contact problem will be able to extend to roughness instability model of stressed surface in chemical reactions. Ultimately, this approach enables prediction of interface damage of modular system under fatigue contact and corrosion.

Residual stress of multi-asperity contact and Stressed surface instability in chemical reaction

Analytical model of multi-asperity contact

Residual stress developed from multi-asperity contact is due to misfitting of plastically strained region against elastically recovering region during the unloading process. Indentation model of elastic-plastic medium by Hardy presented cylindrical plastic deformation at subsurface [58]. Once contact stress of material increases beyond the yield point, stress state of the material remains at yield point while the circular plastic size expands. Finally the plastic deformation will reach free surface and further contact pressures will deform the edge of contact. During contact loading, the elastic and plastic deformation depends on contacting surface configurations as well as contact pressures while the plastically deformed region is responsible for the resultant residual stress field in unloading

process. As shown by Hardy's two-dimensional contact (plane strain) problem, cylindrical plastic deformation is established by contact loading and during unloading the plastically deformed area below contacting asperity develops elastic stress which may interact with adjacent elastic field induced by neighboring plastically deformed area. Figure 4-1 depicts maximum principal plastic strain of undulating surface after contact loading of 0.7 times material yield strength and complete unloading.

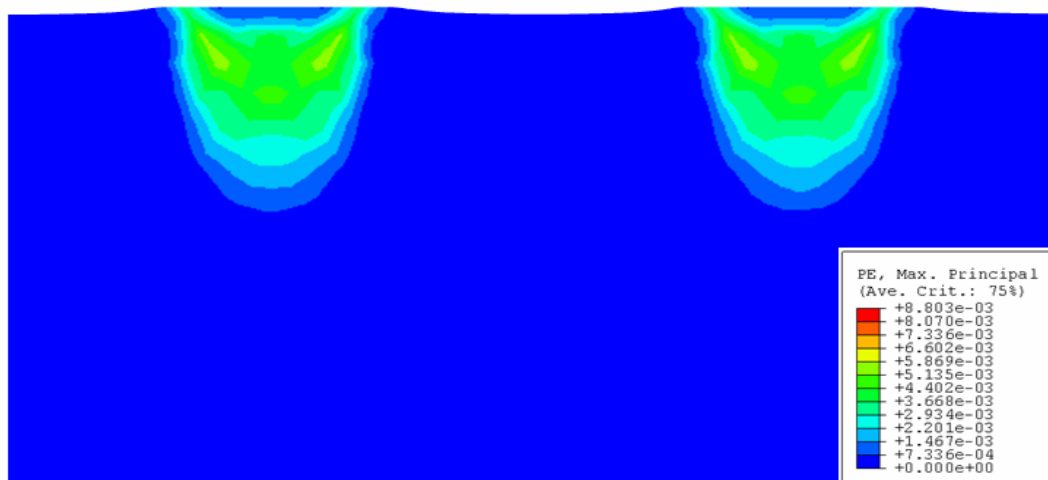


Figure 4- 1. Residually developed maximum principal plastic strain of undulating surface after contact loading-unloading

A linear perturbation analysis is utilized to approximate the residual stress field developed on the undulating surface. A nominally flat surface has been perturbed by characteristic roughness parameter i.e. the amplitude to wavelength ratio (a/λ) in the range of $0.003 < a/\lambda < 0.0125$. As shown in the elastic field around inclusion by Yu and Sanday [59] as well as elastic solution with temperature gradient around inclusion by Davies [60], the center of dilatation (CD) was employed for elastic strain sources of infinite and half-infinite medium. Similarly, for two-dimensional plastic contact inducing residual stress field,

line dilatation (LD) was introduced as a source of elastic strain field established during unloading.

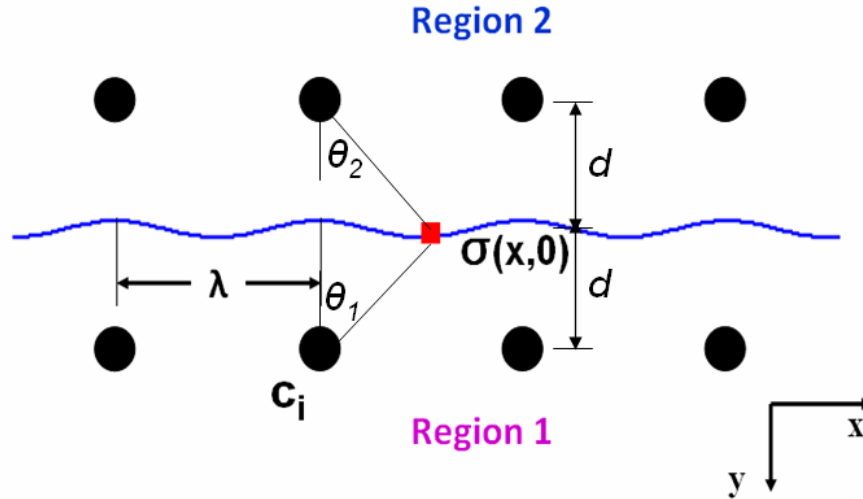


Figure 4- 2. two half-spaced (region 1 and region 2) elastic medium joined at interface with mirrored series of dilatation lines at distance of d from interface.

Residual stress field is determined as a superposition of mirrored arrays of dilatations and distributed loads that make the undulating surface traction free.

For the multi-asperity contact problem, regularly posed series of mirrored line dilatation (C_i) over the joined medium (Figure 4-2) was considered and thus stress state in the joining solids due to series of line dilatations can be obtained by superposition of stress field induced by individual line dilatation. Since our interest is confined in the joined surface, stress state at the joined interface ($y = 0$) is summarized in equation (4-1) and (4-2).

$$\sigma_{xx}^{CD} = \sum \frac{-2C_i(x_i^2 - d^2)}{[x_i^2 + d^2]^2} \quad (4-1)$$

$$\sigma_{yy}^{CD} = \sum \frac{2C_i(x_i^2 - d^2)}{[x_i^2 + d^2]^2} \quad (4-2)$$

Distributed stresses were applied to meet the traction free boundary condition at the perturbed surface of Region 1. By utilizing small perturbation ($a/\lambda \approx 0$) of the surface, final surface stress state was obtained by adding stress field due to equal and opposite surface traction (σ_{ij}^t) on stress state by series of line dilatations (σ_{ij}^c) as depicted in Figure 4-3.

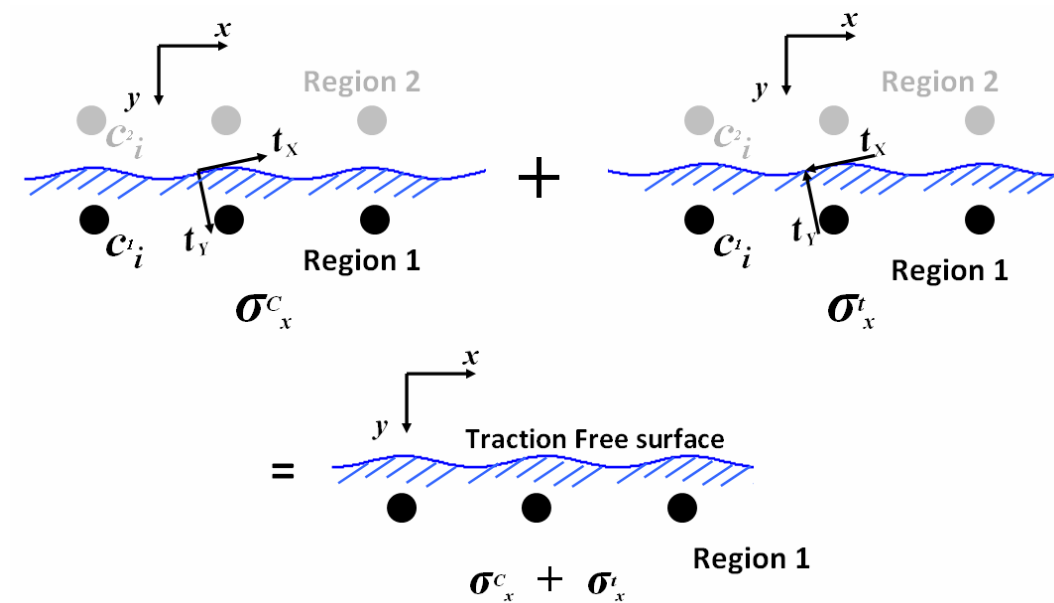


Figure 4- 3. In order to obtain traction free boundary condition on the perturbed surface, stress field due to equal and opposite surface tractions was superposed to stress field due to series of mirrored line dilatations.

However, the strength (C_i) and the location (d) of line dilatation have to be identified to obtain complete stress field, and thus finite element analysis was employed for varying surface perturbations and contact pressures. Finite element models of contact problem with different roughness characteristics ($0.003 < a/\lambda < 0.0125$) and nominal contact pressures ($0.4\sigma_y$, $0.5\sigma_y$, $0.6\sigma_y$ and $0.7\sigma_y$, where σ_y is yield strength of the solid) were conducted to predict the strength and location of line dilatation. The sinusoidal surface is approximated to two dimensional isotropic continuum medium specified by mechanical

properties of cobalt-chromium alloy (cast ASTM F-75) with periodic boundary conditions and perfectly rigid surface is employed for the indenting surface as illustrated in Figure 4-4.

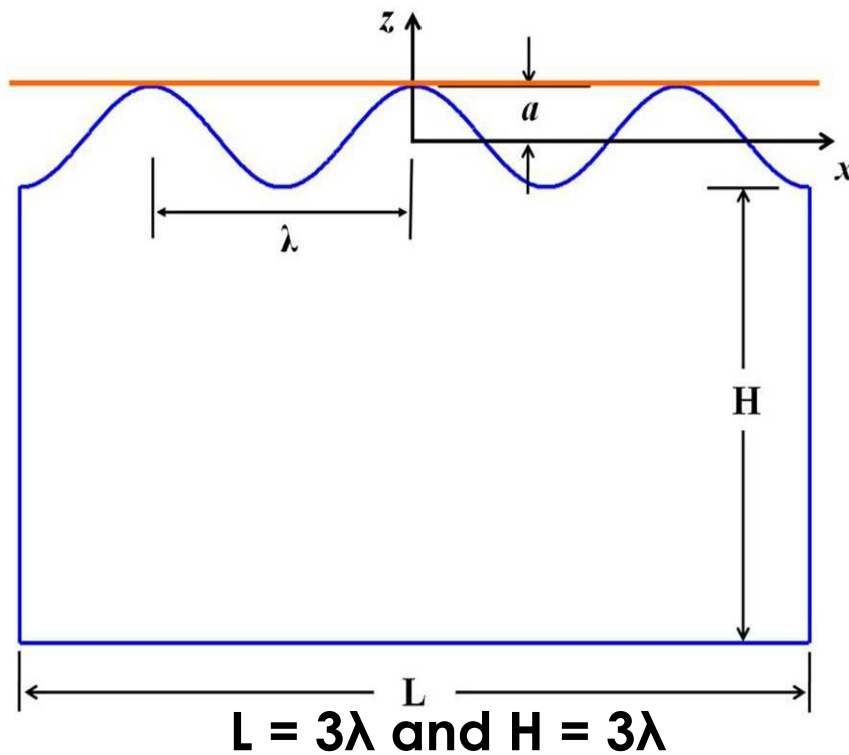


Figure 4- 4. Finite element model was characterized as an elastic-perfectly plastic plane strain body. Surface roughness is parameterized by amplitude to wavelength ratio in the range of $0.003 < a/\lambda < 0.0125$ and contact loadings are characterized in the range of $0.4\sigma_y < P < 0.7\sigma_y$ where σ_y is yield strength of the contact medium

Triangular quadratic elements were created and mesh refinement was performed to achieve numerical convergence. Problem size and material properties are tabulated as Table 1 illustrates. Finite element package, *ABAQUS*, was utilized to perform a series of contact simulations resulting in the residual stress field developed after contact loading-unloading process. Influence of surface roughness amplitude and contact loads was investigated to identify surface residual stress near contacting asperities as well as troughs between neighboring asperities.

Table 4- 1. Description of Finite element model

Mechanical properties		Problem size	
Young's modulus	230 Gpa	Number of elements	32734
Yield strength 0.2% offset	450 Mpa	Number of nodes	101800
Poisson's ratio	0.33	Total number of variables	200799

The strength and location of line dilatation was estimated from FEA results and mapped in terms of roughness parameters (a/λ) and contact pressures (P) so as to identify surface stress stimulated by local plastic deformation of multi-asperity surface.

Instability of stressed surface in chemical interaction

The kinetic model of stressed surface instability in chemical reactions is governed by surface mobility (M) in thermally stimulated state combined with driving force (F) which varies with strain energy and surface roughness with small perturbation;

$$R = MF \quad (4-3)$$

$$F = g - U_{SE} - K\gamma \quad (4-4)$$

where g is chemical energy density, U_{SE} is strain energy density and K and γ are local radius curvature and interface energy respectively. Based on the surface stress state estimated by line dilatation solution and finite element analysis, elastic strain energy can be determined and surface curvature also can be obtained by second order differentiation of the surface characterized by small perturbation. The perturbed surface was sinusoidal wavy profile with small amplitude to wavelength ratio ($0.003 < a/\lambda < 0.0125$). Therefore the reaction rate of stressed surface during chemical reaction can be mathematically expressed as;

$$R = \frac{dH_o}{dt} + \frac{\partial h}{\partial t} = M \left(g - \frac{\sigma^2}{2E} - K\gamma \right) \quad (4-5)$$

where H_o is average height of the surface and h is local height as a function of location and time, $h(x,t)$. Surface function (h) was approximated as sinusoidal configuration by roughness amplitude (a) and wavelength (λ) measured by optical profilometry of milled CoCrMo surface, $h(x,0) = a \cos\left(\frac{2\pi x}{\lambda}\right)$, as a function of location while assumed as independent of time. The local solid surface curvature was obtained by second order differentiation of surface function (h) before etching ($t=0$) i.e. $K = \frac{\partial^2 h(x,0)}{\partial x^2}$. Change in amplitude can be estimated if the reaction rate at asperity summits and troughs are known for given time span of exposure and in addition it enables to determine whether roughening or flattening takes place during the stressed surface chemical reaction.

Experimental measurement of surface instability by contact-induced stress and corrosion

Stress dependence of solid dissolution rate was evaluated by combined experiment of normal contact and nanoscale etching. In order to identify mechanism of roughness instability, milled cobalt-chromium-molybdenum (CoCrMo, cast ASTM F-75) specimen was subjected to elastic contact loads as shown in Figure 4-5. The nominal elastic contact loads are confined as $0.4\sigma_y$, $0.5\sigma_y$, $0.6\sigma_y$ and $0.7\sigma_y$, where σ_y is yield strength of CoCrMo. Subsequently, the contact-stressed CoCrMo was exposed to strong acidic solution of 20 ml HCl , 10 ml HNO_3 and 3 g $FeCl_3$ for 3 minutes. Since milling process creates regularly

undulating surface (Figure 4-5) and only the protruding asperities are in contact, normal contact will nucleate local plastic deformation leading to nonuniform residual stress.

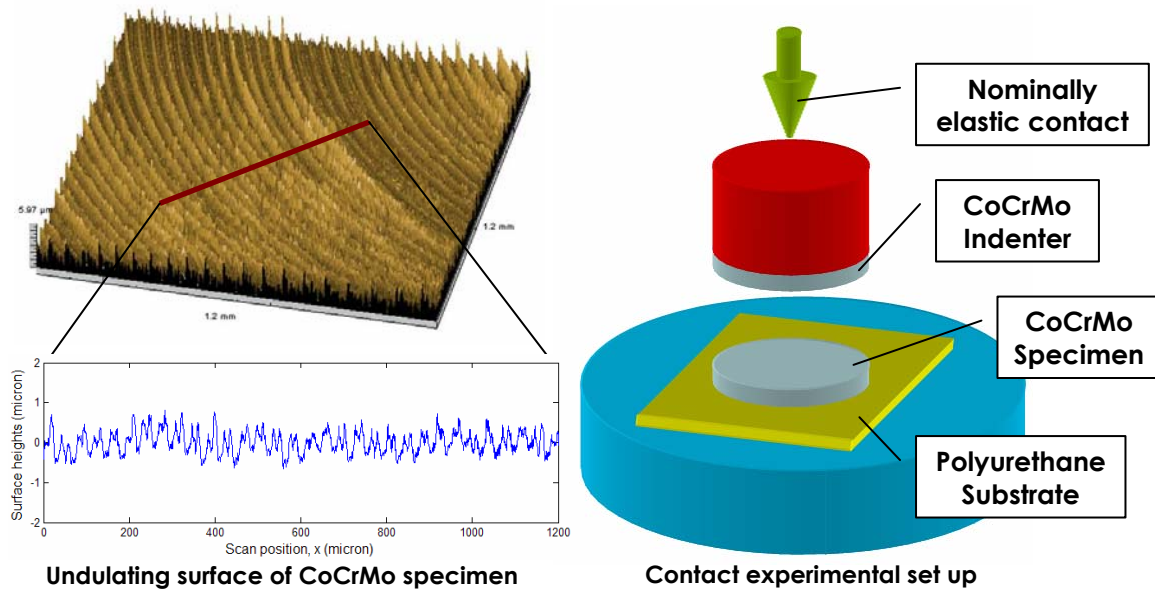


Figure 4- 5. Specimen surface roughness and normal contact experimental set up

During exposure to etchant preferential material dissolution takes place depending upon local stress states. The surface roughness changes were measured by optical profilometry before and after each contact and etching test. Fast Fourier Transform (FFT) calculations were used to determine evolution of dominant roughness mode with amplitude to wavelength ratio of $a/\lambda \approx 0.003$ for the milled CoCrMo surface.

Results

Numerical superposition of local stress state obtained by series sum (equation (4-1) and (4-2)) is used to calculate stress value at troughs for particular surface perturbation and nominal contact pressure.

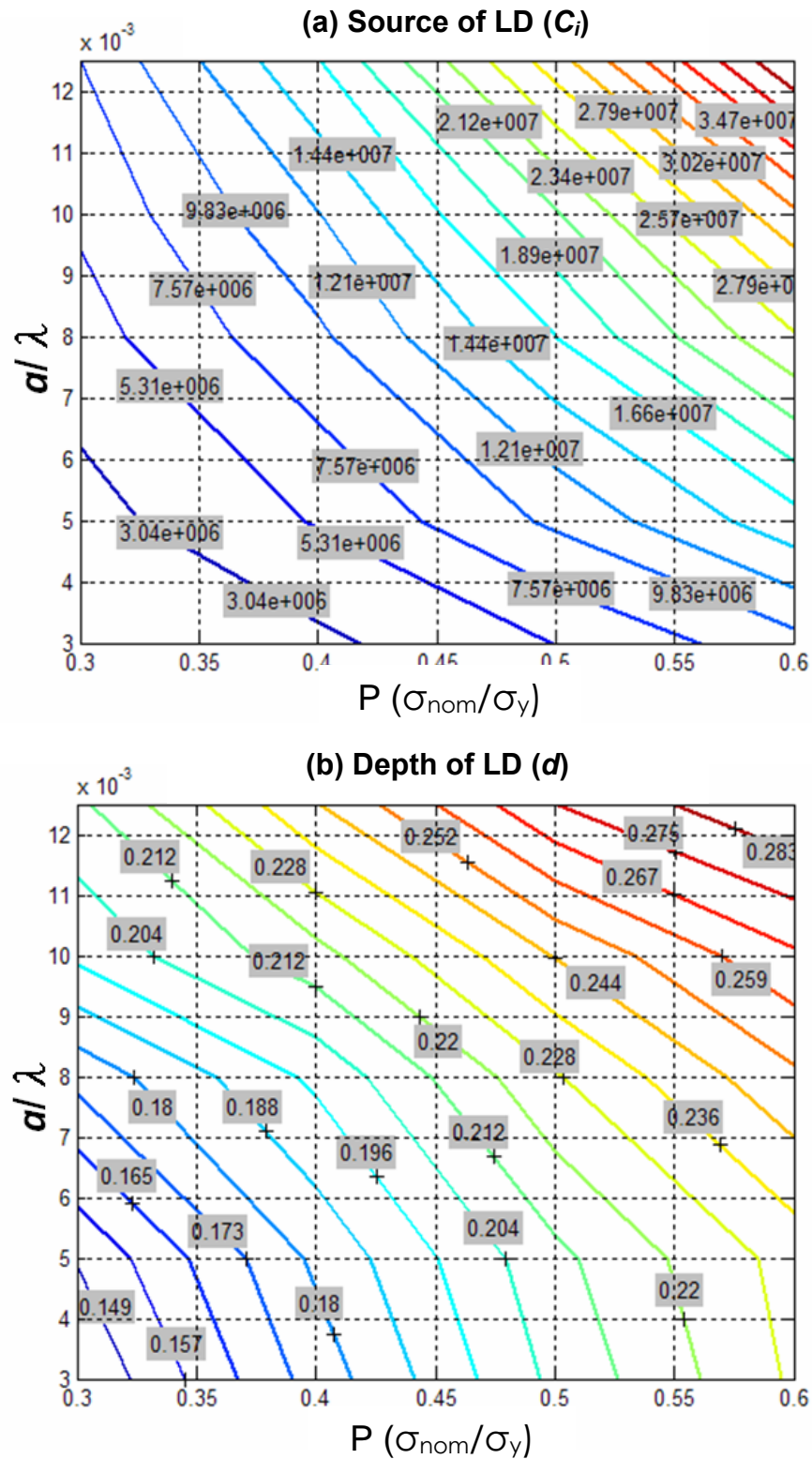


Figure 4- 6. Source and (b) depth of line dilatation map predicted by matching with FEM in terms of roughness and nominal contact pressures.

Analytical prediction of stresses in trough were compared with FEA result to map the dilatation sources (C_i) and depths (d) with respect to roughness parameter (a/λ) and nominal contact pressures (P). Predicted dilatation strength and location corresponding to different (a/λ) and contact load are depicted in Figure 4-6 (a)-(b). Utilizing proposed maps of source and depth of line dilatation, residual stress localized at troughs will be able to approximated if the surface roughness is characterized as undulating waviness in the range of $0.003 < a/\lambda < 0.0125$ as well as nominal contact loads are confined between $0.4\sigma_y$ and $0.7\sigma_y$.

Stress-dependent roughness evolution model was developed based on the local surface stress at troughs determined by hybrid solution of multi-asperity contact while it is assumed that the asperity tip is stress free on complete unloading. As expressed in equation (4-5) reaction rate has quadratic dependence on the stress field. Similar quadratic dependence was observed in experimental measurement of amplitude changes. During consecutive contact-etching experiment the milled surface roughness evolved i.e. decrease in roughness amplitude during contact and increase during etching. Consequently, the experimental results provided rate of evolution during chemical reaction as a function of surface stress. The correlation between contact-induced surface stress by proposed line dilatation model and relative amplitude changes, $\Delta h_s - \Delta h_t$, is presented in Figure 4-7 (b). In addition, this hybrid approach enables to approximate surface mobility (M) and surface energy (γ) by least square fitting technique as shown in Figure 4-7 (b). The fitted curve based on quadratic relations between experimentally measured roughness changes after etching, $(\Delta h_s - \Delta h_t)$ and residual stress predicted by line dilatation model of multi-asperity

contact, indicates that solid surface mobility (M) and interfacial energy (γ) during dissolution are approximately $2.78 \times 10^{-13} \text{ m}^3 / \text{N sec}$ and $0.352 \text{ J} / \text{m}^2$, respectively.

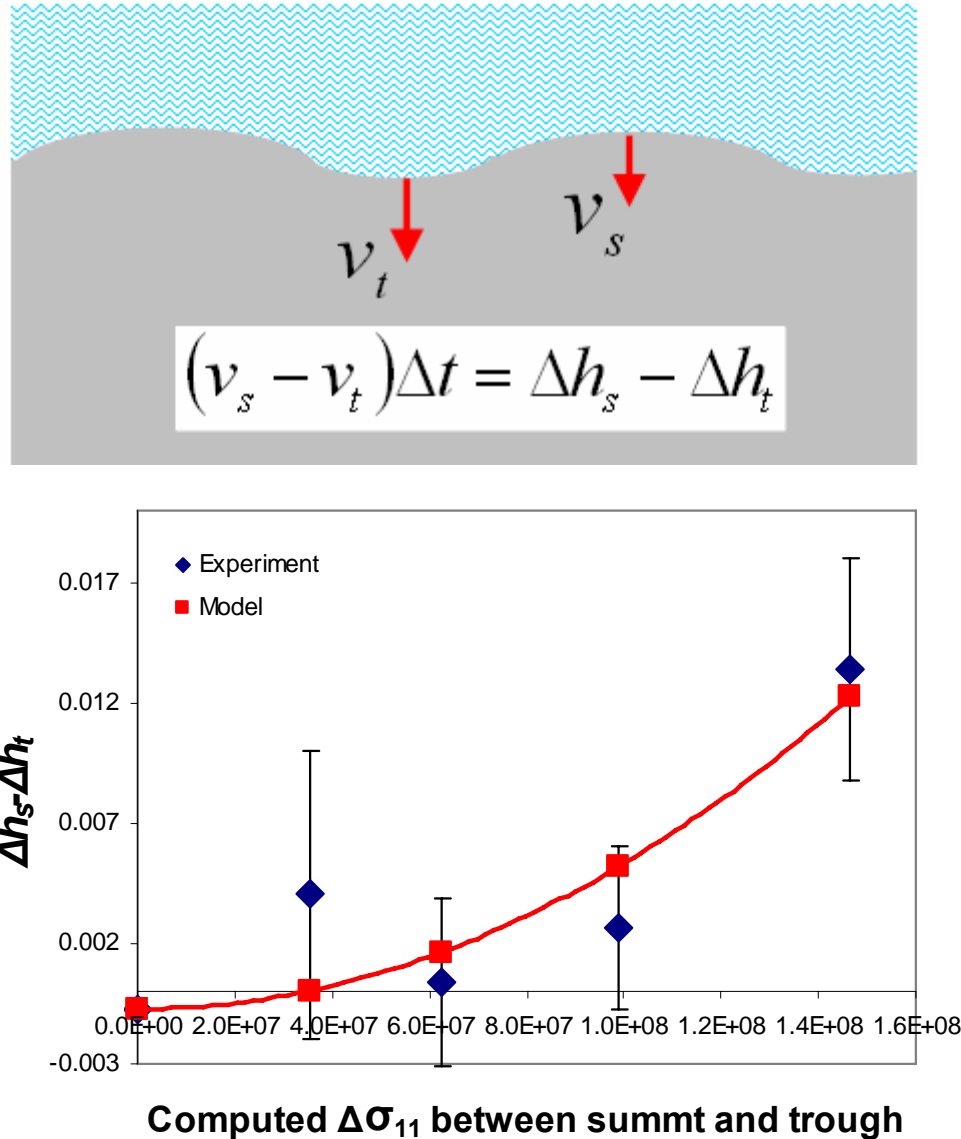


Figure 4- 7. (a) Roughness evolution depends on surface stress state at asperity summits and troughs, (b) quadratic correlation of chemical reaction rate (Δh) and residual stress developed by contact

The interfacial surface energy is comparable with the values obtained from entropy method and value Kim suggested in his surface roughness-evolution spectroscopy [46, 61].

From this method it is possible to predict rate of roughness instability of CoCrMo surface exposed to the etchant under given surface roughness configuration and contact pressures.

Conclusion

From experimental study of undulating surface instability, it has been postulated that rough surface contact results in nonuniform residual stress and nonuniform chemical potentials along the exposed surface. Undulating surface manufactured by milling process creates localized residually stressed area by the course of plastic deformation of contact asperities during loading and elastic strain during unloading. The residual stress may be determined by mismatch between plastic deformation and surrounding materials. The similarity of center of dilation and plastic deformation of contact asperity enables development of multi-asperity contact induced residual stress model. This model was combined with finite element analysis to characterize the residual stress pattern along the wavy surface. Stress dependent surface kinetic solution was expanded based on the stress state characterized in the line dilatation model. Local electrochemical reactions governed by stress suggested roughness evolution process and also new method of determining surface mobility and interfacial energy associated with nanoscale chemical etching.

CHAPTER 5. DELAMINATION WEAR MECHANISM BY FATIGUE CRACK GROWTH DUE TO SLIDING CONTACT OF SINGLE ASPERITY: INFLUENCE OF RESIDUAL STRESS ON CRACK GROWTH RATE

Abstract

Residual stress plays an important role in fatigue fracture, namely, many practical examples have shown that residual stress developed during machining processes affects service life. While it is well known that the compressive residual stress field is beneficial to delay material failure, but experimental study of single asperity by Mitchell and Shrotriya indicate that the residual compression enhances wear rate, whereas residual tension suppresses wear rate during sliding contact [62]. In order to elucidate the wear mechanism of contact problem in the presence of residual stresses, analytical model of delamination wear combined with surface layer spalling analysis has been developed. By investigating cyclic stress intensity factors (ΔK) during sliding contact under compressive and tensile in-plane stress, it is suggested that compressive residual stress increase the crack driving force and consequently increase wear rate during sliding contact.

Introduction

Wear is a process of material loss by fracture of interacting surface layers. This surface damage is due to the interacting surface roughness, deformation of the material by loading, environment, as well as formerly developed residual stress state. When a surface is brought in cyclic sliding contact, the material undergoes repeated compression and tension, and pre-existing subsurface defects turn into microcracks. If the microcrack reaches threshold length crack growth initiates by subsequent alternating elastic tension and compression. For example, fretting contact is a major issue of modular implant failure. Due to human actions like walking, jogging, and running, modular implants such as total hip joint replacement are subjected to repetitive microscale contact at the modular interface producing wear particles during service life of the implant.

In order to investigate the wear mechanism, delamination wear theory by Suh [63-67] was employed. He proposed subsurface crack propagation parallel to free surface which produces lamellar wear particles during continuous sliding. Sliding motion of contacting asperity initiates dislocation activity and relatively high concentration of dislocations at subsurface. In the subsequent sliding motion dislocations pile up and grow into subsurface microcracks. Microcracks propagate or coalesce with neighboring cracks due to shear motion of surface layer during sliding contact. Suh numerically estimated stress intensity factor in order to identify the delamination depth in terms of elastic stress field induced by sliding contact with varying friction coefficients. His numerical study showed that wear depth was determined by location of maximum stress intensity factor of a subsurface crack.

The influence of residual stress was considered in the delamination wear mechanism. Residual stress may play an important role on fatigue crack propagation. Thouless [68] investigated steady edge cracking behavior by loading condition and location of crack from free surface. His study of the long and short crack illustrated correlations between maximum stress intensity factor of opening and shearing motions as a function of depth and length of crack from free surface, and bucking instability determined by edge spalling. Larsson and Carlsson [69] demonstrated the discrepancy between finite element method and elastic solution. They found that the elastic stress field near crack-tip requires the secondary terms in analytical approaches of modified boundary layer problem. Consequently, stress field near crack tip can be determined by superposing the most dominant singular term and other higher orders of non-singular terms. Williams and Ewing [70] also analyzed inclined crack with applied uniaxial stress. From their empirical study they concluded the significance of T-stress by in-plane stress. Cotterell [71] has characterized the directionality of crack propagation with respect to T-stress. Although the onset of fracture mostly depends on the leading term, he proposed that T-stress determines the direction of crack propagation. Therefore influence of the secondary stress term on delaminating behavior under cyclic sliding contact must be included in wear mechanism. Experimental study of cobalt-based implant alloy from Mitchell and Shrotriya [62] illustrated the significant influence of residual stress on subsurface fracture mechanism by measuring wear rate. They utilized AFM probe to simulate sliding contact of single asperity and applied well characterized pre-stresses in compression and tension by using four-point bending frame. The results indicated high dependence of pre-stress on material surface wear by sliding contact. They postulated that oxide layer fracture and reformation process varies in the presence of residual tension and

compression. However the consistent wear trend was found in the identical wear experiment with copper specimen [72]. Since the soft cupric oxide is not passivation layer and cannot protect the sub-layer of copper from contact damage [73], this copper wear experiment depicts that the repeating fracture and repassivation process of surface layer is not a unique mechanism of sliding wear under residual stress state.

In the present work the influence of residual stress on subsurface fracture during sliding contact was investigated. The analytical model was developed to investigate cyclic stress intensity factors (ΔK) of pre-existing crack due to a single asperity contact with far-field stresses parallel to crack surface. Regardless of innumerable efforts on tribological and fracture mechanics studies of surface damage, there is no standard method to characterize surface fracture and wear. This analytical and numerical inspection of fatigue crack growth would provide a guideline to identify wear mechanism.

Mechanics Model of Delaminating Crack

Delamination model by consideration of fatigue crack growth

The motivation of the present study is to understand the microscopic fretting damage of metallic materials under the combined action of contact loading and residual stresses in the solid. Previous nano-indentation investigation [74] and molecular dynamics simulations [75] have showed that the nano-hardness of the material is not altered due to residual stresses. The above observation leads one to conclude that residual stresses might not affect the wear behavior of materials. However, earlier fretting experiments on CoCrMo specimen by Mitchell and Shrotriya [62] showed that the residual stress dependence of the fretting damage.

They presented increases in wear rate with compressive residual stress while a reverse trend of decreased wear rates was observed when the residual stresses were tensile in nature. Residual stress might affect the rate of oxide layer formation but similar observations of the effect of the residual stresses on fretting wear of copper specimen have been observed. Since the cupric layer is not stiff enough to protect the material surface from sliding contact, the wear process is not only due to oxide layer instability of fracture and reformation.

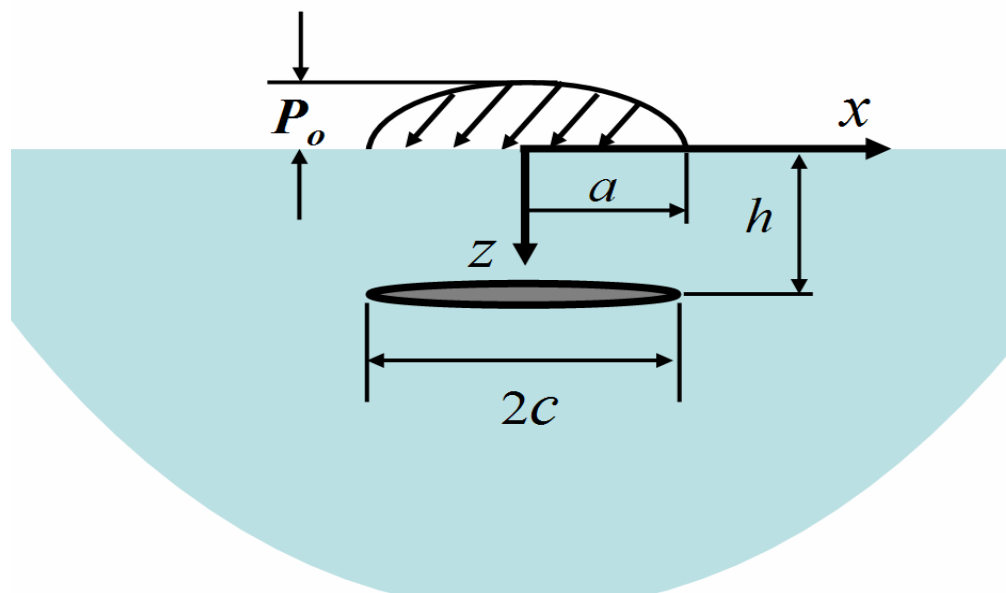


Figure 5- 1. A continuum body subjected to combined parabolic and tangential contact with pre-existing crack at subsurface, where P_o is maximum contact pressure, h and $2c$ are depth of crack location and half length of subsurface crack, respectively.

We followed the delamination wear theory as proposed by Fleming and Suh [65] to correlate our experiments. A continuum body subjected to sliding contact was considered to have pre-existing parallel crack of initial length, $2c$ at a depth of h below the surface (see Figure 5-1). The contact problem was investigated by non-confirming elastic contact solution by Johnson [76]. The surface of a perfectly smooth, plane strain semi-infinite and isotropic elastic medium is in contact with a rigid cylindrical body.

The contact size was assumed to be much smaller than the radius of curvature of rigid indenter to satisfy the linear elasticity. The contact loading comprises of both the normal compressive and tangential loads as seen in Figure 5-1. The tangential load occurs due to friction between the surface and the rigid indenter. The normal traction, P was approximated to parabolic distribution to satisfy uniform normal displacement condition. In order for consistent frictional traction, Q with macroscopic contact is to be proportional to normal traction following Amonton's friction law. Since microscopic friction force is not strongly dependent on normal load when the normal compressive traction is below the critical load level, however, it is possible to approximate uniform tangential traction over the contact area determined as $Q = \mu \pi P_o / 4$, where μ is friction coefficient [77].

Stress field by frictional contact of parabolic tangential and uniform tangential tractions were approximated by Johnson's cylinder sliding model based on McEwen's method[76, 78]. Maximum principal stress fields were normalized by the maximum normal traction, P_o and the coordinates of x and z were also non-dimensionalized by half-contact area, a , as presented in Figure 5-2. The maximum principal stress distribution above illustrated compression in most of the region by parabolic normal load, while there is region behind the tangential load that senses a tensile principal stresses. The subsurface crack will tend to grow when the crack tip is loaded by the tensile stresses. During repetitive sliding motion of sliding the maximum value of cyclic stress intensity factor (ΔK) and location would determine wear rate.

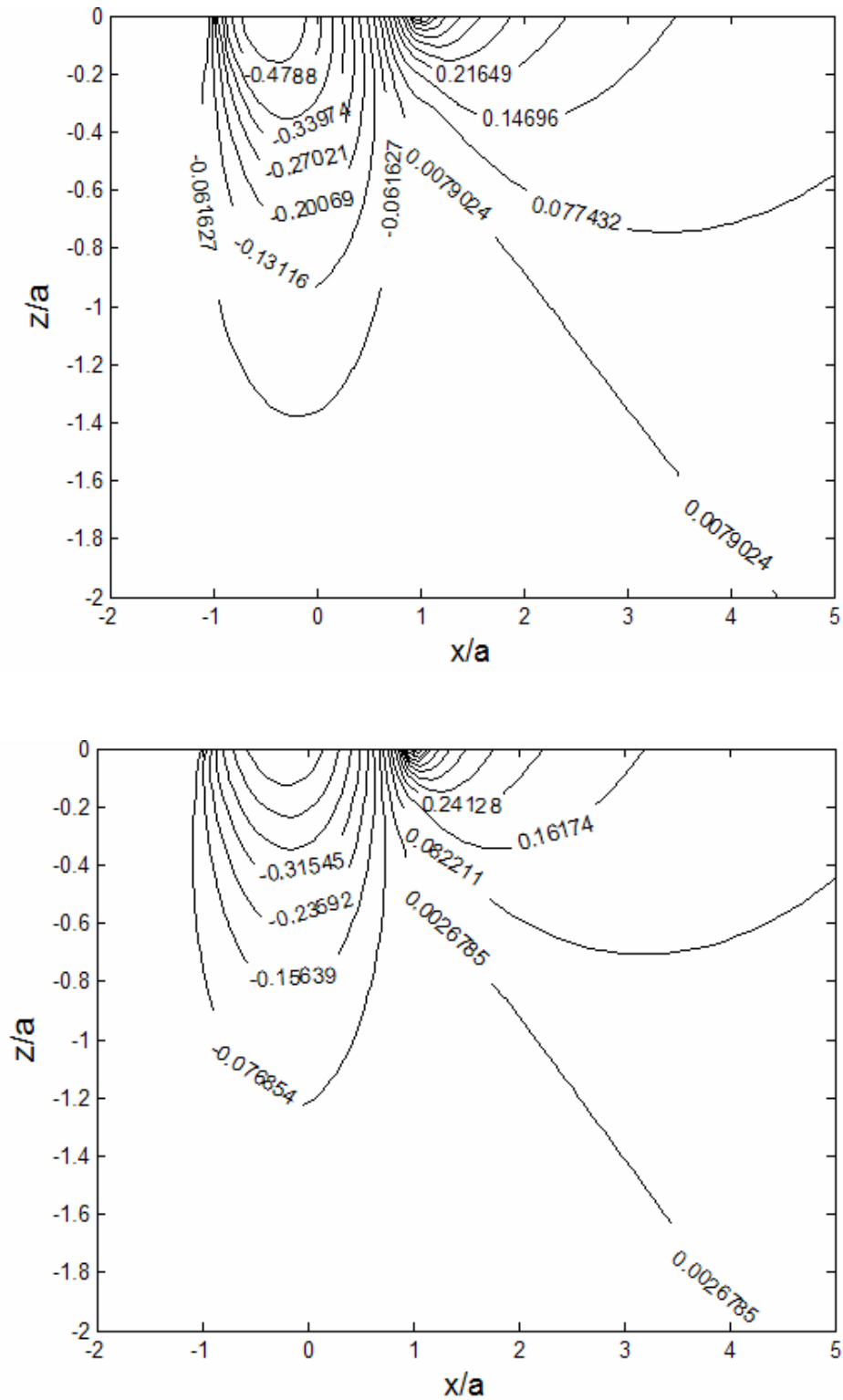


Figure 5- 2. Maximum principal stress distribution solved by Johnson's elastic contact solution under combined loading of parabolic normal and parabolic tangential contact (top) and parabolic normal and uniform tangential contact (bottom) with $\mu = 0.5$.

Following Fleming and Suh [65] we calculated the mixed-mode stress intensity factors due to the presence of a subsurface crack subjected to a Johnson's elastic inclined contact. Their method provides lower bound (through-crack in infinite material) and upper bound (edge-crack in semi-infinite material) of stress intensity factors for crack growth.

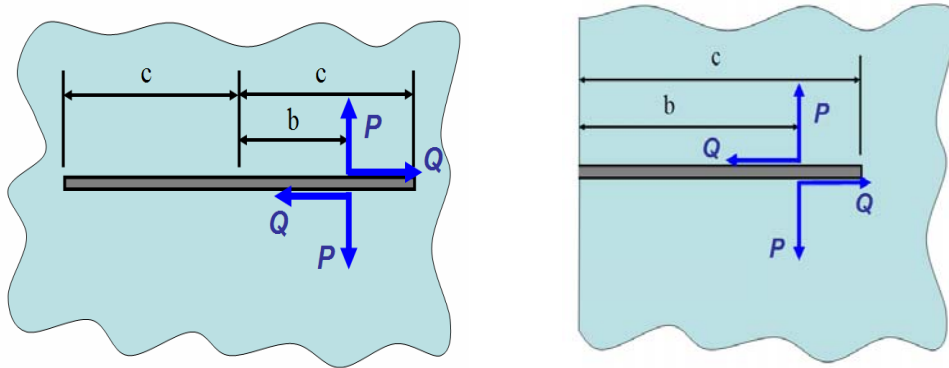


Figure 5- 3. Geometrical presentation of through crack and edge crack with loads.

The applied stress intensity factors were approximated by integration over the crack surface as shown in Figure 5-3 by utilizing equations below;

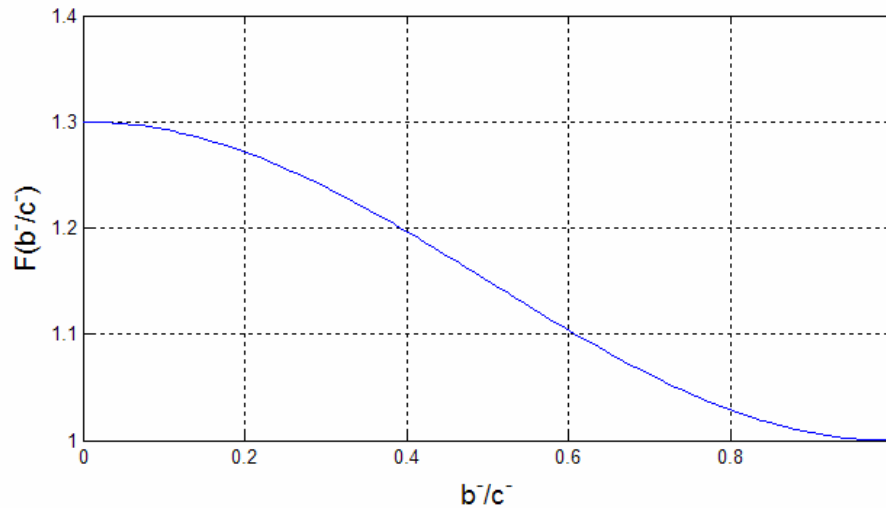
$$d\bar{k}_I^{+c} = \frac{1}{2\sqrt{c}\pi} \left[\sqrt{\frac{c+b}{c-b}} (\bar{\sigma}_z d\bar{x}) - \left(\frac{k-1}{k+1} \right) (\bar{\tau}_{xz} d\bar{x}) \right] \quad (5-1-1)$$

$$d\bar{k}_{II}^{+c} = \frac{1}{2\sqrt{c}\pi} \left[-\sqrt{\frac{c+b}{c-b}} (\bar{\tau}_{xz} d\bar{x}) - \left(\frac{k-1}{k+1} \right) (\bar{\sigma}_z d\bar{x}) \right] \quad (5-1-2)$$

$$d\bar{k}_I = \frac{2}{\sqrt{c}\pi} \left[\frac{F(\bar{b}/\bar{c})}{\sqrt{1-(\bar{b}/\bar{c})^2}} (\bar{\sigma}_z d\bar{x}) \right] \quad (5-2-1)$$

$$d\bar{k}_{II} = \frac{2}{\sqrt{c}\pi} \left[\frac{F(\bar{b}/\bar{c})}{\sqrt{1-(\bar{b}/\bar{c})^2}} (\bar{\tau}_{xz} d\bar{x}) \right] \quad (5-2-2)$$

, where the $F(\bar{b}/\bar{c})$ is defined as a function of ratio between generalized position of local load (\bar{b}) and length of crack (\bar{c}), \bar{b}/\bar{c} .



By numerical integration of equation (5-1) the maximum cyclic stress intensity factor (ΔK) of lower bound was estimated and influence of tangential tractions on wear rate is qualitatively compared in Figure 5-4. The contours of cyclic stress intensity factors of mode *I* and *II* (ΔK_I and ΔK_{II}) are presented with different tangential tractions i.e. parabolic tangential and uniform tangential tractions, respectively. The maximum ΔK_I and ΔK_{II} with uniform tangential traction is greater than with parabolic tangential traction while the depth of maximum ΔK_I and ΔK_{II} indicates lower wear depth with uniform tangential traction. Therefore the fatigue crack growth rate with parabolic tangential traction would be lower but the wear depth with parabolic tangential traction would be greater than with uniform tangential traction.

Therefore the overall wear rate of the sliding contact with different tangential motion will be determined by combination of fatigue crack growth rate and depth.

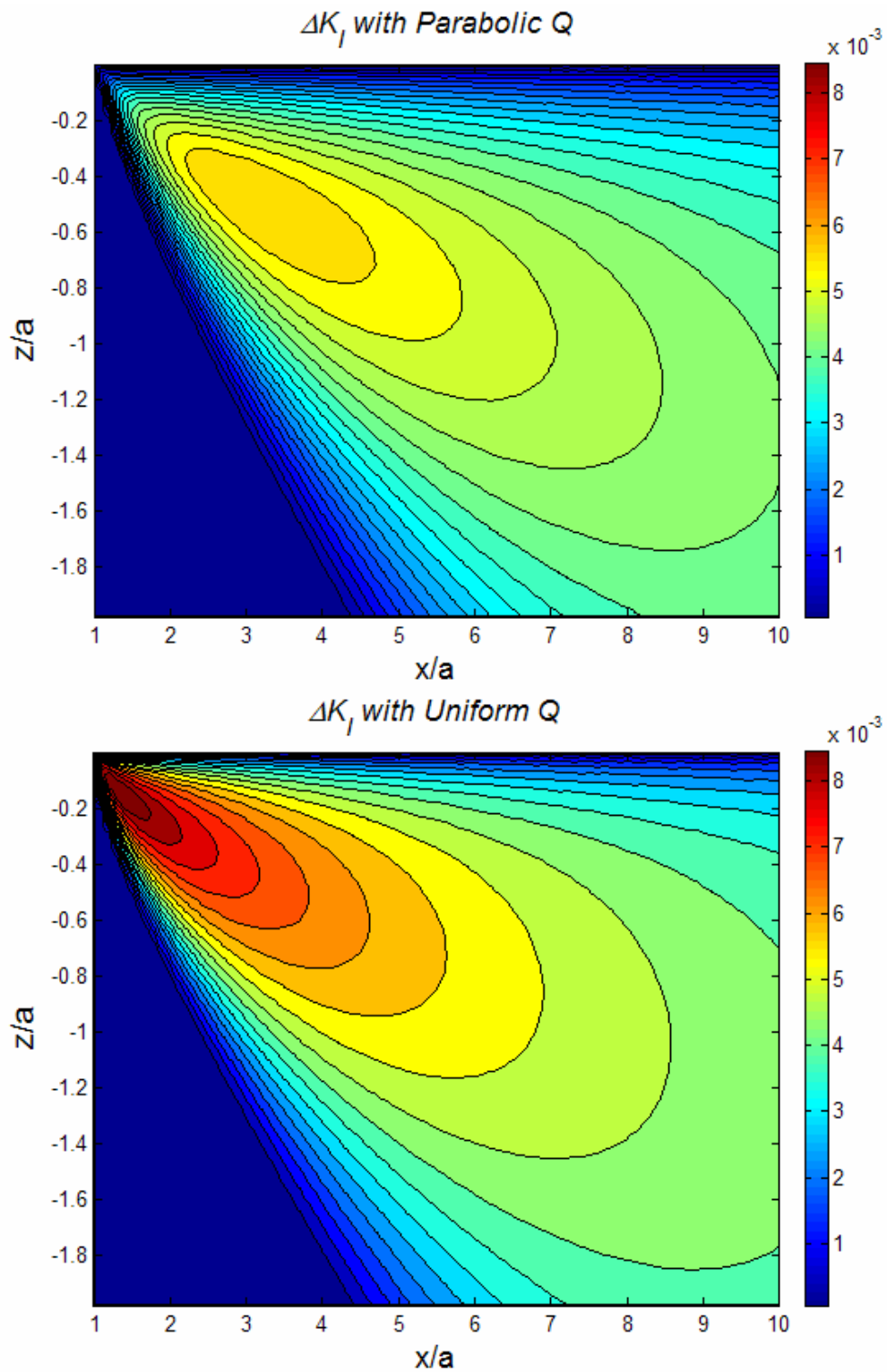


Figure 5- 4. Contour of ΔK_I on parallel crack due to combined contact of parabolic normal and parabolic tangential (top), and parabolic normal and uniform tangential (bottom) loadings

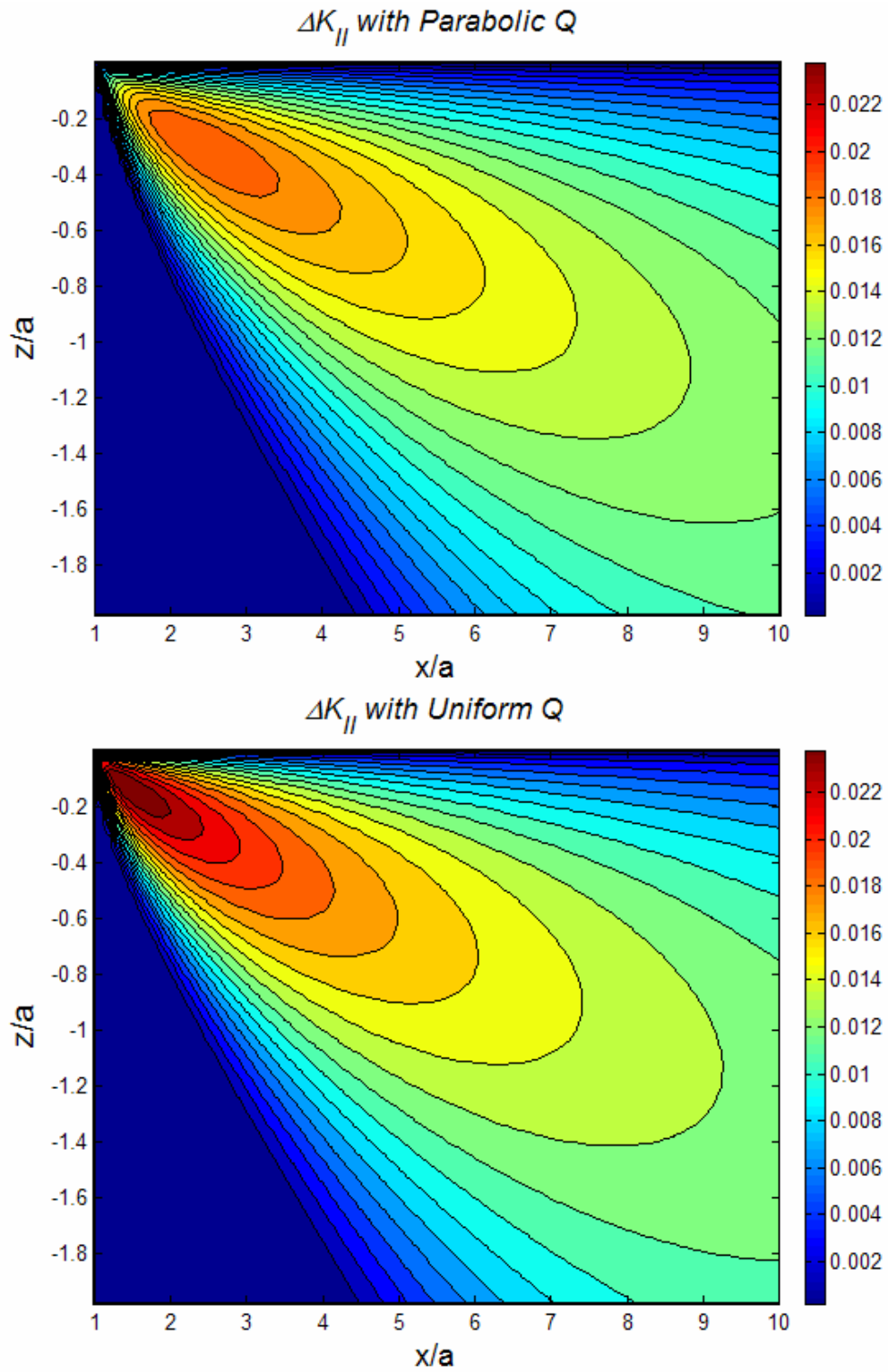


Figure 5- 5. Contour of ΔK_{II} on parallel crack due to combined contact of parabolic normal and parabolic tangential (top), and parabolic normal and uniform tangential (bottom) loadings

Effect of secondary in-plane stress

In the present study, we assume that the crack-tip field obeys the small scale yielding conditions and superposition of the stress intensity factors due to the contact load and residual stresses to be admissible. As mentioned earlier, the Fleming and Suh's [65] delamination wear theory didn't include the effect of secondary terms of stresses on crack growth and hence needs to be modified when the residual stress is loaded. Drory et al. [79] conducted experiments and analysis of decohesion of residually stressed thin films on semi-infinite substrates. Mixed-mode analysis by Suo and Hutchinson [80] have also analyzed decohesion due to residual stresses in thin films on substrates. In the present study the subsurface crack at a depth h can be treated as thin film on a substrate for the purpose of analysis. In our analysis the thin film and substrate are made of the same material (no mismatch in the elastic properties), thus simplifying the analytical expression of Drory et al. [79] and Suo & Hutchinson [80]. When a compressive residual stress is present the interfacial delamination experiences an elastic instability in the form of plate buckling of the thin film. The buckling of the delamination or subsurface crack drives crack growth. However, when the residual stress is tensile in nature the parallel crack is stretched and the crack face does not buckle thereby inhibiting crack growth. The resulting applied stress intensity factors due to the combination of the contact loads and residual stresses can be written as below based on the model schematically depicted in Figure 5-6.

$$\begin{Bmatrix} \Delta K_I(h) \\ \Delta K_{II}(h) \end{Bmatrix} = \int_c \frac{1}{\sqrt{c}} \begin{Bmatrix} \sigma_z(x, h) \\ \tau_{xz}(x, h) \end{Bmatrix} dx - \text{sign}(\sigma_\infty) \sigma_\infty \sqrt{\frac{h}{2}} \begin{Bmatrix} \cos \omega \\ \sin \omega \end{Bmatrix} \quad (5-3)$$

where $\omega = 52.07^\circ$ obtained by the Dundur's elastic mismatch parameters.

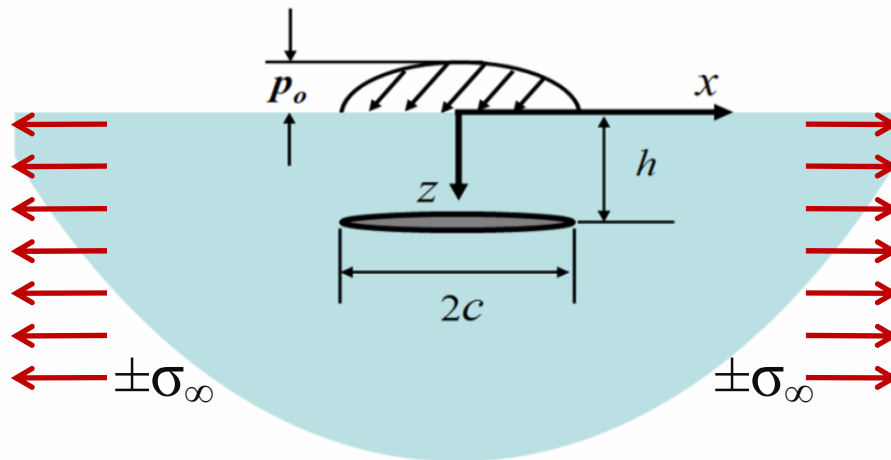
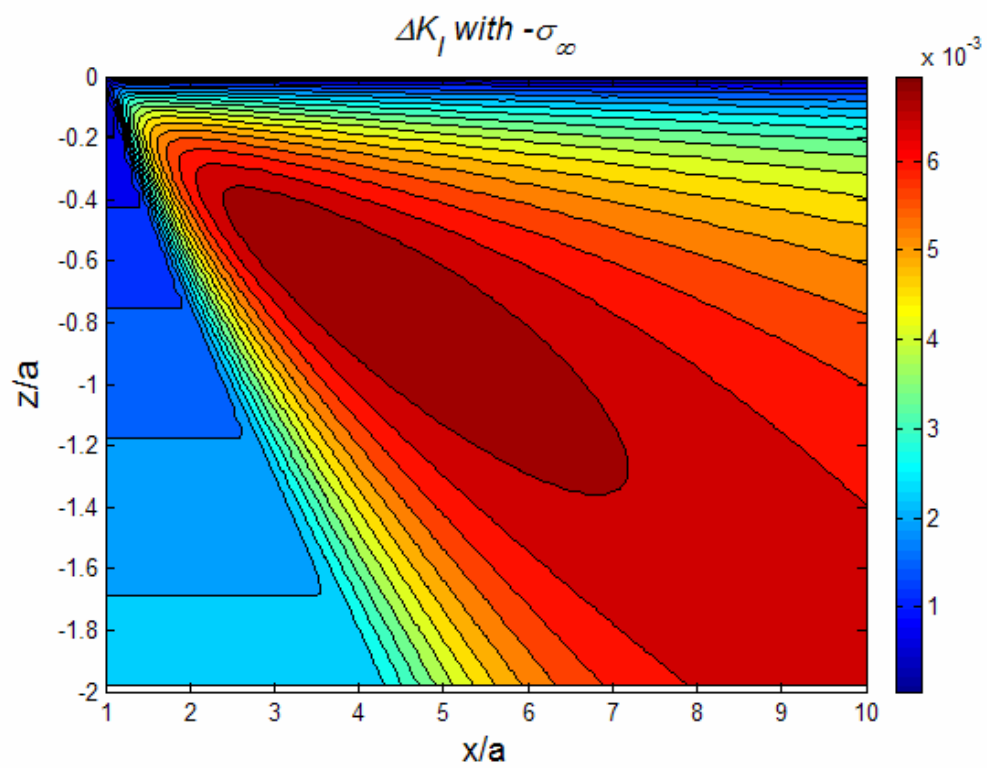
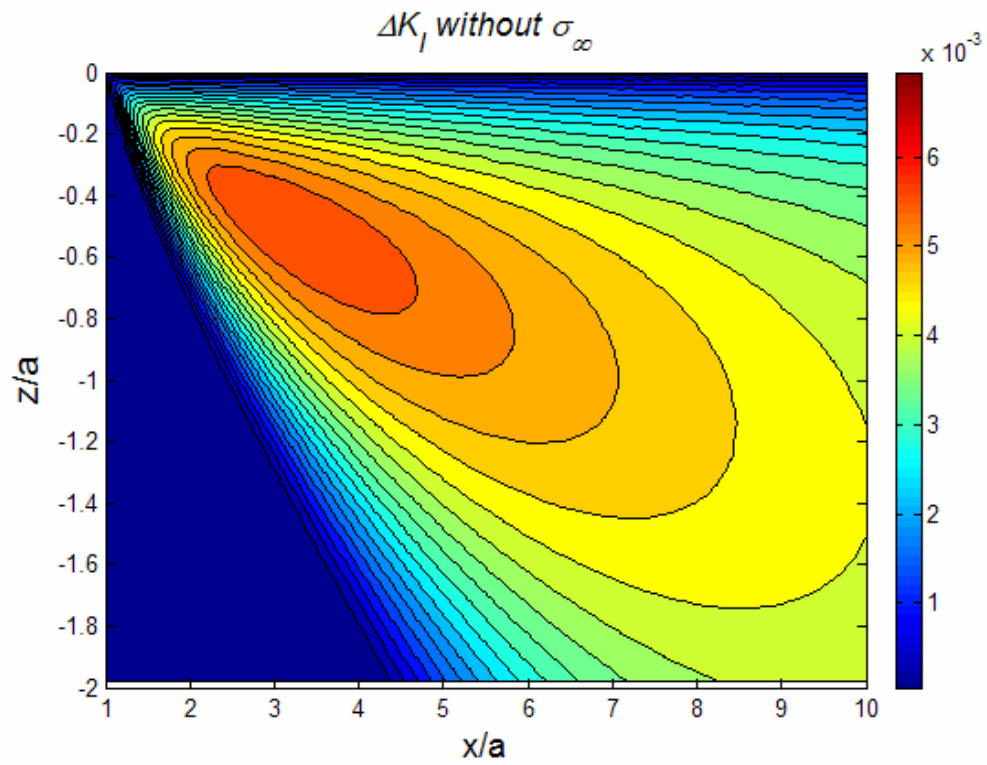


Figure 5- 6. Parallel crack model with normal traction and constant friction coefficient, $\mu = 0.5$ is subjected to in-plane compression $(-\sigma_\infty)$ and tension $(+\sigma_\infty)$

The cyclic stress intensity factors of mode *I* and *II* with in-plane residual stresses which are in elastic compression and tension chosen as 20% of the yield strength ($\sigma_\infty = \pm 0.2\sigma_y$) were computed from equation (3). Sliding contact was loaded in the form of parabolic normal with constant friction coefficient, $\mu = 0.5$. The stress intensity factors are amplified by a compressive residual stress due to the buckling of the surface layer above parallel cracks while the effective stress intensity factor decreases when the residual stresses are tensile in nature as observed in surface layer spalling model. The effective stress intensity factor can explain the linear increase in the fretting wear with compressive residual stress [50] and will be discussed in detail later.



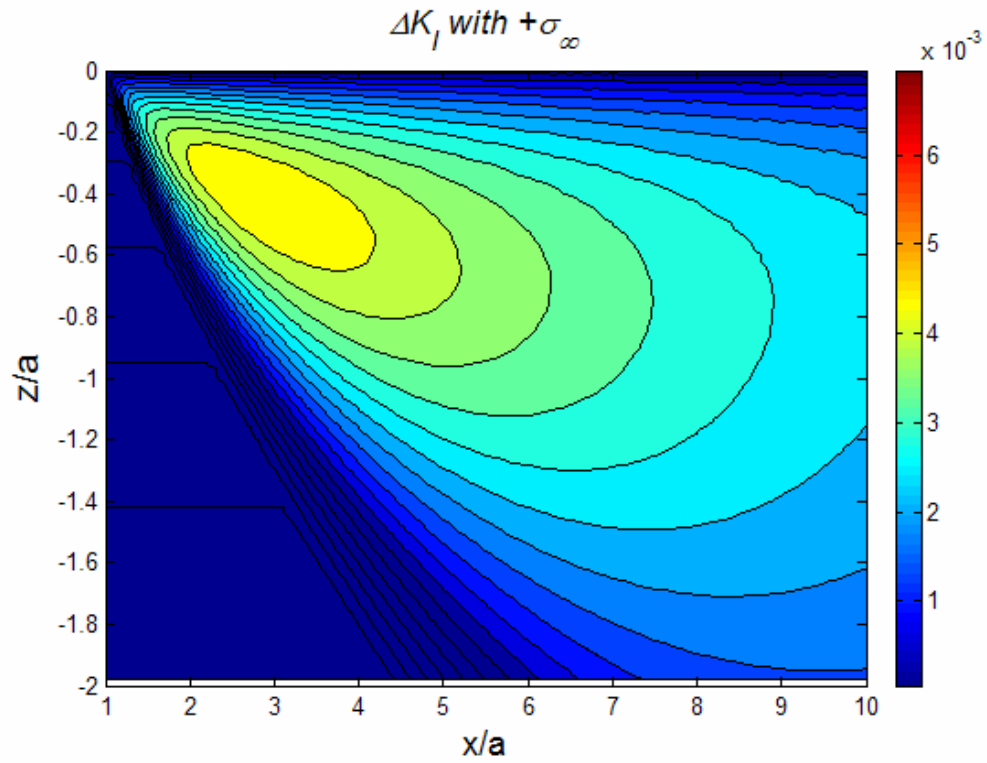
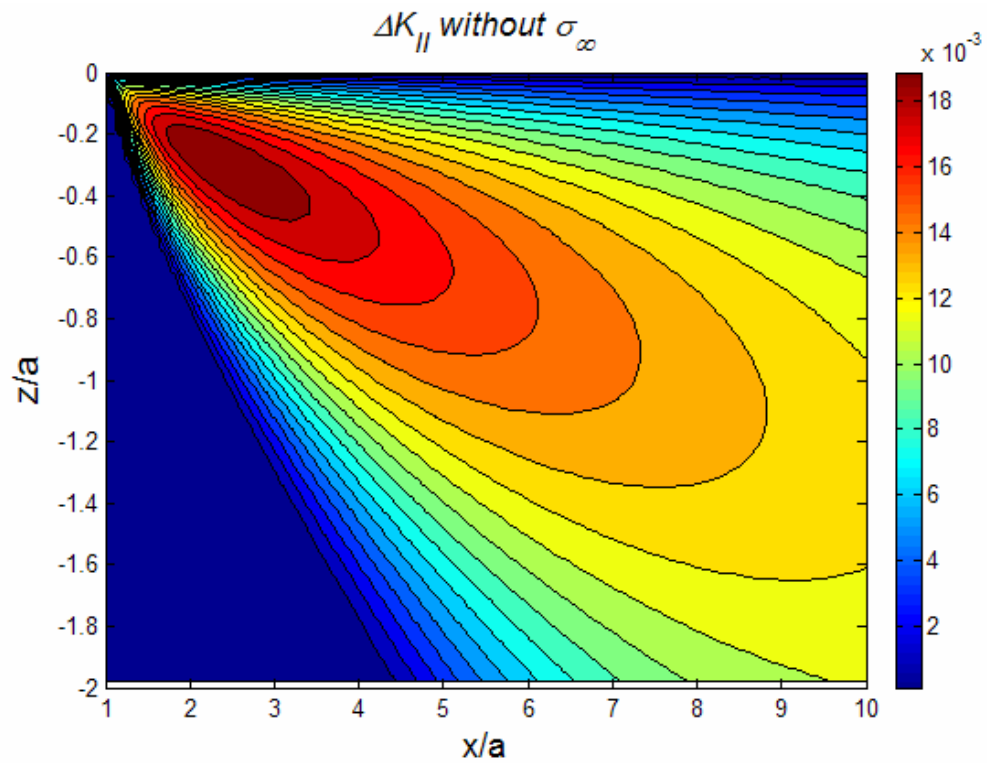


Figure 5- 7. Contour of stress intensity factor of mode I by parabolic friction without far-field stress (top), with far-field compression (middle) and with far-field tension (bottom)



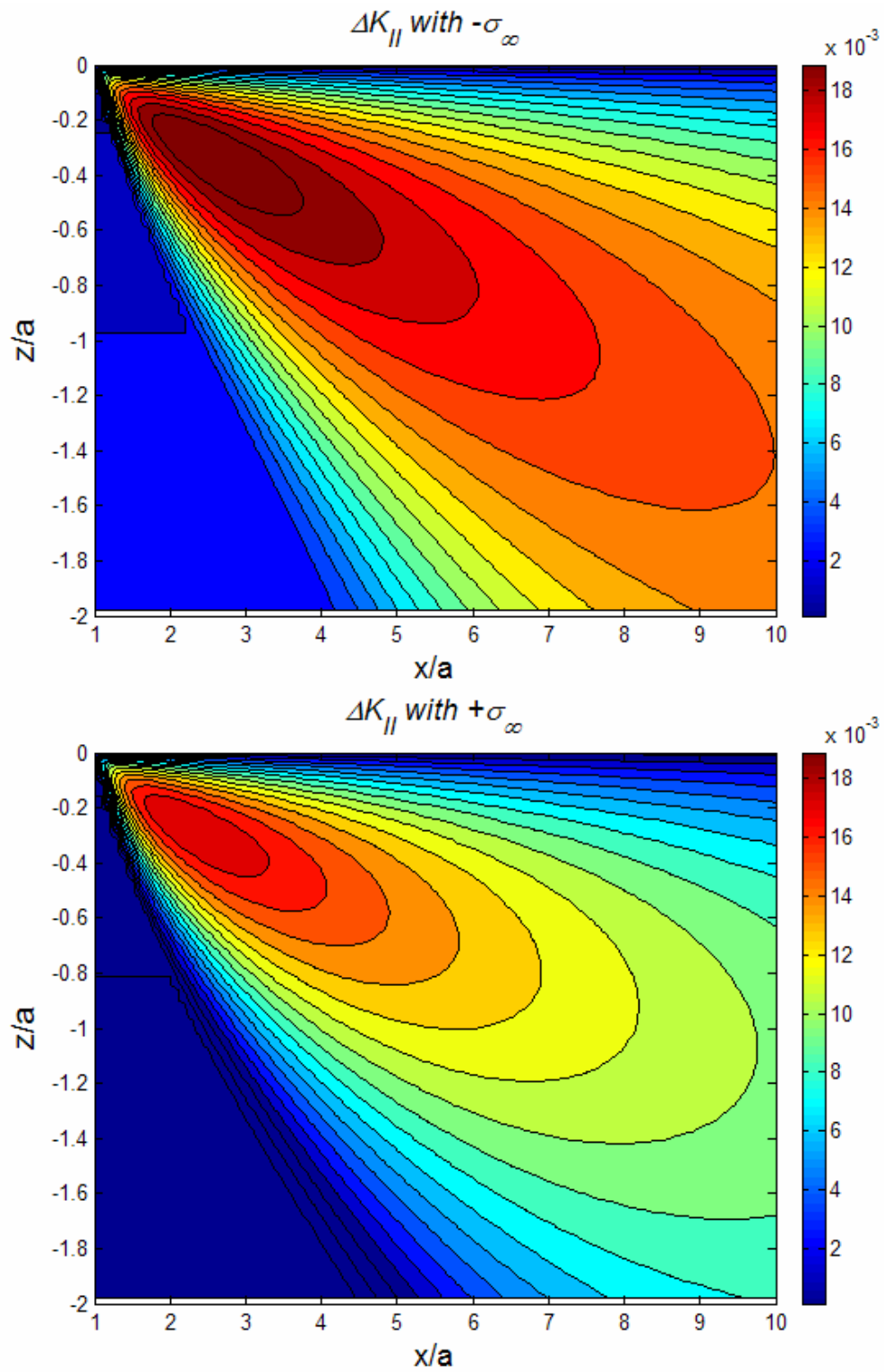


Figure 5- 8. Contour of stress intensity factor of mode II by parabolic friction without far-field stress (top), with far-field compression (middle) and with far-field tension (bottom)

Results and Discussion

The ductile material fracture under cyclically varying loadings has been investigated by introducing stress intensity factor changes. The repeating sliding contact induces alternating compression and tension in the general nature of fatigue due to fully reversed loadings on the body. As presented in the elastic fracture mechanics model of fatigue crack tip, it is postulated that the fatigue crack extension at each cycle of sliding according to fatigue crack growth law prescribed by Paris and Erdogan. The growth of parallel crack depends on varying stress field due to sliding contact. The resultant contact stress field is mostly elastic dominant while the plastic zone is constrained in the range of orders of contact size, unless the normal load is so severe and/or friction coefficient is so high that the contact leads to ploughing. Therefore the rate of crack growth can be characterized by inspection of K_I changes at the crack tips in the imposed elastic stress field.

Stress fields were approximated by Johnson's contact solution with two different combinations of contact loads, i.e. parabolic normal traction with parabolic tangential traction, and parabolic normal with constant tangential traction. In order to generalize the contact problem the stresses and lengths are normalized by maximum normal traction, P_o and half contact size, a , respectively. The established stress field was plotted in Figure 5-2 with different tangential contact conditions. The ΔK_I and ΔK_{II} of crack tip were assessed by numerical integration over the varying lengths of crack surface at the varying depths of crack locations. This result indicated that the crack locations of maximum ΔK_I and ΔK_{II} in the case of parabolic normal traction with constant tangential traction are closer to free surface while the magnitude of ΔK_I and ΔK_{II} in the case of uniform tangential traction is

greater than in parabolic tangential traction. The values of ΔK_I and ΔK_{II} are plotted as a function of subsurface crack location in Figure 5-9 and Figure 5-10. Since the cracks may propagate at the location of maximum ΔK_I and ΔK_{II} , it implies that the constant tangential traction creates smaller size of wear depth while the driving force of crack-tip propagation due to constant tangential traction leads to faster growth.

Experimental results of wear rate of ConCrMo and copper with residual stress have been illustrated linear trend of suppressed wear rate when subjected to tensile in-plane stress and reversed trend when subjected to compressive in-plane stress [62, 72]. Similarly, ΔK_I and ΔK_{II} stimulated by stress state of frictional contact and secondary stress field in tension or compression presented significant influence of residual stress condition as shown in Figure 5-7 and Figure 5-8. Greater ΔK_I and ΔK_{II} were found with compressive in-plane stress while lower ΔK_I and ΔK_{II} were shown with tensile in-plane stress. Plots of maximum ΔK_I and ΔK_{II} as a function of depth are plotted in Figure 5-11 for three different values of residual stress state. The results indicate that maximum value of ΔK_I and ΔK_{II} occurs for compressive stress state. The location of maximum ΔK_I becomes deeper as the sign of residual stress changes

The maximum ΔK_I values were estimated with varying pre-stress from compressive to tensile. As shown in Figure 5-12 the linear dependence of ΔK_I on residual stress indicates greater crack growth rate under compressive residual stress during sliding contact as discussed by experimentally measured wear rate from Mitchell and Shrotriya [62].

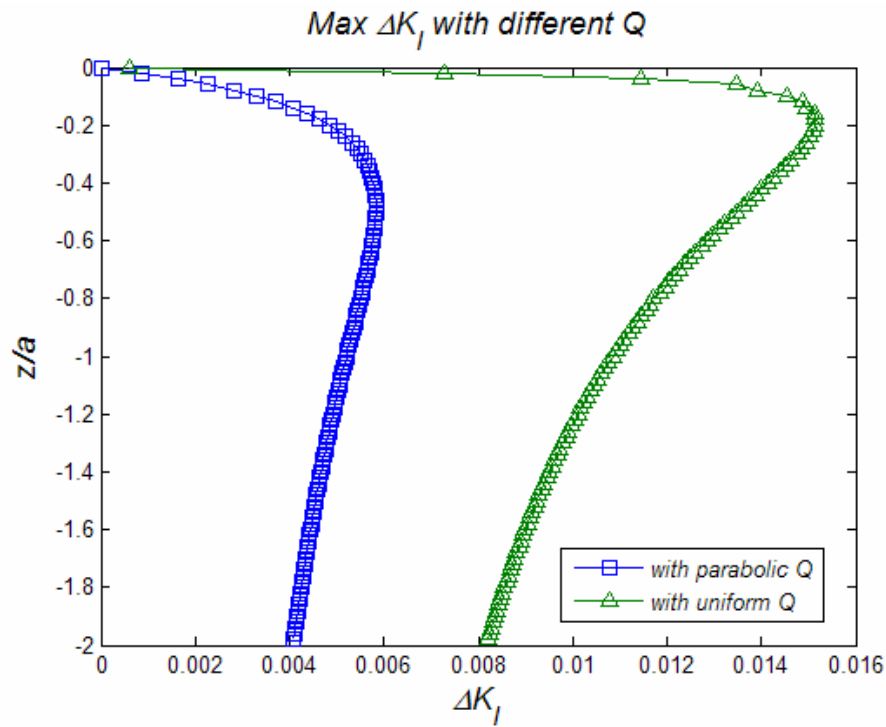


Figure 5- 9. Maximum ΔK_I distribution along the depth of the contacting medium with different tangential tractions.

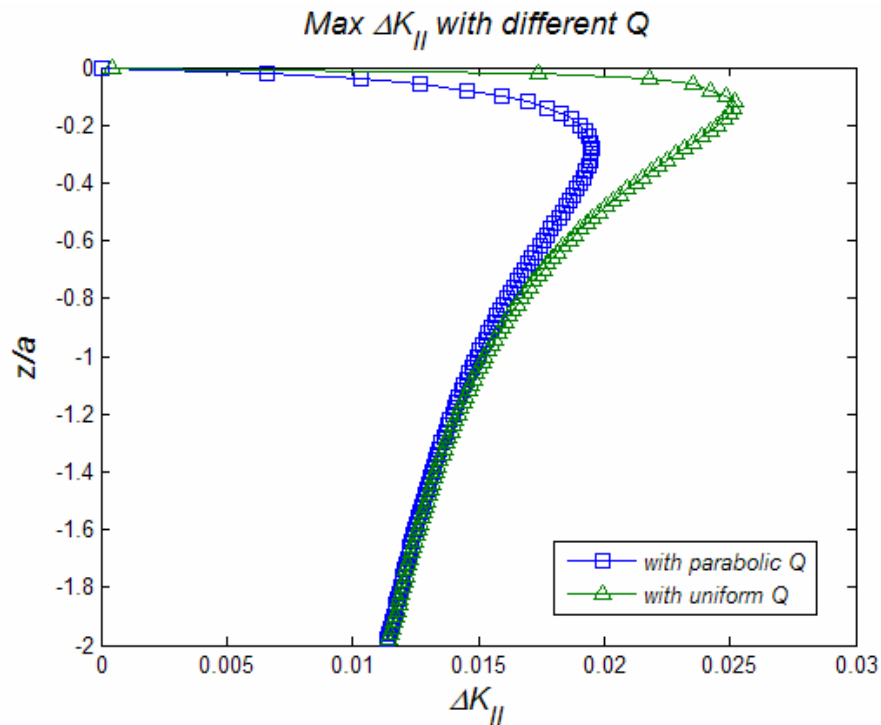


Figure 5- 10. Maximum ΔK_{II} distribution along the depth of the contacting medium with different tangential tractions.

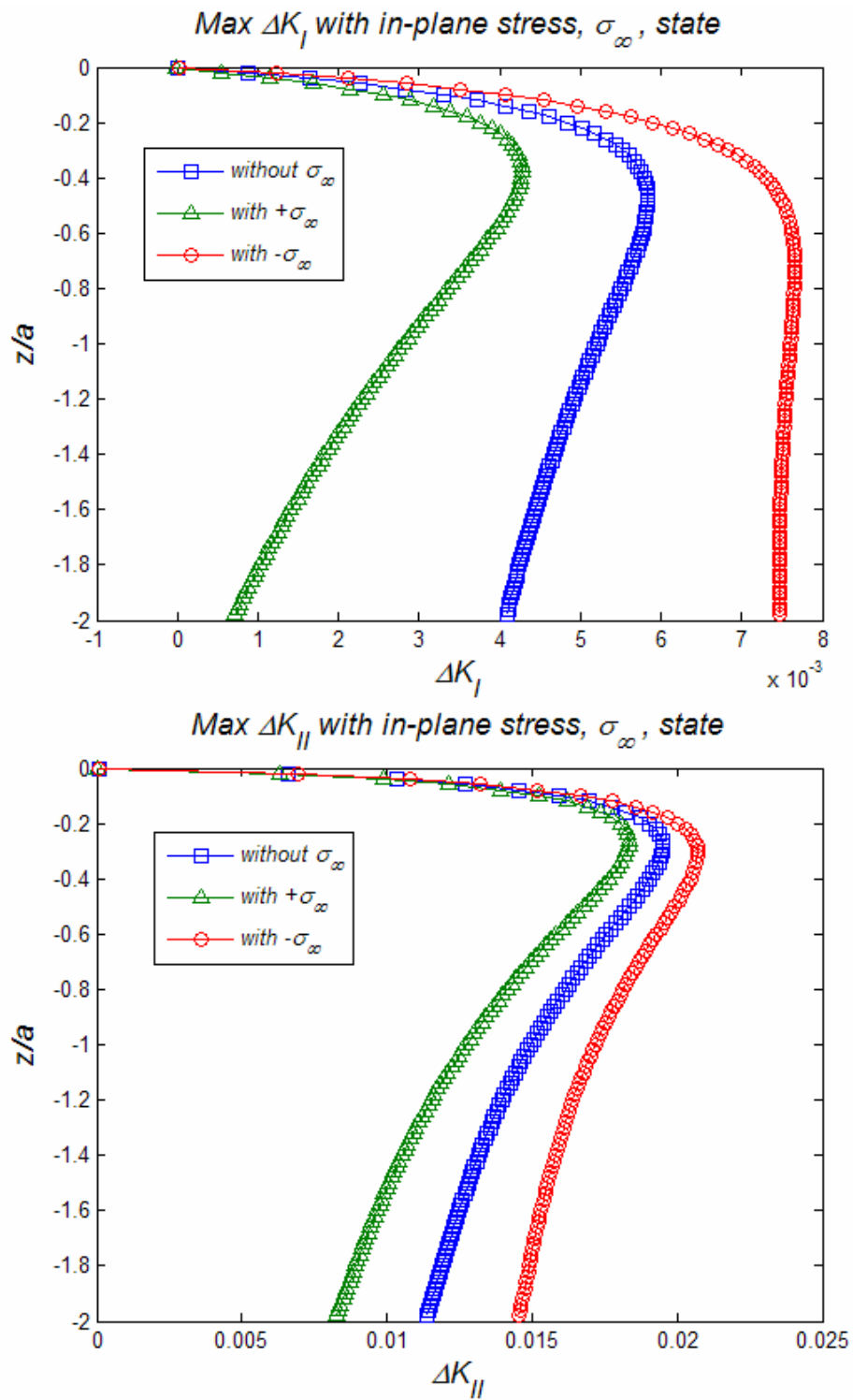


Figure 5- 11. Maximum ΔK_I (top) and ΔK_{II} (bottom) distribution along the depth of the contacting medium indicates higher fatigue crack growth rate and wear depth.

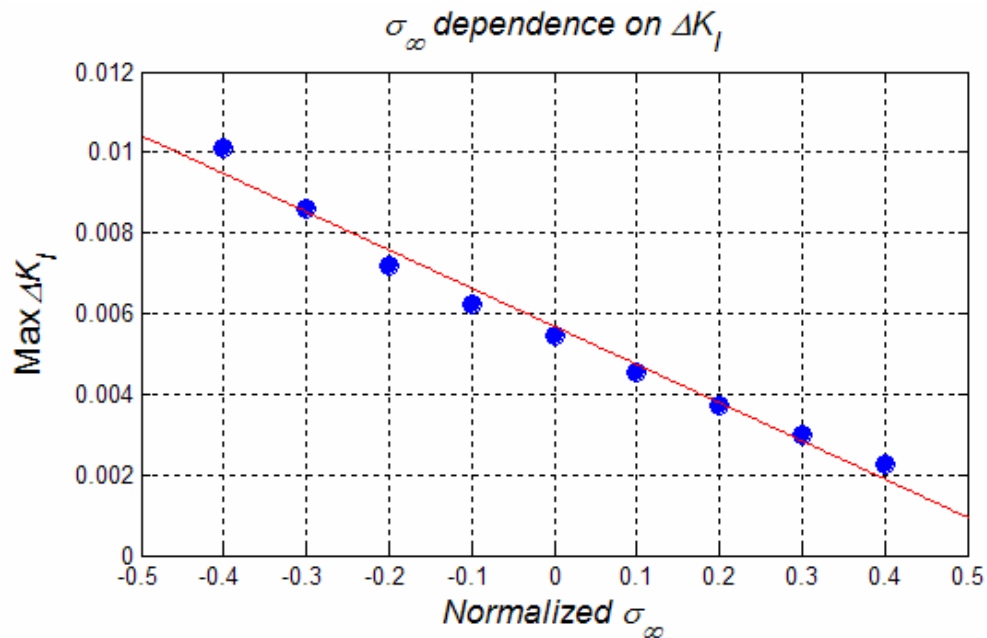


Figure 5- 12. Linear trend of maximum ΔK_I with in-plane stresses implies residual stress dependence of delamination wear

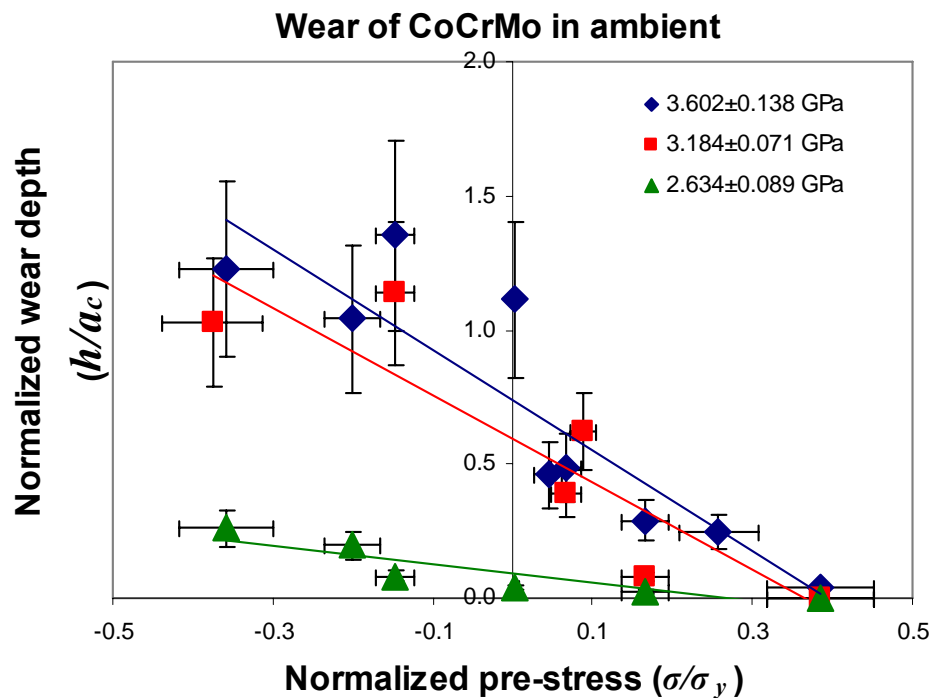


Figure 5- 13. Linear dependence of wear depth during cyclic sliding contact of single asperity with pre-stress loaded on the contacting CoCrMo sample surface where h is measured wear depth and a_c is half contact area obtained by Hertzian contact model.

The consistent experimental result of the linear dependence of fatigue stress intensity factor (ΔK_I) with surface stress state was found in the AFM-based fretting damage experiment in ambient illustrated linear correlations between surface stress and wear depth due to cyclic sliding contact of single asperity as shown by Mitchell and Shrotriya in Figure 5-13 [62].

Conclusion

Subsurface fracture model by cyclic sliding contact has been studied by inspecting stress intensity factors. If crack growth rate follows Paris law the cyclic sliding motion propagates subsurface crack by alternating tension and compression leading to delamination fracture of the surface layer. Stress state and effective crack length determine the stress intensity factor and the location of maximum stress intensity factor and thus wear rate can be qualitatively approximated by observation of cyclic stress intensity factor. The influence of combined secondary in-plane stress with sliding contact-induced stress is significant to determine wear rate since compressive stress of parallel crack tends to buckle the crack plane and opens the crack-tip while tensile stress tends to close crack-tip. Accordingly, the cyclic transformation of compression and tension due to fretting motion may propagate subsurface crack and imposed residual compression drives buckling of crack surface leading to higher wear rate while residual tension suppresses wear rate.

CHAPTER 6. ELECTROCHEMICAL DISSOLUTION OF BIOMEDICAL GRADE Ti6Al4V: INFLUENCE OF RESIDUAL STRESS AND ENVIRONMENT

Abstract

Stress dependent electrochemical dissolution is identified as one of the key mechanisms governing surface degradation in fretting and crevice corrosion of biomedical implants. In the current study, material removal on a stressed surface of Ti6Al4V subjected to single asperity contact is investigated to identify the influence of contact load, residual stress and environment on wear damage. A range of known stress levels are applied to the specimen while its surface is mechanically stimulated in different non-reactive to oxidizing aqueous environments. Evolution of surface degradation is monitored, and its mechanism is elucidated. Implications to life prediction of orthopedic implants are discussed.

Keywords:

Surface, Residual stress, Electrochemical dissolution

Introduction

Fretting corrosion of modular implant material is an insidious problem and may limit the service life of the implants. Repeated contact at modular interface of metallic implants in the corrosive physiological environment results in formation of particulate and soluble debris that can migrate locally or systemically and may induce a cascade of inflammatory events that may ultimately result in bone loss by osteolysis and subsequent implant failure. Fretting corrosion results in metal degradation due to the simultaneous action of mechanical loading and electrochemical oxidation. The two mechanisms do not proceed separately, but depend on each other in a complex way and are influenced by such factors as (a) the elastic and plastic properties of the surfaces (b) contact pressure (c) roughness of the contacting surfaces (d) corrosive environment. The major questions that still exist are: 1) what is the mechanism for onset of material damage at the interface? 2) How can the onset of failure in the interfaces for a given set of materials and interface conditions be predicted? 3) How do the material properties, implant design and surface roughnesses affect these mechanisms and predictions? This lack of understanding severely limits the designers and manufacturers in their efforts to optimize current surface finishing operations in order to produce more durable and reliable total joint replacements.

Our long-term goal is to utilize understanding of mechanisms governing fretting corrosion induced surface damage for design of total joint replacements with enhanced durability and reliability. The objective of this project is to identify the mechanisms governing initiation of surface damage on implants manufactured from titanium alloys. The central hypothesis for this work is that during mechanical load assisted dissolution of implant

surfaces, applied contact loads and surface stress state determine the mechanism governing delamination, dissolution and repassivation of the native oxide layers and underlying material. The experimental analysis tries to identify the mechanisms governing onset of damage on implant surfaces i.e. to identify the influence of contact-induced stresses, the impact of bone and surface debris on fretting corrosion.

We have completed the electrochemical and single asperity surface damage characterization of polished titanium (Ti6Al4V) and cobalt-chromium (CoCrMo) samples. Atomic force microscope (AFM) based experiment to determine the rate of surface damage as a function of environment, contact loads and surface stress state. Ti6Al4V specimens were exposed to four different environment: ambient, phosphate buffered saline (pH 7.4), phosphate buffered saline (pH 4.1), phosphate buffered saline (pH 2.0), CaCl₂ solution (pH 2.0). Since aggressive pitting damage of CoCrMo was observed in the lower pH level solution, CoCrMo specimens were tested only in ambient, phosphate buffered saline (pH 7.4), phosphate buffered saline (pH 4.1), and CaCl₂ solution (pH 4.1).

Experimental set up and procedure

The four-point bending frame is designed to apply varying levels of stress states throughout the sample as illustrated in Figure 6-1. The sample along with four rollers are placed in-between the c-clamp and the extrusion on the base. The rollers, which are modified pin gages (Meyer's Gage Company, South Windsor, CT), force the c-clamp to open against the base. The amount of force is measured by monitoring the free end deflection of the clamp with a capacitance gage (Capacitec, Myer, MA). This deflection has been calibrated by a dead weight method and magnitude of applied force has been determined.

The force applied to the clamp is distributed over the four rollers creating a load control setup. The four-point bending configuration ensures that mid-span of the sample between the inner rollers will experience a range of stresses from compressive stresses. The stress state of any location of the sample surface may be determined from: the load on the rollers, sample dimensions and distance of the location from the edge.

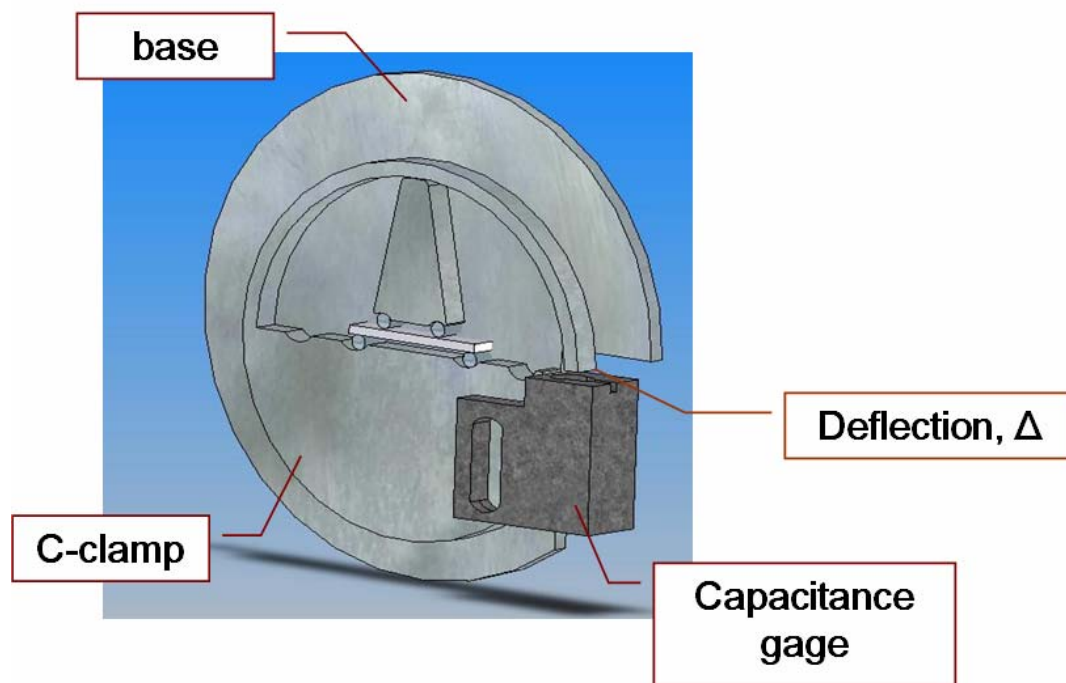


Figure 6- 1. C-clamp design with capacitance gage, utilizing varying size of rollers different bending force, which can be measured by deflection of free end of clamp arm, can be loaded on the rectangular specimen.

A Dimension 3100 atomic force microscope (AFM) with Nanoscope IV controller (VEECO Instruments, Woodbury, NY) was utilized for this experiment. A fluid cell and polymer protective skirt were employed in all testing to protect the piezoelectric scanner on the AFM. Silicon nitride (Si_3N_4) cantilevers with a reflective gold backside coating (DNP-S VEECO Instruments, Woodbury, NY) were used in the present study. Cantilever spring

constant was experimentally determined prior to each study to ensure application of accurate contact loads. Each cantilever's spring constant was determined by monitoring the deflection of the cantilever against a hard substrate (Sapphire) as well as a reference cantilever with known spring constant (VEECO Instruments, Woodbury, NY). In addition, the radius of curvature of the probe was characterized before and after each set of experiments by a commercially available characterizer (TGT01 Micromasch, Wilsonville, OR) in order to determine the probe wear during mechanical stimulation.

Surface damage response of sample was investigated at five different contact forces and five different pre-stress states. The metallic implant materials were loaded into the four-point bending frame and free end deflection of the c-clamp was monitored with the capacitance gage as schematically presented in Figure 6-2.

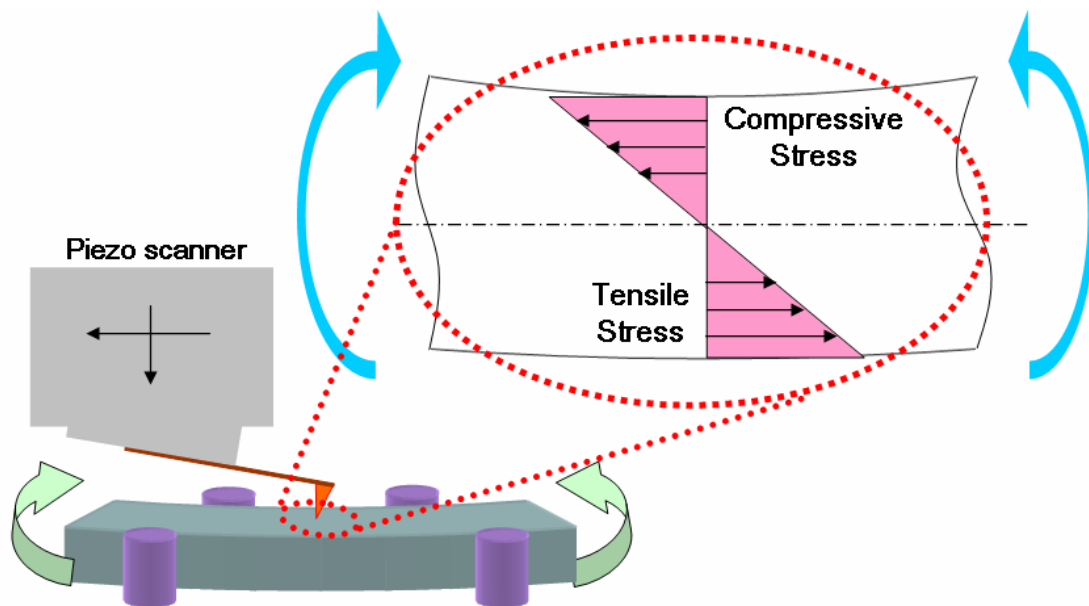


Figure 6- 2. AFM-based fretting contact experimental on stressed rectangular specimen by 4-point bending set up using c-clamp.

An optical camera and step-motor driving motion control were utilized to identify locations that correspond to desired stress states across the specimen surface. The loaded sample was

then placed underneath the AFM and all the tests were preformed for each environment, i.e. ambient and aqueous environment of varying pH levels. In order to clarify the influence of corrosion, in the first step, the wear experiment was performed in ambient. As for the second step a corrosive physiological environment was simulated by using phosphate buffered saline solution (PBS) (Invitrogen, Carlsbad, CA) was augmented with HCl (Fisher Scientific, Fairlawn, NJ) to a desired pH (determined by a pH meter). Also calcium chloride solution was used with HCl solution to pertain comparable chemical condition with PBS. For physiological environment, three values of pH were chosen to simulate the crevice environment. A pH value of 7.4 was used to simulate the pH in the human body, while lower values of 4 and 2 simulate the act of differential aeration within a crevice.

For each test, an initial $5\ \mu\text{m} \times 5\ \mu\text{m}$ AFM scan was recorded at a contact force of 1-2 nN. Mechanical stimulation was then preformed at the center of the $5\ \mu\text{m} \times 5\ \mu\text{m}$ scan on an area of $2\ \mu\text{m}$ by $500\ \text{nm}$. The tip was rastered across this area at 5 Hz for 15 minutes at the desired contact force. Under these conditions each scan line would be covered approximately 70 times along the slow scan axis ($500\ \text{nm}$ dimension). After 15 minutes the scanning parameters were reset to a contact force of 1-2 nN and the final image of $5\ \mu\text{m} \times 5\ \mu\text{m}$ area was recorded. Five mechanical stimulation tests at contact loads of 60nN, 45nN, 30nN, 15nN and 5nN were conducted and the AFM probe wear was also monitored to determine average contact stress for a given surface stress state.

Surface damage was estimated from material removed from $2\ \mu\text{m}$ by $500\ \text{nm}$ area during the test. The initial surface of the sample was initially polished to a mirror finish but localized surface imperfections such as scratches or adhesive tear out pits from polishing etc, could not be completely eliminated. In order to minimize the effects of initial surface

imperfections on the calculation of surface damage, the initial and final $5\mu\text{m} \times 5\mu\text{m}$ images obtained for each test were registered and subtracted to determine the material removal. Average depth of stimulated area was determined from the subtracted images to estimate volume of removed material.

It is necessary to compare material removal based on average contact stress rather than the load since the initial probe radius of curvature varies slightly from one probe to another. Hertzian contact analysis is used to determine the average contact stress based on values of contact load and probe radius. The material properties of Ti6Al4V, CoCrMo and Si_3N_4 were taken as $E_s = 120$ GPa, $E_p = 190$ GPa and $\nu_s = \nu_p = 0.3$ for elastic modulus and Poisson's ratio respectively [42, 81]. Where 's' denotes specimen and 'p' denotes the probe (Si_3N_4) (see table 6-1).

Table 6- 1. Mechanical properties of specimen and AFM probe

	Si_3N_4	Ti6Al4V	CoCrMo
Young's modulus (GPa)	120	190	230
Poisson's ratio	0.33		

The nominal contact pressure is determined in order to correlate the contact pressures to wear rate by fretting motion and combined chemical reactions. The ranges are a result of variations of the initial tip radius and wear on the tip. As mentioned previously the radius of curvature of the tip was monitored before and after each experiment. In a course of experiment, for instance, the average equivalent radius of curvature measured order of 40 nm

to 60 nm and tip wear during the mechanical stimulation presented weak dependence of contact forces in the selected contact loadings.

Results and Discussion

Volume of Ti6Al4V removed is plotted in Figure 6-3 as a function of surface stress state with different group of contact pressure ranges in ambient (room humidity of $35\pm 3\%$). This experimental result illustrated independence of contact pressures as well as pre-stress due to bending under pure mechanical stimulations.

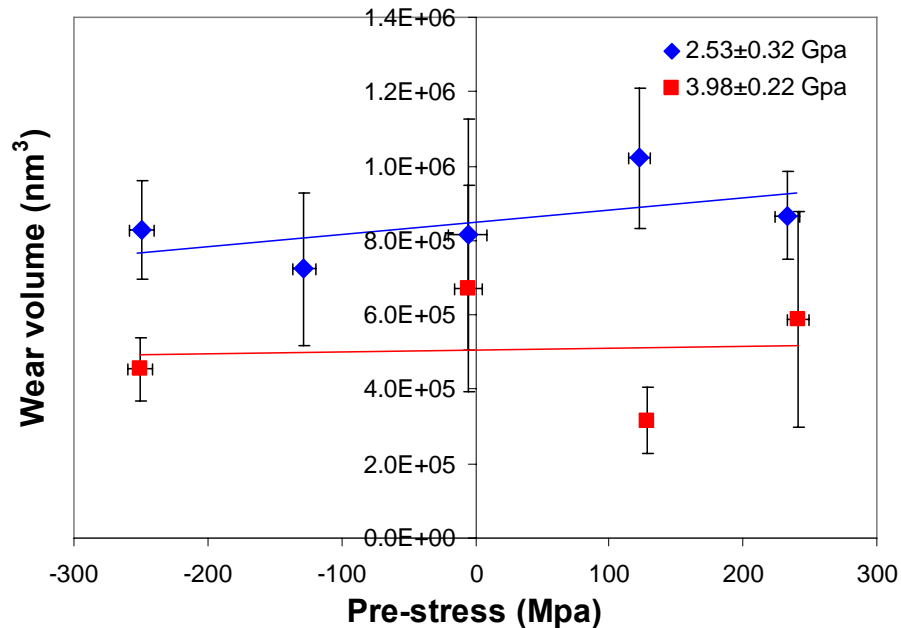


Figure 6- 3. Wear volume of Ti6Al4V with varying pre-stress state due to fretting contact of AFM tip in ambient condition (RH = $35\pm 3\%$).

Wear volume of CoCrMo in ambient (room humidity of $44\pm 5\%$) is presented with varying surface stress state and grouped in different contact pressure ranges. As shown in wear of Ti6Al4V, pre-stress state doesn't affect during continuous scratching motion. However greater contact pressures increases wear rate on CoCrMo surface (see Figure 6-3).

Experimental observation on cast CoCrMo and wrought CoCrMo wear experiment in ambient indicates that the wear rate is approximately three times higher than wear rate of Ti6Al4V and under repeated loading the surface damage can be initiated for very low contact pressures.

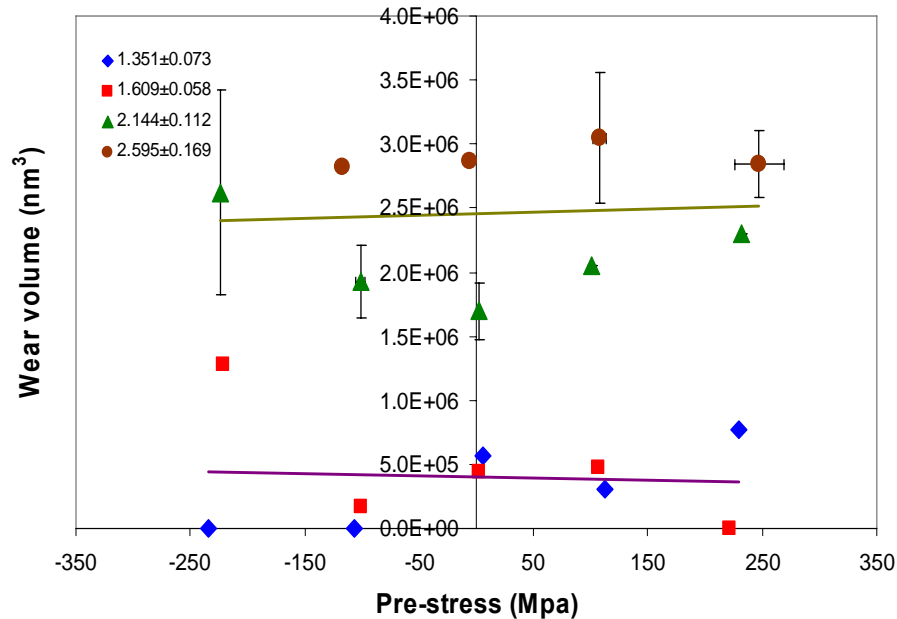


Figure 6- 4. Wear volume of CoCrMo with varying pre-stress state due to fretting contact of AFM tip in ambient condition (RH = 44±5 %).

In ambient and neutral pH value, the wear volume of Ti6Al4V is not dependent on contact pressures. In the passivating condition (PBS pH 7.4) wear rate in Figure 6-5 displays weak dependence of contact stresses over the pre-stress states and amount of wear volume is comparable to the wear in ambient. However, clear quadratic relations of wear volume with varying pre-stresses is shown i.e. under compressive pre-stress the wear rate has been increased while under tensile pre-stress the wear rate has been suppressed. As in the experimental observation of cast CoCrMo [62], Ti6Al4V wear experiment indicates that under repeated loading the surface damage can be initiated for very low contact pressures.

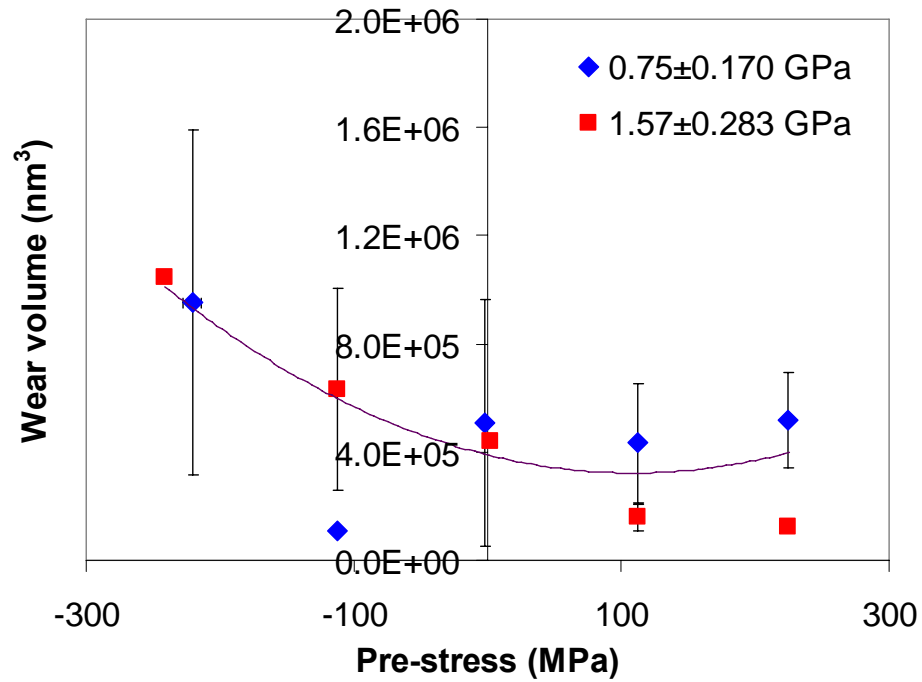


Figure 6- 5. Wear volume of Ti6Al4V with varying pre-stress states due to fretting contact of AFM probe in passivating condition of pH 7.4.

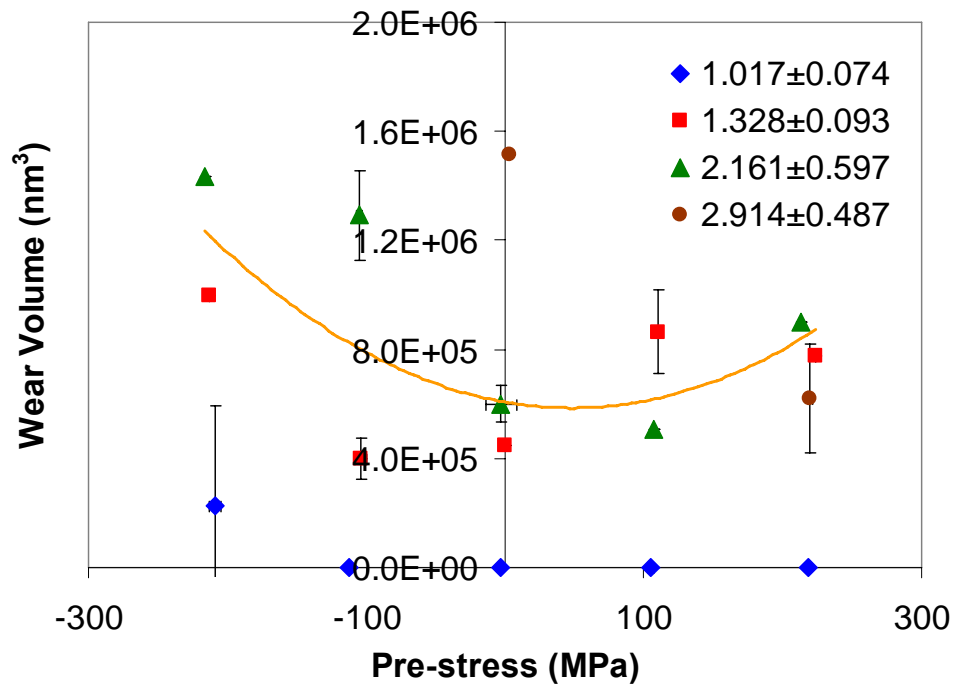


Figure 6- 6. Wear volume of CoCrMo with varying pre-stress states due to fretting contact of AFM probe in passivating condition of pH 7.4

In aqueous environment of neutral pH value, wear volume has been reduced compared to ambient condition over the pre-stress state and contact pressures and overall wear rate of CoCrMo is comparable to Ti6Al4V wear rate in the corresponding environment. The wear in the passivating condition increases with contact pressures and strong dependence of contact stresses over the pre-stress states has been displayed. Namely, skew quadratic relations of wear volume with varying pre-stresses were presented i.e. under compressive pre-stress the wear rate has been increased while under tensile pre-stress the wear rate has been suppressed.

Wear volume in chemically reactive environment has been investigated in three different corresponding reactive chemical conditions, i.e. phosphate buffer solution of pH 4.11 and pH 1.98 and calcium chloride of pH 1.95 respectively.

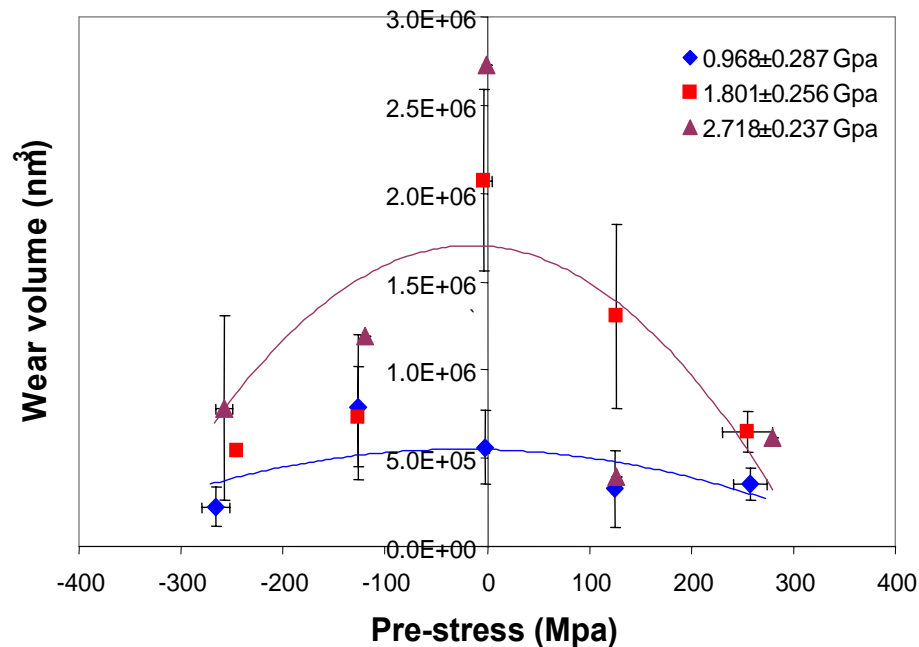


Figure 6- 7. Wear volume of Ti6Al4V with varying pre-stress states due to fretting contact of AFM probe in corroding condition of PBS, pH 4.11.

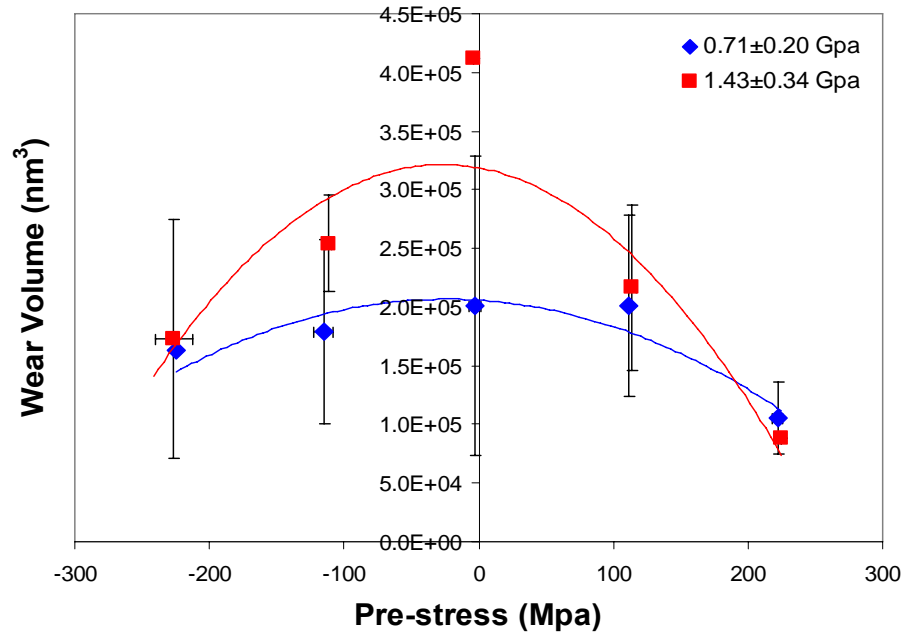


Figure 6- 8. Wear volume of Ti6Al4V with varying pre-stress states due to fretting contact of AFM probe in corroding condition of PBS, pH 1.98.

When the pH is lowered with the addition of HCl in phosphate buffer solution, this skew quadratic behavior is no longer apparent as presented in Figure 6-7 and Figure 6-8. Material removal recorded in the pH 4.11 and pH 1.98 environment indicate that material dissolution rates have a negative quadratic dependence as opposed to the skew quadratic behavior displayed in the non-reactive environment. The material removal due to combination with wear and dissolution is a strong function of contact stresses over the lower pre-stress range between -200 Mpa and 200 Mpa. The higher wear volume was measured with higher contact stresses while the wear volume decreased as high as pre-stress loaded in both of the compression and tension. In addition, in higher acidic PBS the wear volume has been increased comparing to ambient and PBS of neutral pH or lower level of acidity.

Material removal recorded in the pH 4.11 of CaCl₂ environment indicates that material dissolution rates have a skew quadratic dependence as similarly to non-reactive

environment (see Figure 6-9). The material removal due to combination with wear and dissolution dictates a relatively weak contact stress dependence in compressive pre-stress regime. However, the higher wear volume was measured with higher contact stresses under the surface compression. The wear by lowest contact pressure presented almost uniform volume of material removal over the pre-stress state. In the calcium chloride solution of pH 1.95 much higher wear volume on Ti6Al4V was measured comparing to corresponding pH level of PBS (pH 1.98). While the contact pressures are comparable in both cases, the wear volume in CaCl_2 solution was approximately twice of that in PBS. Skew quadratic dependence on surface stress state similarly to pH 7.4 of PBS, presenting increase in compression and decrease in tension as illustrated in Figure 6-10.

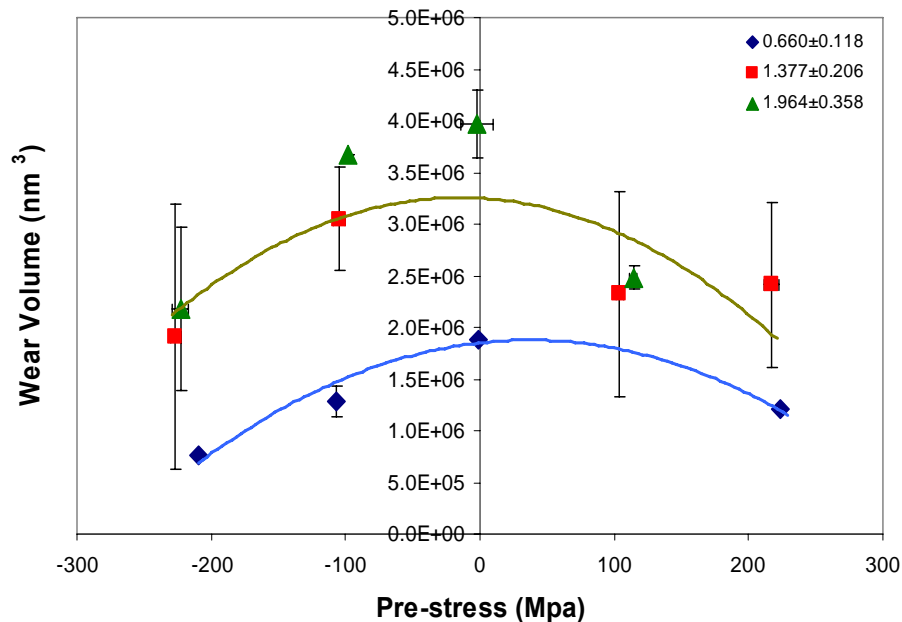


Figure 6- 9. Wear volume of CoCrMo with varying pre-stress states due to fretting contact of AFM probe in corroding condition of PBS, pH 4.11.

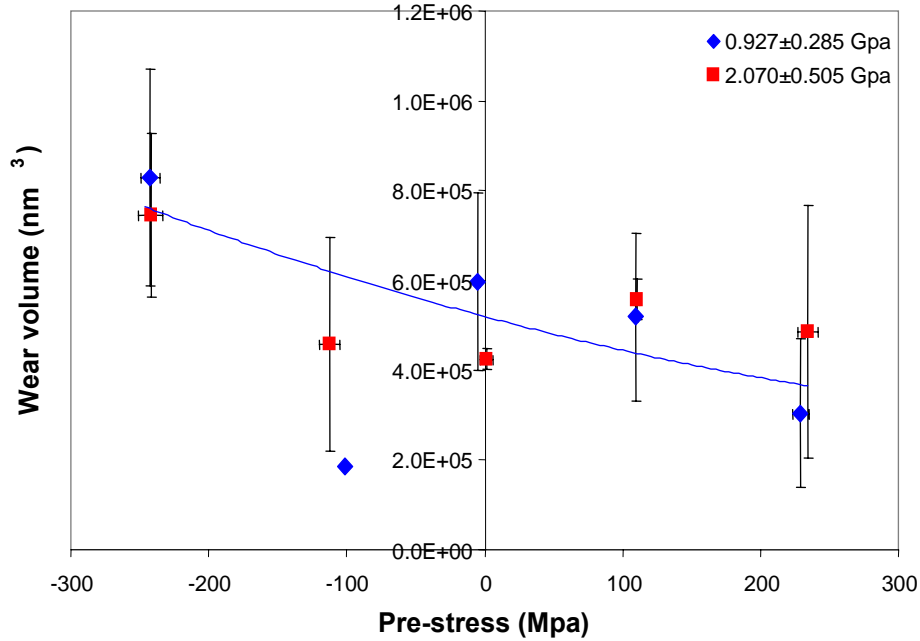


Figure 6- 10. Wear volume of Ti6Al4V with varying pre-stress states due to fretting contact of AFM probe in corroding condition of CaCl₂, pH 1.95.

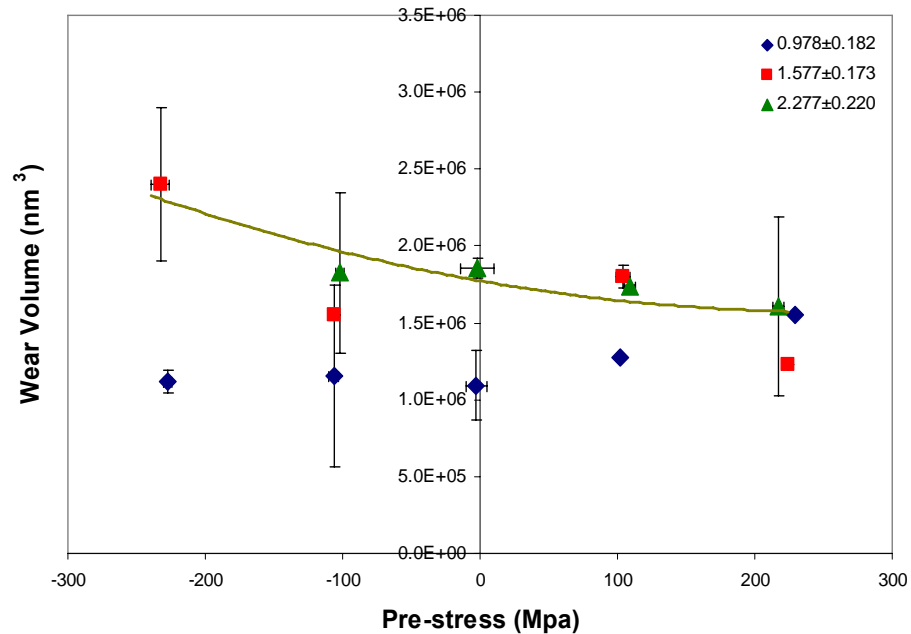


Figure 6- 11. Wear volume of CoCrMo with varying pre-stress states due to fretting contact of AFM probe in corroding condition of CaCl₂, pH 4.11.

As shown in Figure 6-11, material removal recorded in the pH 4.11 of CaCl_2 environment indicate that material dissolution rates have a skew quadratic dependence as similarly to non-reactive environment. The material removal due to combination with wear and dissolution dictates a relatively weak contact stress dependence in compressive pre-stress regime. However, the higher wear volume was measured with higher contact stresses under the surface compression. The wear by lowest contact pressure presented almost uniform volume of material removal over the pre-stress state.

The uncertainty in surface stress values was conservatively estimated by taking into account uncertainties associated with measurement of C-clamp deflection, specimen geometry, roller positions, and distance from edge of the sample. The primary source of error arises from the bending set up deflection as well as error of step motor control of AFM stage by which the desirable surface stress is determined. This uncertainty was incorporated into error estimate for surface stress state. The error associated with material removal was estimated from the standard deviation of trenched area by fretting contact of AFM probe. The range of contact stresses listed in the legend is also obtained by error analysis of effective tip radii measured before fretting experiment. The amount of error caused due to tip shape characterization procedure is assumed negligible since the each protrusion of tip characterizer was identical across all of the substrate.

Surface damage is the result of three possible processes: material delamination, dissolution and repassivation. Surface damage during mechanical stimulation is hypothesized to proceed through delamination of surface layers. However, in the passivating environment, the damaged surface reconstructs oxide layer rapidly and protects exposure to oxygen and moisture resulting in lower wear rates across the varying pre-stresses. When the

environment is reactive, wear mechanism changes to more aggressive chemo-mechanical reactions and as a result, more material is removed even in the similar range of contact pressures. Accordingly, the wear mechanism by combined effect of mechanical and chemical reactions will be determined by physical damage of the surface and associating competition between oxidation of chromium composition, which constructs protective layer, and electrochemical dissolution.

CHAPTER 7. CONCLUSIONS

For load-supporting implant device such as total hip joint replacement, metallic materials have been employed owing to their high ductility and desired wear and friction resistance. However, the corrosion in biological fluid accelerates the degradation of their performance in our body. In this research work, complex damage mechanism in synergistic combination of mechanical and chemical reactions on metallic implant materials have been investigated by analytical and experimental approaches.

Manufactured surface displays scattered protruding asperities and recessed troughs, and when the surface is brought into contact, small scale contact of asperity tip takes place and leads to plastic deformations. During unloading, the residual stress will be developed by mismatch between plastically deformed area and surrounding elastic area. Series of Finite Element Analysis with different roughness and contact pressures depicted that the residual stress field is determined by contact surface configurations and contact loads. Electrochemical reactivity of solid surface interfacing with reactive solution is governed by surface roughness, interfacial energy, strain energy, and chemical potential. Among the multi-factorial combinations, residual stress is a critical factor influencing surface modification process since high variation of residual stress along the interface will be established in rough surface contact. Accordingly, the stress-dependent preferential dissolution determines roughness evolution and ultimate surface crack nucleation during chemo-mechanical process. Fractal surface contact does not display dominant roughness modes but experimental results indicate that a group of roughness modes dominating plastic deformation during loading and stress-assisted dissolution during etching. Fast Fourier

Transform calculation displays contact pressure dependent roughness evolution in contact-etching process, namely, evolving roughness modes ($1/\lambda$) during stress assisted corrosion increases with higher contact pressures.

Roughness evolution of solid surface in chemical reaction illustrates the importance of stress state. If stress states and surface configurations are well characterized the surface instability can be evaluated and localized corrosion damage also can be predicted. For the global application of stress induced corrosion model to anticipate surface degradations, analytical model for contact induced residual stress field has been developed. This combined solution of multi-asperity contact approximates stress states of CoCrMo surface in varying loading conditions depending on body weight and motion. Stress dependence of material dissolution rate from experimental results of CoCrMo surface roughness evolution characterized quadratic correlation between stress and roughness change. Accordingly, this combined solution of multi-asperity contact and dissolution rate can be applied in global use of roughness evolution prediction when CoCrMo surface is stressed by contact in accelerated corrosion environment. In addition, it suggested a direct approximation method of the interfacial energy between solid and liquid. Particularly CoCrMo surface exposed to hydrogen chloride solution characterized $0.352J/m^2$ of interfacial energy which is comparable value with obtained by entropy method [61].

Oxide film such as TiO_2 and Cr_2O_3 plays an important role in fretting contact damage in corrosive environment. The presence of oxide layer prevents the metal surface from oxidation and dissolution due to their stability in electrochemical environment. When the layer is broken and the pure metal alloy is exposed to corrosion, the dissolution of metal ions and passive layer formation take place together. The competition between dissolution rate

and film growth rate may determine total wear rate of the surface in fretting corrosion. As proposed in Chapter 2 and 3, stress states alter the interfacial potential of solid-liquid system and dominate the dissolution response of the surface.

Fretting wear mechanism characterized fatigue crack growth at subsurface during cyclic contact. In particular, CoCrMo implant is usually shaped and manufactured by investment casting process and heat treatment in which subsurface defects such as inclusion and precipitation may be produced during metal flow and solidification. Those subsurface defects progress to critical size of cracks which are able to propagate under fatigue loads. In order to simulate the complex stress field combined with residual stress and contact stress, pre-stress was loaded on the elastic medium from compressive to tensile. This analytical study implies increase in wear rate under compressive residual stress and decrease in wear rate under tensile residual stress. The compressive residual stress leads the crack surface to buckling opening and/or shearing the crack tip. Subsurface cracks experience stresses from compressive to tensile as the slider moves in and away from the cracks, respectively. During compression crack surfaces will be interlocked with high friction between the crack surfaces preventing from relative motions while during tension crack tip undergoes opening and propagates by normal traction on the crack surface. Therefore, the oxide layer fracture by fretting action may be highly dependent on residual stress state developed formerly or superposed stress with neighboring asperity contact-induced stress as well as repeating frictional sliding motion.

Nanoscale contact approximated with uniform friction over the contact area characterized small wear size but higher crack growth rate. Maximum fatigue stress intensity factors have been found at the smaller depth than the parabolic tangential traction. This

nanoscale contact implies smaller wear particle will be produced while the greater crack growth rate per cycle was found. Accordingly, the combination of wear depth and crack growth rate will determine overall wear rate of the surface. The corrosion products of submicron size particulates by the small scale contact may also cause biologically adverse reaction with soft tissue and organs resulting in localized bone loss near implant.

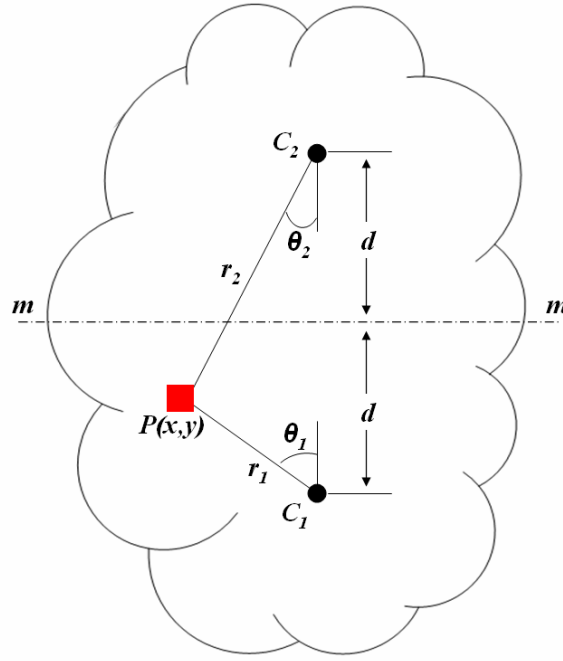
Experimental inspection of fretting corrosion damage as a function of contact stress and residual stress in aqueous environment illustrated oxide layer formation behavior depends on residual stress field. In the passivating environment (PBS pH 7.4) the wear rate displayed strong dependence of pre-stress; increase in wear depth under compressive pre-stress and decrease in wear depth under tensile pre-stress as depicted in delamination wear model. However, the fretting corrosion of titanium alloy doesn't show contact stress dependent wear while wear on cobalt alloy presents strong dependence on contact stresses. Chemo-mechanical reaction was observed in chemically reactive environment of PBS pH 4.11 solution. Oxide film may be developed more rapidly and reached to oxide film stability due to increased interfacial potential by higher concentration of reactive ions in the solution. It was observed that stress enhances reactivity of metal alloy during corrosion in stress-assisted dissolution experiment. Similarly the stress loaded in compression and tension by bending deflection may increase the oxide film growth rate and protective oxide layer thickness. Therefore, wear rate was reduced likely by increased oxide layer growth rate and thickness by stresses. The less wear rate of titanium alloy in reactive environment (pH 4.11) may be one of the evidences of the more aggressive and rapid formation of TiO_2 film compared to oxide layer growth on CoCrMo alloy. Secondly, since TiO_2 characterizes

higher resistance to ionic transport through the oxide layer than Cr_2O_3 does, as experimental results displayed, more stable corrosion barrier reduces wear of Ti6Al4V surface.

In the present study of interface degradation of metallic implant material, strong influence of stress on electrochemical reaction was found. Stress state governs oxide film characteristics in environmental corrosion since interfacial potential tends to be altered by strain energy simulated by mechanical interactions. Retrieval study of implant materials and human tissue near the implant presented that submicron size metallic particles immigrated in surrounding soft tissue generating inflammation in the absence of implant surface damage. It is evidence the ionic transportation of metal ions can take place through the oxide layer. The experimental and analytical study of implant surface degradation elucidated the stress dependence of interfacial potential and provided a guide line in design consideration required to enhance implant device performance in biological fluid.

APPENDIX

Stress state due to embedded pair of center of dilatation in joining semi-infinite elastic medium.



Stress $\sigma_{ij}^{c_1}$ due to C_1 ;

$$\sigma_x^{c_1} = \sigma_{r_1} \sin^2 \theta_1 + \sigma_{\theta_1} \cos^2 \theta_1 - 2\tau_{r_1\theta_1} \sin \theta_1 \cos \theta_1$$

$$\sigma_y^{c_1} = \sigma_{r_1} \cos^2 \theta_1 + \sigma_{\theta_1} \sin^2 \theta_1 + 2\tau_{r_1\theta_1} \sin \theta_1 \cos \theta_1$$

$$\tau_{xy}^{c_1} = (\sigma_{r_1} - \sigma_{\theta_1}) \sin \theta_1 \cos \theta_1 + (\sin^2 \theta_1 - \cos^2 \theta_1) \tau_{r_1\theta_1}$$

Stress $\sigma_{ij}^{c_2}$ due to C_2 ;

$$\sigma_x^{c_2} = \sigma_{r_2} \sin^2 \theta_2 + \sigma_{\theta_2} \cos^2 \theta_2 - 2\tau_{r_2\theta_2} \sin \theta_2 \cos \theta_2$$

$$\sigma_y^{c_2} = \sigma_{r_2} \cos^2 \theta_2 + \sigma_{\theta_2} \sin^2 \theta_2 + 2\tau_{r_2\theta_2} \sin \theta_2 \cos \theta_2$$

$$\tau_{xy}^{c_2} = (\sigma_{r_2} - \sigma_{\theta_2}) \sin \theta_2 \cos \theta_2 + (\sin^2 \theta_2 - \cos^2 \theta_2) \tau_{r_2\theta_2}$$

Total stress σ_{tot} ($= \sigma^{c_1} + \sigma^{c_2}$) at center line $m-m$ ($\theta_1 = \theta_2$ and $r_1 = r_2$);

$$\sigma_x = 2(\sigma_r \sin^2 \theta + \sigma_\theta \cos^2 \theta)$$

$$\sigma_y = 2(\sigma_r \cos^2 \theta + \sigma_\theta \sin^2 \theta)$$

$$\tau_{xy} = 2\tau_{r\theta}(\sin^2 \theta - \cos^2 \theta) = 0$$

Since,

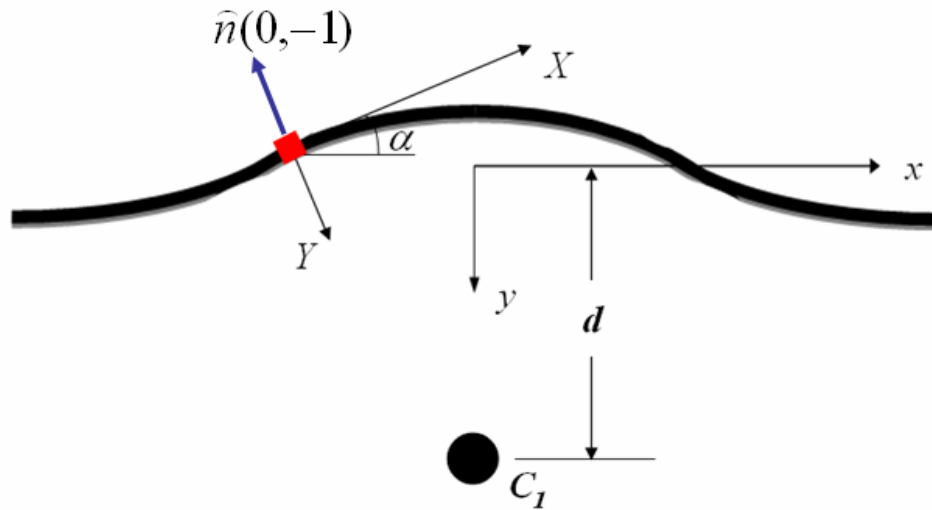
$$\sigma_r = -\frac{C}{r^2} \quad \text{and} \quad \tau_{r\theta} = 0$$

$$\sigma_\theta = \frac{C}{r^2}$$

$$\sigma_x = -2C \left(\frac{x^2 - d^2}{r^4} \right) \quad \text{and} \quad \begin{cases} \sin \theta = \frac{x}{r} \\ \cos \theta = \frac{d}{r} \\ r = \sqrt{x^2 + y^2} \end{cases}$$

$$\sigma_y = 2C \left(\frac{x^2 - d^2}{r^4} \right)$$

Small perturbation of the center line $m-m$ with cosine curve where $a/\lambda \ll 1$
as; $h(x) = -a \cos(2\pi x/\lambda)$



Stress along the local coordinate X - Y by rotation with R ;

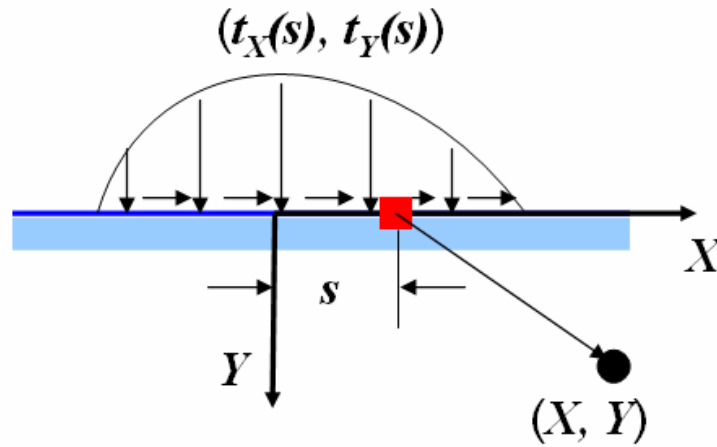
$$\sigma_{IJ} = R^T \sigma_{ij} R = \begin{bmatrix} \sigma_x & h_{,x}(\sigma_x - \sigma_y) \\ h_{,x}(\sigma_x - \sigma_y) & \sigma_y \end{bmatrix}, \text{ where } R = \begin{bmatrix} \cos \alpha & \sin \alpha \\ -\sin \alpha & \cos \alpha \end{bmatrix}$$

$$\text{and } \sin \alpha \approx h_{,x} = \frac{\partial h}{\partial x}, \cos \alpha \approx 1.$$

Traction forces on surface normal to $\hat{n}(0, -1)$ along X - Y coordinates,

$$t_I = \hat{n} \sigma_{IJ} = (0, -1) \begin{bmatrix} \sigma_x & h_{,x}(\sigma_x - \sigma_y) \\ h_{,x}(\sigma_x - \sigma_y) & \sigma_y \end{bmatrix} = [-h_{,x}(\sigma_x - \sigma_y), -\sigma_y]$$

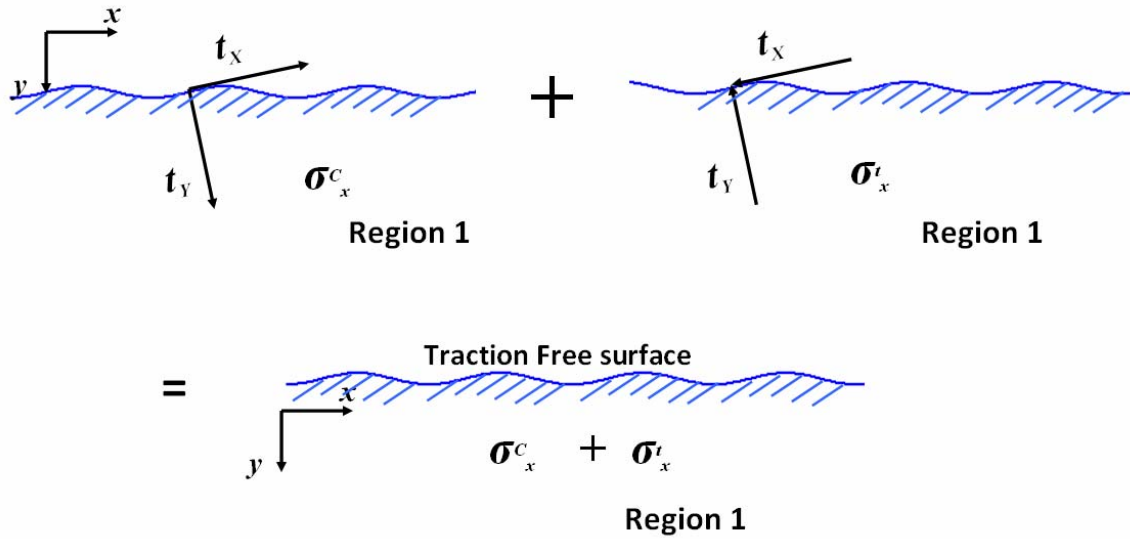
Stress components due to reverse surface traction of t_I to achieve traction free surface were obtained by solution of normal and tangential contact from Johnson [76]



Stress due to traction at surface $Y=0$;

$$\overline{\sigma_X} = \int_{-\infty}^{\infty} -\frac{2t_X(s)}{\pi(X-s)} ds$$

$$\text{and } \overline{\sigma_Y} = \overline{\tau_{XY}} = 0.$$



Combined total stress on the surface $m-m$ will be superposition of stress field due to equal and opposite traction, $-t_x$;

$$\bar{\sigma}_x = -2C \frac{x^2 - d^2}{(x^2 + d^2)^2} + \frac{2}{\pi} \int_{-\infty}^{\infty} \frac{t_x(s)}{(X-s)} ds$$

$$\bar{\sigma}_y = 2C \frac{x^2 - d^2}{(x^2 + d^2)^2}$$

$$\text{, where } t_x(s) = -h_{,s} \left[-4C \frac{s^2 - d^2}{(s^2 + d^2)^2} \right] = \frac{8aC\pi}{\lambda} \frac{s^2 - d^2}{(s^2 + d^2)^2} \sin\left(\frac{2\pi}{\lambda} s\right)$$

In the presence of line dilatation series (C_i) cyclically with space of λ the final surface stresses are;

$$\bar{\sigma}_x = -2C \sum_{n=-\infty}^{\infty} \frac{(x+n\lambda)^2 - d^2}{\{(x+n\lambda)^2 + d^2\}^2} + \frac{16aC}{\lambda} \int_{-\infty}^{\infty} \sin\left(\frac{2\pi}{\lambda} s\right) \sum_{n=-\infty}^{\infty} \frac{(s+n\lambda)^2 - d^2}{\{(s+n\lambda)^2 + d^2\}^2 (x-s)} ds$$

$$\bar{\sigma}_y = 2C \sum_{n=-\infty}^{\infty} \frac{(x+n\lambda)^2 - d^2}{\{(x+n\lambda)^2 + d^2\}^2}$$

REFERENCES

1. Brown, S.A. and K. Merritt, Fretting corrosion in saline and serum. *J Biomed Mater Res*, 1981. 15(4): p. 479-488.
2. Bundy, K.J., Corrosion and Other Electrochemical Aspects of Biomaterials. *Critical Reviews in Biomedical Engineering*, 1994. 22(3-4): p. 139-251.
3. Gil, F.J., et al., Fretting corrosion behaviour of ball-and-socket joint on dental implants with different prosthodontic alloys. *Bio-Medical Materials and Engineering*, 2003. 13(1): p. 27-34.
4. Gilbert, J.L., C.A. Buckley, and J.J. Jacobs, In vivo corrosion of modular hip prosthesis components in mixed and similar metal combinations. The effect of crevice, stress, motion, and alloy coupling. *J Biomed Mater Res*, 1993. 27: p. 1533-1544.
5. Gilbert, J.L. and J.J. Jacobs, The mechanical and electrochemical processes associated with taper fretting crevice corrosion: A review, in *Modularity of Orthopedic Implants*, D.E. Marlowe, J.E. Parr, and M.B. Mayor, Editors. 1997, American Society Testing and Materials: W Conshohocken. p. 45-59.
6. Goldberg, J.R. and J.L. Gilbert, In vitro corrosion testing of modular hip tapers. *Journal of Biomedical Materials Research Part B-Applied Biomaterials*, 2003. 64B(2): p. 78-93.
7. Hallab, N.J. and J.J. Jacobs, Orthopedic implant fretting corrosion. *Corros Rev*, 2003. 21(2-3): p. 183-213.

8. Hallab, N.J., C. Messina, A. Skipor, and J.J. Jacobs, Differences in the fretting corrosion of metal-metal and ceramic-metal modular junctions of total hip replacements. *Journal of Orthopaedic Research*, 2004. 22: p. 250-259.
9. Jacobs, J.J., J.L. Gilbert, and R.M. Urban, Corrosion of metal orthopaedic implants. *Journal of Bone and Joint Surgery-American Volume*, 1998. 80A(2): p. 268-282.
10. Jacobs, J.J., et al., Metal release in patients who have has a primary total hip arthroplasty - A prospective, controlled, longitudinal study. *Journal of Bone and Joint Surgery-American Volume*, 1998. 80A(10): p. 1447-1458.
11. Nakashima, Y.e.a., Hydroxyapatite-coating on titanium arc sprayed titanium implant. *Journal of Biomedical Materials Research*, 1997. 35: p. 287-298.
12. Hauert, R., An overview on the tribological behavior of diamond-like carbon in techincal and medical applications. *Tribological International*, 2004. 37: p. 991-1003.
13. Zhang, H.e.a., Nano-Hydroxyapatite Coated Femoral Stem Implant by Electrophoretic Deposition. *Materials Research Society Symposium Proceedings*, 2006.
14. Lewis, G., Design issues in clinical studies of the in vivo volumetric wear rate of polyethylene bearing components. *Journal of Bone and Joint Surgery-American Volume*, 2000. 82A(2): p. 281-287.
15. Lewis, G., Geometric element analysis of fretting in a model of a modular femoral component of a hip implant *Bio Med Mater Eng*, 2004. 14: p. 43-51.
16. Mudali, U.K., Sridhar,T.M. and Raj, B., Corrosion of bio implant. *Sadhana*, 2003. 28: p. 601-637.
17. Hallab, N.J., and J. J. Jacobs, Orthopedic implant fretting corrosion. *Corrosion reviews*, 2003. 21(Nos. 2-3): p. 183-213.

18. Brown, S.A., C.A.C. Flemming, J.S. Kawalec, H.E. Placko, C. Vassaux, K. Merritt, J.H. Payer, and M.J. Kraay, Fretting corrosion accelerates crevice corrosion of modular hip tapers. *Journal of Applied Biomaterials*, 1995. 6: p. 19-26.
19. He, D.X., T.C. Zhang, and Y.S. Wu, Fretting and galvanic corrosion behaviors and mechanisms of Co-Cr-Mo and Ti-6Al-4V alloys. *Wear*, 2001. 249(10-11): p. 883-891.
20. Goldberg, J.R., et al., A multicenter retrieval study of the taper interfaces of modular hip prostheses. *Clinical Orthopaedics and Related Research*, 2002(401): p. 149-161.
21. Kraft, C.N., B. Burian, O. Diedrich, and M.A. Wimmer, Implications of orthopedic fretting corrosion particles on skeletal muscle microcirculation. *Journal of Materials Science: Materials in Medicine*, 2001. 12: p. 1057-1062.
22. Wimmer, M.A., J. Loos, R. Nassutt, M. Heitkemper, and A. Fischer, The acting wear mechanisms on metal-on-metal hip joint bearings: in vitro results. *Wear*, 2001. 250: p. 129-139.
23. Bundy, K.J., et al, Ph shifts and precipitation associated with metal-ions in tissue culture. *Biomaterials*, 1985. 6(2): p. 89-96.
24. Bundy, K.J., C.J. Williams, and R.E. Luedemann, Stress-Enhanced Ion Release - the Effect of Static Loading. *Biomaterials*, 1991. 12(7): p. 627-639.
25. Viceconti, M., et al., Fretting wear in a modular neck hip prosthesis. *Journal of Biomedical Materials Research*, 1997. 35(2): p. 207-216.
26. Viceconti, M., et al, Design-related fretting wear in modular neck hip prosthesis. *J Biomed Materi Res*, 1996. 30(2): p. 181-186.
27. Archard, J.F., Elastic Deformation and the Laws of Friction. *Pro Roy Soc (London)*, 1957. 243(1233): p. 190-205.

28. Greenwood, J.A., and J.B.P. Williamson, Contact of Nominally Flat Surfaces. *Pro Roy Soc (London)*, 1966. 295(1442): p. 300-319.
29. Whitehouse, D.J., and J.F. Archard, The properties of random surfaces of significance in their contact. *Pro Roy Soc (London)*, 1970. 316(1524): p. 97-121.
30. Onions, R.A., and J. F. Archard, The contact of surfaces having a random structure. *J Phys D: Appl Phys*, 1973. 6: p. 289-304.
31. Bush, A.W., R.D. Gibson, and T. R. Thomas, The elastic contact of a rough surface. *Wear*, 1975. 35: p. 87-111.
32. Johnson, K.L., J.A. Greenwood, and J.G. Higgins, The contact of elastic regular wavy surfaces. *Int J Mech Sci*, 1985. 27(6): p. 383-396.
33. Chang, W.R., I. Etsion, and D.B. Bogy, An elastic-plastic model for the contact of rough surfaces. *Journal of Tribology*, 1987. 109: p. 257-263.
34. Yan, W., and K. Komvopoulos, Contact analysis of elastic-plastic fractal surfaces. *Journal of Applied Physics*, 1998. 84(7): p. 3617-3624.
35. Ciavarella, M., G. Demelio, J.R. Barber, and Y.H. Jang, Linear elastic contact of the Weierstrass profile. *Pro Roy Soc (London)*, 2000. 456: p. 387-405.
36. Gong, Z.Q., and K. Komvopoulos, Effect of surface patterning on contact deformation of elastic-plastic layered media. *Journal of Tribology*, 2003. 125: p. 16-24.
37. Abbott, E.J., and F.A. Firestone, Specifying Surface Quality - A Method Based on Accurate Measurement and Comparison. *Mech. Eng.*, 1933. 55: p. 569.
38. Kogut, L., and I. Etsion, Elastic-plastic contact analysis of a sphere and a rigid flat. *J of Appl Mech*, 2002. 69: p. 657-662.

39. Jackson, R.L., and I. Green. A finite element study of elasto-plastic hemispherical contact. in STLE/ASME Joint International Tribology Conference. 2003. Ponte Vedra Beach, Florida USA: ASME.
40. Zhao, Y., D.M. Maietta, and L. Chang, An asperity microcontact model incorporating the transition from elastic deformation to fully plastic flow. *Journal of Tribology*, 2000. 122: p. 86-93.
41. Gao, Y.F. and A.F. Bower, Elastic-plastic contact of a rough surface with Weierstrass profile. *Proceedings of the Royal Society A*, 2006. 462(2065): p. 319-348.
42. Fraker, A.C., *ASM handbook*. , in *Corrosion of metallic implants and prosthetic device*, A.C. Fraker, Editor. p. 1324-1335.
43. Herrera, M., et al., Effect of C content on the mechanical properties of solution treated as-cast ASTM F-75 alloys. *J Mat Sci Mat Med*, 2005. 16(7): p. 607-611.
44. Kilner, T., et al., Static mechanical-properties of cast and sinter-annealed cobalt-chromium surgical implants. *J Mater Sci*, 1986. 21(4): p. 1349-1356.
45. Barber, J.R., and Ciavarella, M., Contact mechanics. *Int J Sol Str*, 2000. 37: p. 29-43.
46. Kim, K.S., J.A. Hurtado, and H. Tan, Evolution of a surface-roughness spectrum caused by stress in nanometer-scale chemical etching. *Physical Review Letters*, 1999. 83(19): p. 3872-3875.
47. Schaaff, P., The role of fretting damage in total hip arthroplasty with modular design hip joints - evaluation of retrieval studies and experimental simulation methods. *Journal of Applied Biomaterials & Biomechanics*, 2004. 2: p. 121-135.
48. Barvosa-Carter, W., et al., Kinetically driven growth instability in stressed solids. *Physical Review Letters*, 1998. 81(7): p. 1445-1448.

49. Ryu, J., V. Dayal, and P. Shrotriya, Onset of Surface Damage in Modular Orthopedic Implants: Influence of Normal Contact Loading and Stress-assisted Dissolution. *Experimental Mechanics*, 2007. 47: p. 395.
50. Mitchell, A. and P. Shrotriya, Stress assisted dissolution of biomedical grade CoCrMo: Influence of contact loads and residual stresses. 2006.
51. Smith, H.F., The problem of comparing the results of two experiments with unequal errors. *Journal of the Council of Scientific and Industrial Research*, 1936. 9: p. 211-212.
52. Satterthwaite, F.E., An Approximate Distribution of Estimates of Variance Components *Biometrics Bulletin*, 1946. 2: p. 110-114.
53. Srolovitz, D.J., On the Stability of Surfaces of Stressed Solids. *Acta Metallurgica*, 1989. 37(2): p. 621-625.
54. Asaro, R. and W. Tiller, Interface Morphology Development During Stress Corrosion Cracking: Part I. Via Surface Diffusion. *Metallurgical Transactions*, 1972. 3: p. 1789-1796.
55. Aziz, M.J., P.C. Sabin, and G.Q. Lu, The Activation Strain Tensor - Nonhydrostatic Stress Effects on Crystal-Growth Kinetics. *Physical Review B*, 1991. 44(18): p. 9812-9816.
56. Yu, H. and Z. Suo, Stress-dependent surface reactions and implications for a stress measurement technique. *Journal of Applied Physics*, 2000. 87: p. 1211-1218.
57. Liang, J. and Z. Suo, Stress-Assisted Reaction at a Solid-Fluid Interface. *Interface Science*, 2001. 9: p. 93-104.
58. Hardy, C., C.N. Baronet, and G.V. Tordion, The elasto-plastic indentation of a half-space by a rigid sphere. *International Journal for Numerical Methods in Engineering*, 1971. 3: p. 451.

59. Yu, H.Y. and S.C. Sanday, Elastic Field in Joined Semi-Infinite Solids with an Inclusion. Proceedings: Mathematical and Physical Sciences, 1991. 434: p. 521-530.
60. Davies, J.H., Elastic Field in a Semi-Infinite Solid due to Thermal Expansion or a Coherently Misfitting Inclusion. Journal of Applied Mechanics 2003. 70: p. 655-660.
61. Jian, Z., K. Kuribayashi, and W. Jie, Solid-liquid interface energy of metal at melting point and undercooled state. Materials Transaction, 2002. 43: p. 721-726.
62. Mitchell, A. and P. Shrotriya, Onset of nanoscale wear of metallic implant materials: Influence of surface residual stresses and contact loads Wear, 2007. 263: p. 1117-1123.
63. Suh, N.P., The delamination theory of wear Wear, 1973. 25: p. 111-124.
64. Jahanmir, S., N.P. Suh, and E.P. Abrahamson, Microscopic Observations of the Wear Sheet Formation by Delamination. Wear, 1974. 28: p. 235-249.
65. Fleming, J.R. and N.P. Suh, Mechanics of Crack Propagation in Delamination Wear Wear, 1977. 44: p. 39-56.
66. Jahanmir, S. and N.P. Suh, Mechanics of Subsurface Void Nucleation in Delamination Wear Wear, 1977. 44: p. 17-38.
67. Suh, N.P., Overview of the Delamination Theory of Wear Wear, 1977. 44: p. 1-16.
68. Thouless, M.D., et al., The Edge Cracking and Spalling of Brittle Plates. Acta Materialia, 1986. 35: p. 1333-1341.
69. Larsson, S.G. and A.J. Carlsson, Influence of non-singular stress terms and specimen geometry on small-scale yielding at crack tips in elastic-plastic materials. Journal of the Mechanics and Physics of Solids, 1973. 21: p. 263 - 277.
70. Williams, J.G. and P.D. Ewing, Fracture under complex stress - The angled crack problem. International Journal of Fracture Mechanics, 1972. 8: p. 441.

71. Cotterell, B., Notes on the paths and stability of cracks International Journal of Fracture Mechanics, 1966. 2: p. 526-533.
72. Chua, B., Investigation into the stress assisted damage of copper surface under single asperity [electronic resource] : influence of contact pressures, surfaces stress states and environments. Thesis (M.S.), Iowa State University, 2008., 2008.
73. Jeng, Y.R. and S.M. Chiu, Innovative Wire Bonding Method Using a Chemically Reacted Thin Layer for Chips with Copper Interconnects. Journal of Electronic Materials, 2006. Vol. 35: p. 279.
74. Tsui, T.Y., W.C. Oliver, and G.M. Pharr, Influences of stress on the measurement of mechanical properties using nanoindentation: Part I. Experimental studies in an aluminum alloy. Journal of Materials Research 1996. 11(3): p. 752-759.
75. Schall, J.D. and D.W. Brenner, Atomistic simulation of the influence of pre-existing stress on the interpretation of nanoindentation data. Journal of Materials Research, 2004. 19: p. 3172-3180
76. Johnson, K.L., Contact Mechanics. 1987, Cambridge, UK: Cambridge University Press.
77. Bhushan, B. and A.V. Kulkarni, Effect of normal load on microscale friction measurements. Thin solid films, 1996. 278: p. 49-56.
78. McEwen, E., Stresses in elastic cylinders in contact along a generatrix. Philosophical Magazine, 1949. 40: p. 454.
79. Drory, M.D., M.D. Thouless, and A.G. Evans, On the Decohesion of Residually Stressed Thin Films Acta Metall, 1988. 36: p. 2019-2028.

80. Hutchinson, J.W. and Z. Suo, Mixed mode cracking in layered materials. *Advances in applied mechanics* 1992. 29: p. 63-191.
81. Ho, S.P., et al., Nanotribology of CoCr-UHMWPE TJR prosthesis using atomic force microscopy. *Wear*, 2002. 253(11-12): p. 1145-1155.

ACKNOWLEDGEMENT

I would like to express my gratitude to my advisor, Dr. Pranav Shrotriya for his guidance, encouragement, and support for the research and graduate studies. Apart from his academic guidance, I have always been a recipient of his generosity and patience and good advice. I also wish to thank Prof. Palaniappa Molian, Prof. Sriram Sundararajan, Prof. LeAnn Faidley, and Prof. Vinay Dayal for taking the time to serve on my graduate committee. I would like to thank my fellow graduate students, and officemates, Dinesh Karyana-Sundaram, Kyongho Kang, Kanaga Karuppiah, and Yilei Zhang for helpful discussion about the experiments and coursework. And finally, I like to thank to my parents and family for their love and support.